Integrated SOFC/GT Systems with Improved Dynamic Capabilities for Mobile Applications

by

Zhenzhong Jia

A dissertation submitted in partial fulfillment
of the requirements for the degree of
Doctor of Philosophy
(Naval Architecture & Marine Engineering)
in The University of Michigan
2014

Doctoral Committee:

Professor Jing Sun, Chair
Associate Professor Ryan M. Eustice
Professor Huei Peng
Professor Anna Stefanopoulou
Professor Armin W. Troesch

ACKNOWLEDGEMENTS

It has been three years (Sept 2011- Sept 2014) since I started my PhD study at the Department of Naval Architecture & Marine Engineering (NAME) at the University of Michigan. This work would not have been possible without the help and support from my family, advisor, lab-mates and friends.

First, I would like to give my grateful and sincere thanks to my advisor, Prof. Jing Sun, for her consistent guidance, advice, help and support in both my work and life. Her insights and suggestions made this work possible. Even though my productivity had its ups and downs, her continuous support and patience allowed the completion of my goal. I also wish to thank other members of my doctoral committee, Prof. Huei Peng, Prof. Anna Stefanopoulou, Prof. Armin Troesch and Prof. Ryan Eustice for their helpful comments and kind encouragement.

I would like to extend my gratitude to my friends and colleagues at the University of Michigan for their help and friendship. In particular, I want to thank So-Ryeok Oh, the former research scientist in the RACE Lab, for all the valuable advices and discussions. I would also like to thank Caihao Weng, Jun Hou, Hyeongjun Park, Qiu Zeng, Dave Reed, Esteban Castro, and Richard Choroszucha in the RACE Lab. I would also like to express my gratitude towards Xiaowu Zhang, Tianyou Guo and other members in the VDL Lab and Qingsi Wang from the EECS department for their supports.

I would like to acknowledge Automotive Research Center (US Army TARDEC) and Naval Engineering Education Center (US Navy) for the financial support. My sincere gratitude also goes to Herb Dobbs and Joel King for their valuable advices.

Finally, I would like to express my deepest thanks to my parents and my brother, for their unwavering faith in me and constant encouragement through the years.

TABLE OF CONTENTS

LIST OF FIGURES

LIST OF TABLES

LIST OF APPENDICES

NOMENCALTURE

SOFC Modeling

A	Area of the electro-chemical reaction $[m^2]$
C_s	Molar concentration of species s $[mol \cdot m^{-3}]$
E_0	Nernst potential $[V]$
F	Faraday constant $[C \cdot mol^{-1}]$
I_{com}	Current density command $[A \cdot m^{-2}]$
N_d	Number of discretization units in the finite volume method
N_{cell}	Number of cells in the SOFC stack [-]
$N_{in,s}, N_{out,s}$	Inlet and outlet molar rate of species s, respectively $[mol \cdot sec^{-1}]$
K_{eq}	Equilibrium constant of chemical reaction
P	Power $[W]$
Q_{cond}	Heat conduction flux $[J \cdot sec^{-1}m^{-2}]$
Q_{in}, q_{out}	Inlet and outlet enthalpy flux of gas flows $[J \cdot sec^{-1}m^{-2}]$
$\tilde{R}$	Universal ideal gas constant $[J \cdot mol^{-1} \cdot K^{-1}]$
R_{ohm}	Ohmic resistance $[\Omega]$
T	Temperature $[K]$
U, U_{cell}, U_{sofc}	Operating voltage or potential loss of the SOFC cell $[V]$
U_{OCV}	Open circuit voltage $[V]$
V	Volume $[m^3]$
W	Air/gas mass flow rate $[kg \cdot sec^{-1}]$
$c_{v,s}$	Heat capacity of gaseous species s $[J \cdot K^{-1}mol^{-1}]$
c_p	Heat capacity of solid layers $[J \cdot K \cdot kg^{-1}]$
$c_{p,air}, c_{p,gas}$	Heat capacity of air or gas $[J \cdot K^{-1}mol^{-1}]$
d_k	Characteristic length of channel k $[m]$
$h_s(T)$	Specific enthalpy of species s at temperature T $[J \cdot mol^{-1}]$

i	Current density of a unit $[A \cdot m^{-2}]$
$k_{a,b}$ (e.g., $k_{f,PEN}$)	Heat transfer coefficient from layer a to layer b $[J \cdot K^{-1}m^{-2}s^{-1}]$
l	Length of cell discretization unit $[m]$
p	Pressure of gas or gas species $[Pa]$
r_k	Rate of reaction k $[mol \cdot sec^{-1}m^{-2}]$
$v_{s,k}$	Stoichiometric coefficient of species s in reaction k
α	Orifice constant of gas channels $[m \cdot sec]$
ϵ	Emissivity of solid layers
λ	Thermal conductivity of layers $[J \cdot sec^{-1}m^{-1}K^{-1}]$
γ	Heat capacity ratio, $\gamma = c_p/c_v$
ρ	Density $[kg \cdot m^{-3}]$
σ	Stefan-Boltzmann constant $[W \cdot m^{-2}K^{-4}]$
τ	Solid layer thickness $[m]$

Others

D	Turbine blade tip diameter $[m]$
E_{brg}	Battery capacity requirement $[kJ]$
ER	Turbine expansion ratio [-]
J	Effective moment of inertia for the GT-generator $[kg \cdot m^2]$
K_{SM}	Compressor surge margin [-]
M	Molar weight $[kg \cdot mol^{-1}]$
N	Shaft speed $[RPM]$
N_0, N_{crt}, N_{min}	Threshold, critical and lower limit shaft speed $[RPM]$
N_{tc}	Corrected turbine speed $[RPM \cdot K^{-0.5}]$
$\widetilde{N}, \widetilde{W}$	Normalized speed, normalized mass flow rate [-]
P_{base}	Baseline power demand $[W]$
P_{peak}	Peak power demand $[W]$
PR	Compressor pressure ratio [-]
T_{cell}, T_{sofc}	SOFC cell temperature $[K]$
T_{grad}	SOFC local cell temperature gradient $[K \cdot m^{-1}]$

m	Mass $[kg]$
t_d, t_r	Delay time and ramping time of fuel supply $[sec]$
t_s or T_s	Settling time of transient response $[sec]$
v_T	Cell temperature change rate $[K \cdot min^{-1}]$
α	$\alpha = (2\pi/60)^2$, convert shaft speed from RPM to $rad \cdot sec^{-1}$
ΔT_{LM}	Logarithmic mean temperature difference $[K]$
η	Efficiency [-]
ϕ_t, ϕ_{choke}	Corrected turbine flow, capacity $[kg \cdot K^{0.5} \cdot sec^{-1} bar^{-1}]$
τ	Time-constant $[sec]$

Subscript and Superscript

HEX	Heat exchanger
INJ	Injector
PEN	PEN structure
SET	Set values
SS	Steady-state
afd	Air feeding tube, injected air
bed	Catalytic burner bed reactor
an	Anode
$c, comp$	Compressor
ca	Cathode
cb	Catalytic burner
des	Desired
$design$	Parameters at design points
f	Fuel
gen	Generator
net	Net, total
$norm$	Normalized
$sofc$	Solid oxide fuel cell
$t, turb$	Turbine

Abbreviations

APU	Auxiliary Power Unit
AR	Air excessive Ratio
BIBO	Bounded Input Bounded Output
CB	Catalytic Burner
ERD	Energy Recuperation Device
FU	Fuel Utilization ratio
G/M	Generator/Motor
GT	Gas Turbine
HEX	Heat EXchanger
ICE	Internal Combustion Engine
IS-RG	Incremental Step-Reference Governor
LG	Load Governor
LUT	Look-Up Table
MPC	Model Predictive Control
Ox	Oxidation reaction
PEN	Positive electrode-Electrolyte-Negative electrode assembly
RCL	Rich-Catalytic Lean-burn
Red	Reduction reaction
RGA	Relative Gain Array
RMS	Root Mean Square
RPM	Revolution Per Minute
R-SOFC/GT	Recuperating SOFC/GT
SOFC	Solid Oxide Fuel Cell
S-SOFC/GT	Sprinter-SOFC/GT
SR	Steam Reforming
TIT, TOT	Turbine Inlet Temperature, Turbine Outlet Temperature
VGC or VGT	Variable Geometry Compressor or Variable Geometry Turbine
WGS	Water Gas Shift
ZSLM	Zero Slope Line Method

ABSTRACT

Integrated SOFC/GT Systems with Improved Dynamic Capabilities for Mobile Applications

by

Zhenzhong Jia

Chair: Jing Sun

This work is focused on developing control and system integration solutions to achieve rapid and reliable load following operation of solid oxide fuel cell/gas turbine (SOFC/GT) systems for mobile applications. Both the traditional recuperating-SOFC/GT system and the newly proposed sprinter-SOFC/GT system are studied through model-based methodologies. It is shown that solutions developed in this research could enhance system performance and meet operating objectives.

For the recuperating system, the generator/motor (G/M) dual mode operation and its implications are investigated. Active shaft load control is used to manage transients by: (a) pre-conditioning of G/M power for load step-up transients; and (b) absorbing the excessive power through motoring operation for load step-down transients. Feedback and optimization algorithms are developed. By taking advantage of the dual operating G/M, better trade-offs between power tracking and thermal safety can be achieved, the battery requirements can be reduced and system performance can be enhanced.

The sprinter-SOFC/GT system, which has far superior load following capability than traditional systems, is proposed in this research. In the system, the SOFC operated at constant temperature provides only the baseline power with high efficiency while the GT-generator's transient capability will be fully explored for fast dynamic load following. System design and control framework suited for the proposed system are investigated.

An SOFC operational strategy is derived to keep fairly constant SOFC power and temperature over the entire load range. A design procedure is also developed to determine various component sizes. The "actual" operational envelope is determined by integrating the SOFC power/temperature constraints with safety factors. An optimization problem is proposed to determine the optimal feed-forward operation map.

Control analysis and feedback design are presented for the sprinter system. The stability of steady-state operation is studied through numerical simulations and linearized analysis of a simplified "2-state" model. Open-loop instability was identified for the low and medium airflow regions. Open-loop analysis and relative gain array (RGA) technique are used to gain insights on system operation and input-output interactions. Feedback control design is performed to address transient issues. The sprinter system achieves far superior performance than its recuperating counterpart for fast and safe load following.

CHAPTER 1
Introduction

1.1 Overview of Integrated SOFC/GT Systems

Integrating high temperature (~1000K) solid oxide fuel cells (SOFCs) with a gas turbine (GT) is an effective strategy to develop highly efficient and clean (i.e., ultra-low emissions) power generation solutions. By leveraging the complementary features of these two power sources, i.e., SOFC and GT, the integrated system could achieve up to 70% theoretical fuel-to-electric efficiency for stationary applications [1] - [5]. Several SOFC/GT-based power plants have been successfully installed in practice. For example, Siemens-Westinghouse demonstrated a 220kWe (i.e., 220kW electric power) unit at the University of California, Irvine (UC-Irvine) [3] and a 300kWe unit at Pittsburgh [31]. Around 53% overall system efficiency has been achieved by the 220kWe system during the continuous test operation for more than 3000 hours [3]. Outside the United States, the Mitsubishi Heavy Industries, Ltd. (MHI, Japan) also tested a 75kWe SOFC-MGT (i.e., micro-GT) facility and a 200kWe class system [32].

Besides their high system efficiency and low emissions, other main advantages of the integrated SOFC/GT systems include:

(1) Features related to the high-temperature SOFCs are preserved. No noble catalyst such as platinum is required [24]. The internal reforming capability [4] and flexible fueling options [41] help to reduce the complexity and cost of the fuel processing system.

(2) Even higher efficiency can be achieved by recuperating the other wasted energy from the SOFC exhaust through the catalytic burner and GT [4], [24].

(3) High power density, which is critical for mobile applications, can be achieved [4].

(4) The hybrid systems scale easily and have inherent advantage in CO_2 separation for carbon capture and sequestration/utilization [4], [41].

Due to the aforementioned benefits, the SOFC/GT system has been considered as a promising power solution for many mobile applications, e.g., auxiliary power units (APUs) for ground vehicles [6], [7] and aircrafts [8], the primary propulsion system for mid-sized vehicles [9] and marine power generations [10], [11]. SOFC/GT-based APU systems are able to provide electrical power for auxiliary devices independent of engine operation, bringing many practical benefits [24]. For example, using SOFC/GT-based APUs in heavy-duty trucks can greatly reduce the engine idling time, thus reducing fuel costs and emissions. Delphi expects that ~30% overall efficiency can be achieved by its SOFC-based APU (note: w/o GT), which is developed for idle reduction [79] regulations [42]. In our cooperative project with US ARMY TARDEC, model-based analysis shows that adding a recuperating GT improves the efficiency of a 5kW-class APU from 35% to 40% for military ground vehicles [7]. In [8], the author claimed that about 63% efficiency can be achieved by the 440kW-class APU system developed for aircrafts. In [9], model-based analysis indicates that around 55% overall efficiency is attainable for a 75kW-class SOFC/GT electrical propulsion system designed for mid-sized cars.

The SOFC/GT system is also a promising clean and efficient power generation solution to provide both propulsion and auxiliary service power for marine applications [10], [11]. For example, for vessels running at hotel mode in harbors, SOFC/GT-based APU systems can provide electricity with high efficiency and low emissions. Meanwhile, to improve efficiency and sustainability of vessels with reduced emissions (note: ships contribute 4.5% to global CO_2 emissions [43]), the integrated SOFC/GT system has been considered as the primary power source for both civilian, e.g., primary propulsion system for a LNG (liquefied natural gas) carrier [44], and military, e.g., the combined heat and power (CHP) generation for military sealift ships [11], applications.

Although the SOFC/GT concept is very appealing for mobile applications from the efficiency point of view, its feasibility depends critically on the system's dynamic characteristics and load following performance. However, many studies have shown that the SOFC/GT system has very limited dynamic capability due to system characteristics, e.g., large thermal inertia of the SOFC stack, stringent operation requirements [13], [14] for operating safety considerations and closed thermal/mechanical couplings [7]. Detailed

analysis of operation challenges of the SOFC/GT system for mobile applications and the overview of mitigating strategies are presented in Section 1.3.

In this dissertation, in order to achieve fast, safe and efficient load following for mobile applications, we focus on developing control and system integration solutions to improve the dynamic capabilities of integrated SOFC/GT systems. The remainder of this chapter is organized as follows: Section 1.2 presents the SOFC/GT system configuration and operational principles. Section 1.3 elucidates the operational challenges and control strategies for mobile applications. Dissertation overview and contributions are presented in Section 1.4 and Section 1.5, respectively.

1.2 System Configuration and Operational Principles

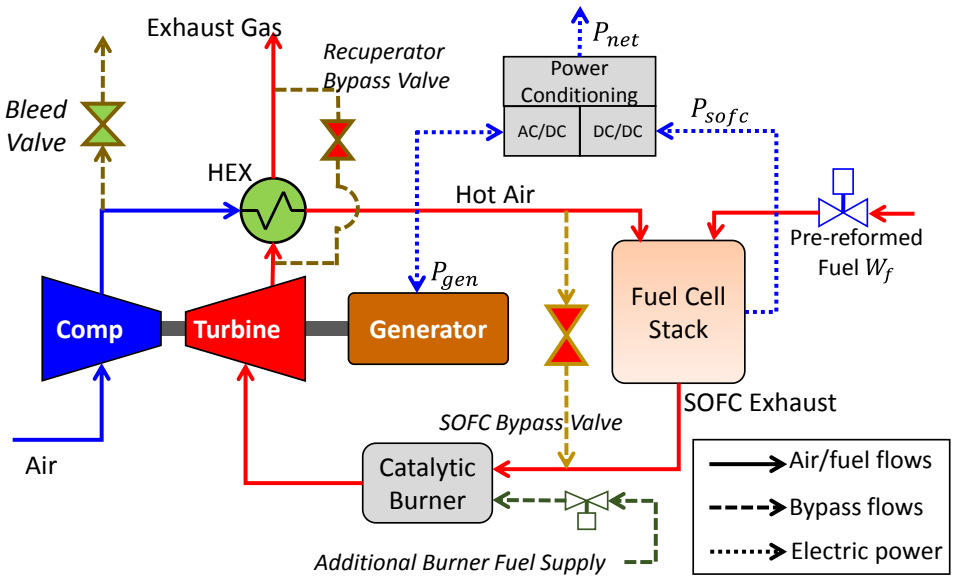

Figure 1.1: The hybrid SOFC/GT system configuration. Note that the "basic system configuration" discussed in this dissertation does not include any bypass valve.

Figure 1.1 presents the configuration of a representative SOFC/GT system. The key system components include an SOFC stack, a catalytic burner (CB), a heat exchanger (HEX), and a GT-generator where a compressor, a turbine and a generator are connected by a mechanical shaft. During operations, the pre-heated air is supplied to the cathode side of the SOFC, while pre-reformed fuel is fed to the anode side. The high-temperature

exhaust from the SOFC can be fed into the CB where the unused fuel is burned to further increase the temperature and thermal energy of the high temperature SOFC exhaust flow, which will be used to drive the turbine. This provides a mechanism [4] to recuperate the exhaust energy for improved system efficiency. The turbine drives both the compressor (delivers air into the SOFC stack) and the generator (produces additional electric power) through a mechanical shaft. The high-temperature turbine exhaust then passes through the HEX to pre-heat the air supplied to the SOFC.

If the bypass valves are excluded from the SOFC/GT system in Figure 1.1, the remaining layout is the most commonly used system setup reported in the literature [4], [14], [21]. It is referred to as the "basic system configuration" throughout this dissertation. There are many variant system setups, e.g., system with a dual-spool GT [4] and multiple HEXs. In order to achieve improved performances, the basic system setup could also be augmented with additional components and functionalities, e.g., various bypass valves [4], independent fuel supplying system to the catalytic burner [4], [15], and variable geometry compressor/turbine (VGC/VGT) [16], [17].

In particular, there might be a mismatch between the desired airflow for the SOFC and that supplied by the GT, leading to over-cooling or over-heating of the SOFC. In this case, bypass valves [18] or a heater/cooler [19] are used to extend the operating range at the expense of efficiency and complexity [17]. For example, an SOFC bypass valve and a recuperator bypass valve (see Figure 1.1) have been used in the Siemens-Westinghouse test facility to regulate the inlet air flow rate and temperature, respectively [4]. Similar valves have also been utilized in the Department of Energy Hyper (Hybrid Performance Project) hardware-in-the-loop (HIL) simulation facility [20].

Given that the additional components used in the augmented systems will further complicate the system operation and increase the system size (which is very critical for mobile applications), capital cost and malfunction rate, one objective of this study is to keep the integrated system as simple as possible [14] while achieve efficient and reliable operations. Meanwhile, instead of explicitly modeling the external fuel reformer such as the on-board JP8 fuel reformer, an alternative approach is adopted, by assuming that the pre-reformed fuel is a mixture of multiple species [34] (e.g., CH_4, CO, and H_2), where concentration ratios could be varied to reflect different pre-reforming results. In doing so,

we can simplify the system analysis and focus on the dynamic couplings of the SOFC and the GT-generator [7] in this research.

1.3 Operation Challenges and Strategies for Mobile Applications

1.3.1 Operation Challenges

Fast load following and safe transient operation are considered to be the most critical factors for reliable operation of SOFC/GT systems for mobile applications [14]. However, both model-based analysis [14], [15] and experimental studies [4] reveal that the integrated SOFC/GT system has very limited transient capabilities, which limit its widespread applications to mobile platforms [7].

First, the large thermal inertia of the SOFC stack and the slow fuel path dynamics associated with the fuel processing/delivery system, often lead to slow transient responses [7]. For example, typical power transients might take several minutes or longer while the thermal transients might take hours to settle [14]. Although batteries or ultra-capacitors are commonly used to provide the bridging power during load transients, it is desirable for the hybrid SOFC/GT system to have fast load following capability to meet the desired size target without relying on an oversized energy storage system [7]. This is particularly important for mobile applications with stringent space limits.

Second, although the SOFC is generally able to respond to quick (e.g., 10 seconds [80]) load changes, a sudden large change in SOFC operating condition could seriously impact the components and their life cycle due to thermally induced stresses [14]. Hence, fast changes in SOFC operation are usually prohibited in practice. Moreover, to limit the SOFC thermal fatigue and degradation, it is preferred to keep the SOFC temperature at constant levels for efficient and long life-cycle operation [1], [14]. Therefore, it becomes very challenging to achieve fast load following while enforcing effective thermal safety management [7], [14].

Third, the closed thermal and mechanical couplings, which are essential for high system efficiency operation, make fast and safe load following extremely challenging [7]. In fact, the operational challenges in SOFC/GT systems arise from two competing goals, namely, maximizing system efficiency versus fast and safe load transients. For instance,

the optimal operating points are located at the boundary of the feasible operation region to maximize power production for a given fuel supply. However, this leaves no sufficient safety margin for fast and safe load transient operations. A phenomenon which has been observed in both real systems and model-based analysis is the temporary large and rapid shaft speed drop during transients that might eventually lead to system shutdown [15]. Therefore, effective strategies to extend dynamic capabilities of SOFC/GT systems are becoming critical enablers for their widespread applications to mobile platforms [7].

1.3.2 Mitigating strategies for Recuperating Systems

Most papers found in the literature focus on the design [14], [21] and optimization [22] of recuperating-SOFC/GT (referred to as R-SOFC/GT in this dissertation) systems, in which a recuperating GT, whose primary function is to recuperate the exhaust energy, is integrated with the SOFC. In comparison, the control and system integration solutions, especially those aimed at addressing aforementioned operating challenges, have not been fully explored [6], [14]. Currently, strategies that mitigate the limited SOFC/GT transient capabilities mainly focus on two directions: one is to find effective operating strategies without modifying the existing system configuration; the other on augmenting the system with additional components and functionalities through system integrations [7].

For the first approach, many control strategies have been developed. In [48], the impact of GT speed on dynamic performance and controllability of the SOFC/GT system is investigated. A multi-loop feedback control scheme has been developed by controlling the current, fuel, and airflow for safe part-load operations in [13], [14]. Even though there are strong interactions among different loops in the system, the multi-loop control design could be made stable due to the time scale separation between those loops. The results are presented in Figure 5.23 and Figure 5.24 of this dissertation. Similar feedback control strategies can also be found in [45] - [47], [49]. Besides the integrated SOFC/GT system, feedback control strategies have also been used to improve the transient performance of the SOFC stack, i.e., the primary power source of the traditional R-SOFC/GT system, as demonstrated in [50] - [52].

Optimization-based controls have also been studied for the R-SOFC/GT systems. For instance, an incremental step reference governor (IS-RG) has been developed in [15]

for fast load step-up operations. At each sampling time, the IS-RG controller determines the maximum permissible generator power while avoiding potential system shutdown. In addition, model predictive control (MPC) strategies, which can handle various operation constraints, e.g., the constraints on SOFC temperature and fuel utilization, have also been developed for coordinated power and thermal management [12], [53].

For the second approach, the uses of variable geometry compressor/turbine (i.e., VGC/VGT), bypass valves, and energy storages have been investigated. In [16], the VGT is used to address the shutdown problem and improve the transient performance during abrupt load changes. Similar techniques, e.g., the VGC, have also been used to improve the part-load performance [17]. In the SOFC/GT system, the operation of fast component, i.e., the GT, is primarily limited by its air delivery functions and cannot contribute much to transient operations. Bypass valves are used in [4] to mitigate this problem. However, the added components complicate the system design, control, and operation.

In CHAPTER 3, an alternative method, i.e., the generator/motor (G/M) dual mode operation, is proposed to improve the airflow control authority and transient performance of the R-SOFC/GT system. In particular, without adding new components and by taking full advantage of the bi-directional operation of the electric machine (i.e., G/M), we will show that improved load following and thermal management can be achieved, power and energy requirements for the battery, which provides the bridging power in load transients, can be reduced, and overall system performance can be enhanced [7].

However, one common problem of the conventional R-SOFC/GT systems is that their transient performance, e.g., load and thermal transients, is dominated by transient limitations of the SOFC, which is the primary power source of R-SOFC/GT systems. The GT-generator, i.e., the component with fast shaft dynamics, is mainly used as an energy recovery device (ERD) to recuperate the otherwise wasted SOFC exhaust energy to drive the compressor for air delivery (primary task) while limited remaining shaft power can be used to drive the generator to produce additional electric power, which only contributes less than 20% of the system net power. Moreover, the power generation capability of the GT-generator is limited by its size, which is often optimized to match the SOFC in the R-SOFC/GT system [17]. Therefore, one cannot take advantage of the fast dynamics of the GT-generator for improved transient operations in the conventional R-SOFC/GT systems.

This motivates us to pursue a new type of SOFC/GT system for mobile applications, as will be investigated in the following sections.

1.3.3 Sprinter System: Concept and Research Problems

To meet the fast and safe load following requirements for mobile applications, a sprinter-SOFC/GT (referred to as S-SOFC/GT) system, is pursued in this dissertation. As shown in Figure 1.2, the recuperating and sprinter SOFC/GT systems have the same base components and configuration. The main differences are: (1) the relative size of the GT-generator with respect to the SOFC; and (2) the operation principles.

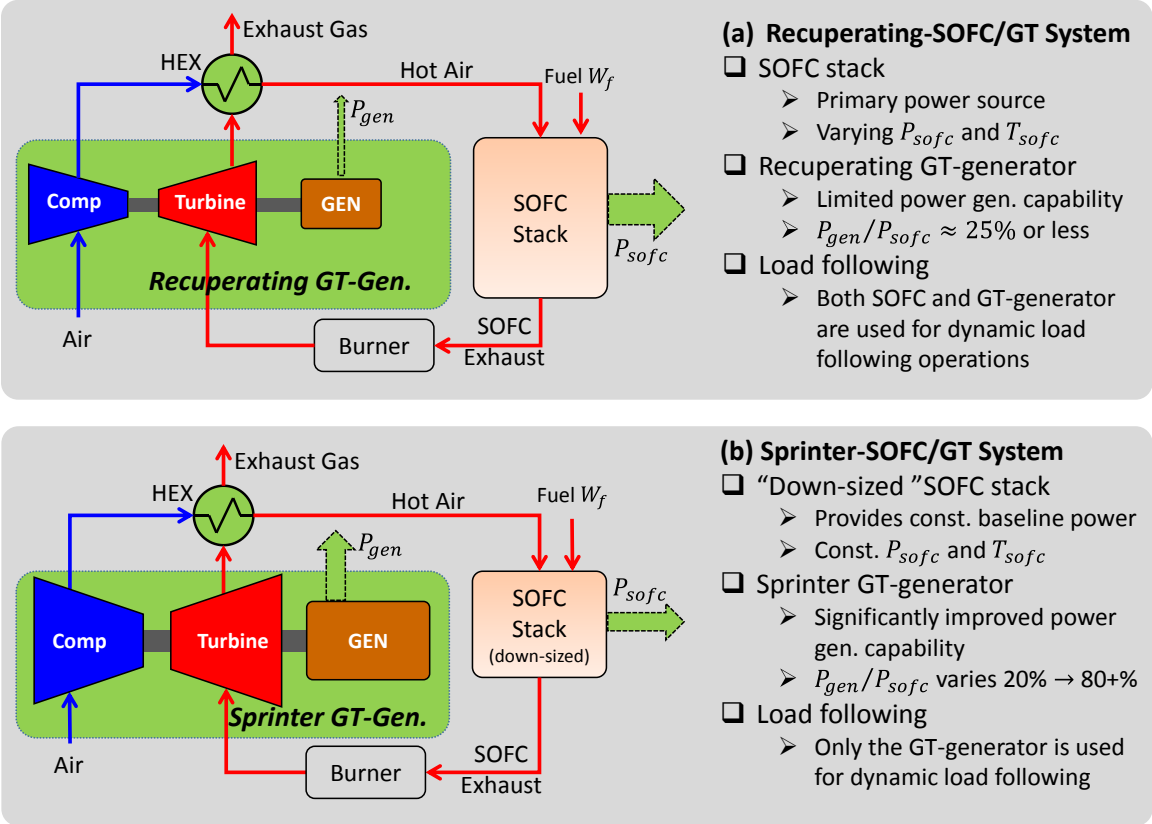

Figure 1.2: The conventional recuperating-SOFC/GT (R-SOFC/GT) system versus the proposed sprinter-SOFC/GT (S-SOFC/GT) system, where P_{sofc}, P_{gen} and T_{sofc} refer to SOFC power, generator power and SOFC temperature, respectively. One main difference between these two systems is the relative size between the SOFC and the GT-generator.

In the proposed S-SOFC/GT system, a "down-sized" SOFC stack that is operated at relatively constant temperature is integrated with a sprinter GT-generator assembly.

This sprinter GT-generator could produce a considerable amount of electrical power very quickly to meet the desired power demand. In the proposed system, only the fast dynamic component, i.e., the GT-generator, will be used for dynamic load following, while the SOFC is mainly used to provide the baseline power with high efficiency. Compared with traditional R-SOFC/GT systems, in which both the SOFC and GT-generator are used for dynamic load following operation, the proposed S-SOFC/GT system has the potential to achieve: (1) fast load following by taking full advantage of the fast dynamic capability of the GT-generator; (2) efficient and long life-cycle operation by running the SOFC cells at fairly constant temperature [39].

To the author's best knowledge, the S-SOFC/GT concept proposed herein has not been studied in the literature. Given the differences between the recuperating and sprinter systems (see Figure 1.2), the system design, dynamic operation and controls associated with the proposed S-SOFC/GT system need to be investigated. The design procedure for the R-SOFC/GT system is not well suited for the S-SOFC/GT system for several reasons. First, the design process from the full-load design point to part-load off-design analysis does not apply to the S-SOFC/GT system because at least two design points, i.e., the baseline and the peak load operating points, need to be determined. Second, the sprinter system has an additional design objective of keeping fairly constant SOFC temperature over all load conditions. Third, design guidelines for the traditional systems, e.g., typical values for fuel utilization and power split ratio, cannot be directly applied because their values will vary greatly over the entire operation range in the sprinter system. Fourth, the new system has significantly extended operating ranges for the GT-generator in terms of air/gas mass flows, pressures, temperatures and generator power. Hence, system design procedure suited for the proposed S-SOFC/GT systems needs to be developed.

The proposed system also has different control implications. For example, in the proposed system, the load following and airflow management, which dominates the cell temperature, are both controlled by the generator. This poses different transient operation challenges since the airflow and the generator power will vary greatly over the entire load range, as shown in Section 4.4. Hence, specific control algorithms need to be developed for the S-SOFC/GT system to achieve fast transient operation while maintaining constant SOFC power and temperature over a wide load range.

1.4 Dissertation Overview

This work aims to develop control and system integration solutions to achieve fast and safe load following operation of SOFC/GT systems for mobile applications. To this end, both the R-SOFC/GT system and the S-SOFC/GT system are investigated through model-based methodologies. For the R-SOFC/GT system, the G/M dual mode operation and its implications on system transient performance and energy storage requirements are studied. For the S-SOFC/GT system, model-based analysis is applied to gain fundamental understanding on the system efficiency, steady-state and transient operations as well as strategies for fast and safe load following through control design.

To support the model-based studies, a dynamic model of the integrated SOFC/GT system is developed in CHAPTER 2. The modeling principles and governing equations for the main system components, e.g., tubular SOFCs, turbomachinery, catalytic burner and heat exchanger, are presented. The system model is derived by integrating models of those individual components. The finite volume method [23], [24] is applied to describe the spatial distributions of parameters along the SOFC stack. The catalytic burner model is developed by using mass and energy conservation and the ideal gas law [39]. Modeling of the heat exchanger is developed based on those commonly used in thermodynamics. Moreover, the tubular SOFC model and the turbomachinery model are validated against experimental data reported in the literature. The integrated SOFC/GT system model lays foundation for subsequent design and control studies.

In order to improve transient performance, the R-SOFC/GT system is augmented by a battery and an electric machine capable of operating in both generator and motor mode in CHAPTER 3. Through case studies of a 5kW-class APU system, this chapter focuses on studying the G/M dual mode operation and its control and design implications on transient performance and battery requirements. Active shaft load control is used to manage transients by: (1) pre-conditioning of G/M power for load step-up operations; and (2) absorbing the excessive power through motoring mode operation for load step-down operations. Feedback control and optimization algorithms are developed while numerical simulations are carried out to show their effectiveness and computational efficiency. The

G/M dual mode operation is evaluated in terms of load following performance, thermal safety and battery requirements.

The remaining chapters (chapter 4-5) are devoted to the new S-SOFC/GT system, which is designed to tackle the fundamental limitations of R-SOFC/GT systems. Model-based analysis is applied to an example system, which is intended to be used as a primary electrical propulsion system for military vehicles, to gain fundamental understanding on system design and control. In particular, we investigate the feasibility problem, whether the S-SOFC/GT system has the ability to achieve desired design objectives of (1) keeping constant SOFC power and temperature over the entire load range; and (2) achieving fast and safe load following. System design procedure and control algorithms associated with the proposed S-SOFC/GT system will also be developed.

To this end, an operational strategy is proposed in CHAPTER 4 to maintain fairly constant SOFC power and temperature over the whole load range. Based on this strategy, a design procedure that helps to size different components is developed for the sprinter system. The "actual" operating envelope is determined by integrating the constant SOFC power and temperature constraints with multiple operational safety factors, as shown in Section 4.4. A constrained optimization problem is formulated in Section 4.5 to identify the optimal feed-forward map, which is used to schedule the actuators and power split for different power demands. The S-SOFC/GT system is compared with the conventional R-SOFC/GT system in terms of feasible operation region, steady-state feedforward map and system performance, as well as the operating safety margin.

Stability analysis and feedback control design are presented in CHAPTER 5 for the S-SOFC/GT system. In Section 5.1, BIBO stability of steady-state operation points is evaluated through numerical simulations and is further investigated by linearized analysis of a simplified model. System analyses are carried out in Section 5.2 to gain insights on system transients and operation challenges. In Section 5.3, feedback control design suited to the S-SOFC/GT system is performed for both load step-up and step-down transients. In the end, the transient performance of the S-SOFC/GT system is compared with the "state-of-the-art" results for the R-SOFC/GT system reported in the literature.

Finally, a summary of the dissertation is given in CHAPTER 6 and the important conclusions are highlighted.

1.5 Contributions

The contributions of this dissertation on system modeling, configuration analysis and control design of integrated SOFC/GT systems with improved transient capabilities for mobile applications are summarized as follows:

1. Dynamic models are developed for the integrated SOFC/GT system. Modeling of key components such as SOFCs, turbomachinery, catalytic burner and heat exchanger are discussed. Finite volume method is used to discretize the tubular SOFC while curve fitting techniques are used to express the GT maps in compact functional forms. The SOFC and GT models are validated against experimental data available from the open literature. Finally, individual component models are integrated to represent the overall system dynamics. The modeling effort leads to a comprehensive model library, which can be used for the studies of hybrid SOFC/GT systems.
2. For the R-SOFC/GT system, G/M dual mode operation and its implications on system operation and energy storage requirements are investigated. Active shaft load control is achieved through pre-conditioning operation of G/M load and motoring operation for load step-up and step-down transients, respectively. Model-based analysis reveals that by taking full advantage of the dual mode operation of the G/M, better trade-offs between power tracking and thermal safety can be achieved, the battery power/energy requirements can be reduced, and overall system performance can be enhanced. The findings provide a practical way to enhance the transient capabilities of conventional R-SOFC/GT systems without modifying the base components or system layout.
3. Operational strategy and design procedure well-suited to the S-SOFC/GT system are developed. In particular, through model-based analysis, an SOFC operating strategy is derived to coordinate multiple inputs to keep fairly constant SOFC temperature and power over the entire load range, thereby establishing the feasibility of the proposed S-SOFC/GT system. A design procedure, which helps to determine component sizes and the approximated steady-state operation line from the given power requirements, is developed for the proposed S-SOFC/GT system.
4. Feasible operating regimes and steady-state performance are studied for the proposed S-SOFC/GT system. The “actual” operating envelope is determined by integrating the

constant SOFC power/temperature constraints with those pertinent to different safety factors. Steady-state trends of various variables, such as cell voltage, CB temperature and generator power, are analyzed. A constrained optimization problem is formulated to determine the static feed-forward map of the S-SOFC/GT system. The results offer guidelines to schedule the actuators to achieve maximum efficiency for different net power demands while satisfying the safety and operational constraints. Finally, the S-SOFC/GT system is compared with the R-SOFC/GT system in terms of safe/feasible operation envelope, static feedforward map and performance.

5. Stability analysis and feedback control design are performed for the new S-SOFC/GT system. The BIBO stability with respect to the generator load is investigated through numerical simulations and linearized system analysis. Shaft speed control is proposed to stabilize the system at desired operating points. Meanwhile, open-loop analysis and relative gain array (RGA) analysis are used to gain insights on system transients, loop interactions and operation challenges. Based on the characteristics of the S-SOFC/GT system, a cascade feedforward-feedback control strategy is developed for the sprinter system. It is shown, through numerical simulations, that by taking full advantage of the GT-generator's fast dynamic capabilities, the proposed S-SOFC/GT system could achieve far superior load following performance, compared with the "state-of-the-art" results for the conventional R-SOFC/GT system.

CHAPTER 2
Modeling of Integrated SOFC/GT Systems

Due to the limited availability of SOFC/GT experiment facilities and the lack of experimental data in the open literature, simulation-based study remains the only viable option for most research groups [14], [39]. There are many publications focusing on the modeling of hybrid SOFC/GT systems. For example, detailed reviews of dynamic SOFC models and the integrated SOFC/GT system models can be found in [5] and [33], each of which reviews more than 100 papers. Given the difficulties in system-level experimental validations and the importance of model-based analysis, it is critical to validate the key system components with respect to experiment data. Otherwise, the numerical simulation might produce questionable results. In this chapter, we will describe the modeling of the integrated SOFC/GT system and key components, including the SOFC, turbomachinery, catalytic burner, and heat exchanger. We will also delineate how these component models are validated with data reported in the open literature. Other components, such as the fuel reformer [14], are not included in order to focus on the dynamic couplings between the SOFC stack and the GT-generator [39] throughout this dissertation.

2.1 Modeling of Tubular SOFCs

2.1.1 Tubular SOFC cells

In this research, the tubular SOFC cells developed by Siemens-Westinghouse are selected due to their advantages in thermal expansion and gas sealing [23]. As shown in Figure 2.1 [54], the pre-heated air enters the injector, i.e., the air feeding tube, and travels to the closed end of the cell tube. Pre-reformed fuel enters the SOFC outside the cell tube from the closed end. The air and fuel both flow along the cell in the same direction from the closed end to the open end of the cell. This is known as a co-flow configuration [1].

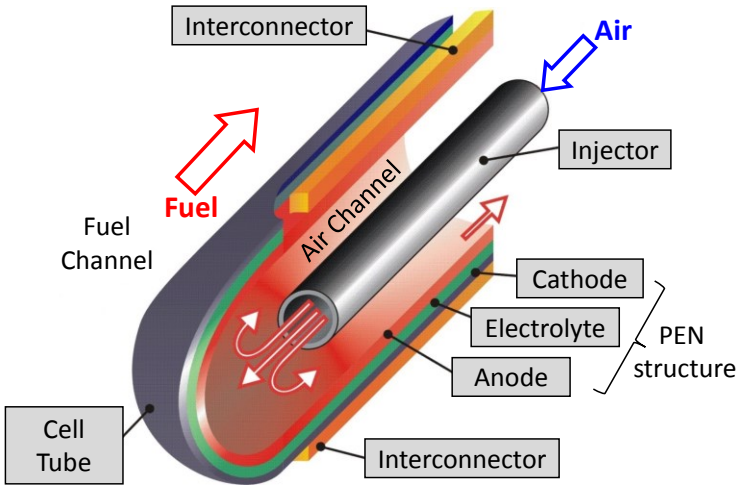

Figure 2.1: Gas flows in the co-flow tubular SOFC cell [54].

The SOFC model utilized in this work is mainly based on Oh's model [34], which was developed based on SOFC models in [23] and [24]. Moreover, a significant amount of work has been done to improve Oh's model [34], leading to close agreements between the model responses and experiment data, as will be shown in Section 2.1.5. The model is included here for a self-contained system model presentation. The model is composed of three sub-models, namely, the electro-chemical sub-model, the mass balance sub-model and the energy balance sub-model [24]. The full model is developed by integrating these sub-models as presented in the following sections.

Our SOFC modeling approach takes into account the trade-off between acceptable computational load and sufficient modeling accuracy. The following strategies have been used to reduce the complexity of the resulting model without significant compromise on the modeling accuracy. First, the anode, cathode, and electrolyte are considered as one assembly, called the PEN (Positive electrode-Electrolyte-Negative electrode) structure. Based on the physical structure, five temperature layers could be defined for the SOFC, namely, the temperatures for fuel flow, air flow, PEN, injector, and feeding air, as shown in Section 2.1.4. Second, the SOFC can be treated as a distributed parameter system to capture the spatial distribution along the flow field for variables such as the temperature, species concentration, and current density. The governing equations are described using the discretization technique, such as the finite-volume method [23], [24]. In doing so, the SOFC is divided into user-defined number (e.g., N_d) along the flow axis and each section

is modeled as a lumped parameter sub-system, i.e., variables such as temperatures and the current density are assumed to be homogeneous in each discretized unit. In this research, the tubular cell is discretized into four (i.e., N_d=4) sections [7]. Third, the fuel is assumed to be a mixture of 6 gas species, consisting of CH_4, CO, CO_2, H_2, H_2O and N_2, where the species concentrations can be varied to reflect different pre-reforming results [34].

The following assumptions, which are commonly used in the literature [14], [24], are used for developing the SOFC model in this chapter:

1. The SOFC cell is considered equipotential (i.e., all the discretized units have the same voltage) because of the high electrical conductivities of the interconnectors.
2. The current is produced only by the oxidation of H_2, and CO reacts only through the water gas shift (WGS) reaction (see Figure 2.2).
3. Ideal gas laws are applied for the bulk flows in the fuel, air and feeding air channels.
4. Adiabatic boundary conditions are applied for the SOFC by assuming that the cell is located in the middle of a large stack [14].

2.1.2 Electrochemical Sub-model

The voltage of one discretized unit of the SOFC cell can be calculated by:

$$U^j = U^j_{OCV} - \left(U^j_{ohm} + U^j_{act} + U^j_{con}\right), \qquad j = 1,2,\dots,N_d, \tag{2.1}$$

where j is the index of discretization units. U^j_{OCV} is the open circuit voltage in the jth unit. For notation simplicity, the superscript j will be omitted in the following equations. The open circuit voltage can be determined by the Nernst Equation as follows:

$$U_{OCV} = E_0 - \frac{\tilde{R}T_{PEN}}{2F} ln\left(\frac{p_{H_2O}}{p_{H_2}p_{O_2}^{0.5}}\right), \tag{2.2}$$

where $\tilde{R}$ and F are the ideal gas constant and Faraday constant, respectively; T_{PEN} is the temperature of the PEN structure; p_{H_2}, p_{O_2}, and p_{H_2O} are the partial pressures of H_2, O_2, and H_2O, respectively. The Nernst potential $E_0 \approx 1.2723 - 2.7645 \cdot 10^{-4}\, T_{PEN}$ [61].

The last three terms in Eqn. (2.1) represent various potential losses. U_{ohm} is the ohmic loss due to the electrical and ionic resistance along the current path in the SOFC. The activation loss, U_{act}, is due to the energy barrier to overcome in order for the electro-chemical reaction to occur, and can be described by the Butler-Volmer equation [24]. The concentration loss, U_{con}, reflects the over-potential due to species diffusion between the reaction site and the bulk flow in the gas channels. Expressions for these potential losses can be found in [24]. The polarization relation in each discretization unit, as denoted by the following nonlinear algebraic function, can be identified in the electro-chemical sub-model based on the local conditions, including T_{PEN} and species pressures:

$$U = f\left(i, p_{H_2}, p_{O_2}, p_{H_2O}, p_a^{tot}, T_{PEN}\right), \tag{2.3}$$

where p_a^{tot} is the total pressure of the bulk flow in the air channel while the details on Eqn. (2.3) are given in [24]. Note that there is no state in the electro-chemical sub-model.

2.1.3 Mass Balance Sub-model

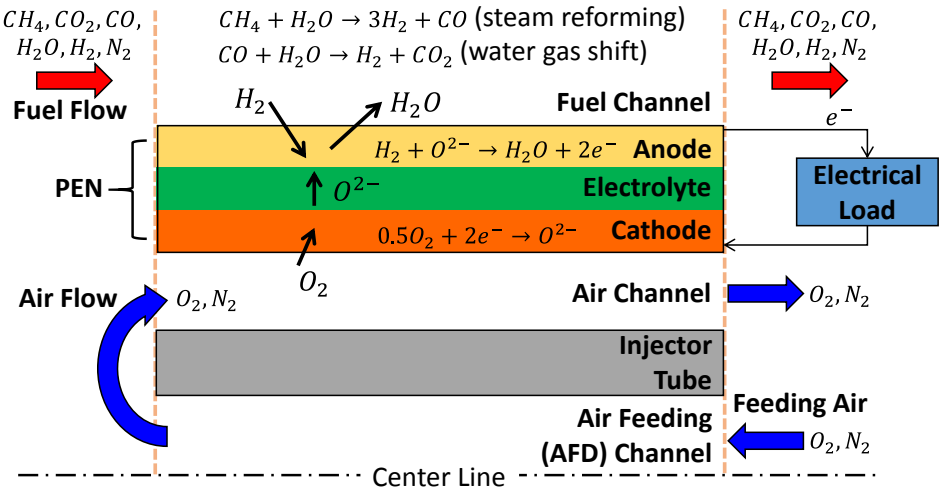

Figure 2.2: Operating principle of co-flow tubular SOFCs. The figure shows electro-chemical reactions and mass flows across one discretization unit of the SOFC cell.

The masses accumulated in the fuel and air channels are calculated in the mass balance sub-model. As shown in Figure 2.2, the chemical species considered in the fuel channel are CH_4, CO, CO_2, H_2, H_2O and N_2, while for the air channel the species are O_2

and N_2. Table 2.1 lists the reactions considered in the model. As shown in Figure 2.2, in the fuel channel, three reactions are taken into account: methane steam reforming (SR), water gas-shift (WGS), and hydrogen electro-chemical oxidation (Ox). In the air channel, only the reduction (Red) reaction from O_2 to O^{2-} ions is considered [34]. According to Faraday's law, the rates of oxidation (Ox) and reduction (Red) reactions are related to the current density as follows [24]:

$$r_{Ox} = r_{Red} = i/2F. \tag{2.4}$$

Table 2.1 Reactions considered in the SOFC model

Location	Reaction	Expression
Fuel Channel	SR	$CH_4 + H_2O \rightarrow CO + 3H_2$
	WGS	$CO + H_2O \leftrightarrow CO_2 + H_2$
Anode	Ox	$H_2 + O^{2-} \rightarrow H_2O + 2e^-$
Cathode	Red	$0.5O_2 + 2e^- \rightarrow O^{2-}$

Note that the SR reaction is slow and highly endothermic, while the WGS is fast and weakly exothermic. Thus, the reforming process is dominated by the endothermic SR reaction that requires the heat generated by the electro-chemical reaction. In this study, the formula described in Eqn. (2.5), which is widely used in the literature [24], [55], [56], is adopted for the reaction rate of the steam reforming reaction:

$$r_{SR} = 0.04274 \cdot p_{CH_4} \cdot exp\left(-\frac{E_{SR}}{\tilde{R}T_f}\right), \tag{2.5}$$

where $E_{SR} = 82kJ \cdot mol^{-1}$, and T_f is the temperature of the fuel channel. Note that r_{SR} only depends on the partial pressure of CH_4, p_{CH_4}, and fuel temperature T_f. In addition, the formula in [55] is adopted to calculate the rate of WGS reaction as follows:

$$r_{WGS} = k_{WGS} \cdot p_{CO} \cdot \left(1 - \frac{p_{CO_2}p_{H_2}}{p_{CO}p_{H_2O}K_{eq,WGS}}\right), \tag{2.6}$$

where $k_{WGS} = 0.01$, reflecting the very fast kinetics of the WGS reaction, and $K_{eq,WGS}$ is the equilibrium constant with $K_{eq,WGS} \approx exp\left(4276/T_f - 3.961\right)$ [24].

The mass balance dynamics of gas species in the bulk flow of the fuel channel for each discretization unit can be expressed as follows:

$$\dot{C}_{s_f} = \left(N_{in,s_f} - N_{out,s_f}\right)\frac{1}{V_f} + \sum_{k\in\{SR,WGS,Ox\}} v_{s_f,k} \cdot r_k \cdot \frac{1}{d_f}, \quad s_f \in \{CH_4, CO_2, CO, H_2O, H_2, N_2\}, \tag{2.7}$$

where C_{s_f} is the molar concentration of species s_f; N_{in,s_f} and N_{out,s_f} are the inlet and outlet molar flow rates of species s_f, respectively; V_f is the volume of the fuel channel in one discretization unit; $v_{s_f,k}$ is the stoichiometric coefficient of species s_f in reaction k; r_k is the rate of reaction k; and d_f is the characteristic length of the fuel channel [23]. As mentioned above, all the variables refer to the same discretization unit.

Similarly, the mass balance dynamics of the bulk flow in the air channel is:

$$\dot{C}_{s_a} = \left(N_{in,s_a} - N_{out,s_a}\right)\frac{1}{V_a} + v_{s_a,Red} \cdot \left(\frac{r_{Red}}{d_a}\right), \qquad s_a \in \{O_2, N_2\}, \tag{2.8}$$

where C_{s_a} is the molar concentration of species s_a; V_a is the volume of the fuel channel in one discretization unit; and d_a is the characteristic length of the cathode air channel.

2.1.4 Energy Balance Sub-model

The temperature dynamics in the SOFC is calculated in the energy balance sub-model [24]. The temperatures in five layers, i.e., the fuel flow (T_f), the air flow (T_a), PEN structure (T_{PEN}), the injector (T_{INJ}) and feeding air (T_{afd}), are calculated by solving the dynamic equations of the energy balance in each layer. As in Figure 2.3, the heat transfer considered in the model includes the convection between the bulk flows (i.e., fuel, air, and feeding air flows) and their surrounding solid structures, the conduction Q_{cond} in the solid layers (i.e., PEN and injector) as well as radiation Q_{rad} between PEN and injector

[23], [24]. In particular, $Q_{conv,Solid/Gas}$ indicates the conduction heat transfer between the solid structure $Solid$ and the air/gas bulk flow Gas.

The energy balance dynamics in the fuel flow can be expressed as follows:

$$\left(\sum_{s_f} c_{v,s_f} C_{s_f}\right)\frac{dT_f}{dt} = \left(Q_{in,f} - Q_{out,f}\right)\frac{1}{l} + k_{f,PEN}\left(T_{PEN} - T_f\right)\frac{1}{d_f} + r_{Ox}\left(h_{H_2O}(T_{PEN}) - h_{H_2}(T_f)\right)\frac{1}{d_f}, \quad s_f \in \{CH_4, CO_2, CO, H_2O, H_2, N_2\}, \tag{2.9}$$

where c_{v,s_f} is the heat capacity of gaseous species s_f; $Q_{in,f}$ and $Q_{out,f}$ are the inlet and outlet enthalpy flux of the fuel flow, respectively; $k_{f,PEN}$ is the coefficient of heat transfer between PEN and the fuel flow; and $h_{H_2O}(T_{PEN})$ and $h_{H_2}(T_f)$ are the specific enthalpies of H_2O at temperature T_{PEN} and of H_2 at T_f, respectively. The first term in the right hand side (RHS) of Eqn. (2.9) is due to the enthalpy flux of the bulk flow; the second term accounts for the convective heat exchange between fuel flow and PEN; the last term is caused by the enthalpy flux due to the oxidation reaction at the anode [24].

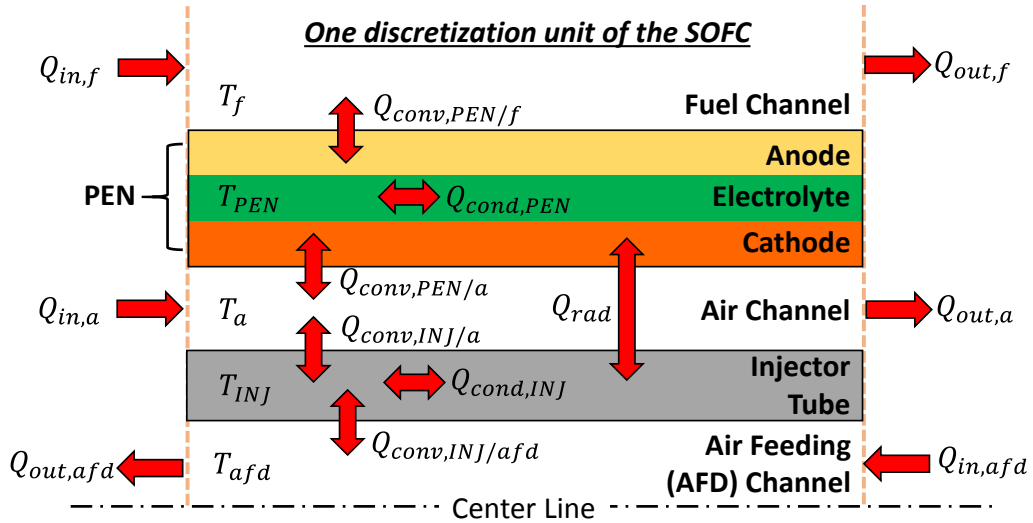

Figure 2.3: Heat transfer in the tubular SOFCs.

Similarly, for the air flow, we have:

$$\left(\sum_{s_a} c_{v,s_a} C_{s_a}\right)\frac{dT_a}{dt} = \left(Q_{in,a} - Q_{out,a}\right)\frac{1}{l} + k_{a,PEN}(T_{PEN} - T_a)\frac{1}{d_a} + k_{a,INJ}\left(T_{INJ} - T_a\right)\frac{1}{h_a} - 0.5 r_{Red} h_{O_2}(T_a)\frac{1}{d_a}, \quad s_a \in \{O_2, N_2\}, \tag{2.10}$$

where the second and the third term in RHS of Eqn. (2.10) account for the heat exchange between the air bulk flow and its surrounding solid walls; the last term is caused by the enthalpy flux due to the reduction reaction at the cathode.

The energy balance dynamics in the PEN structure can be described as follows:

$$\begin{aligned}\rho_{PEN} c_{p,PEN} \frac{dT_{PEN}}{dt} &= \frac{Q_{cond,PEN}}{l} \\ &- \left[k_{f,PEN}\left(T_{PEN} - T_f\right) + k_{a,PEN}(T_{PEN} - T_a)\right]\frac{1}{\tau_{PEN}} \\ &+ r_{Ox}\left[h_{H_2}\left(T_f\right) + 0.5 h_{O_2}(T_a) - h_{H_2O}(T_{PEN})\right]\frac{1}{\tau_{PEN}} \\ &- iU\frac{1}{\tau_{PEN}} + \left[\frac{2\sigma\left(T_{INJ}^4 - T_{PEN}^4\right)}{1/\epsilon_{INJ} + 1/\epsilon_{PEN} - 1}\right]\frac{1}{\tau_{PEN}},\end{aligned} \tag{2.11}$$

where ρ_{PEN}, $c_{p,PEN}$ and τ_{PEN} are density, specific heat capacity and thickness of the PEN structure, respectively. The first term $Q_{cond,PEN}$ accounts for the conductive heat transfer in the PEN structure and the last term in Eqn. (2.11) represents the radiation between the injector and PEN. The remaining terms account for the convective heat transfer between PEN and the surrounding flows, the enthalpy flux caused by the electro-chemical reaction and the electrical work done by the SOFC cell.

Similarly, for the injector tube, we have:

$$\rho_{INJ} c_{p,INJ} \frac{dT_{INJ}}{dt} = \frac{Q_{cond,INJ}}{l} - \left[k_{a,INJ}\left(T_{INJ} - T_a\right) + k_{afd,INJ}\left(T_{INJ} - T_{afd}\right)\right]\frac{1}{\tau_{INJ}} - \left[\frac{2\sigma\left(T_{INJ}^4 - T_{PEN}^4\right)}{1/\epsilon_{INJ} + 1/\epsilon_{PEN} - 1}\right]\frac{1}{\tau_{INJ}}, \tag{2.12}$$

where $Q_{cond,INJ}$ accounts for the conductive heat transfer in the injector and the last term in Eqn. (2.12) represents the radiation between injector and PEN. The remaining terms account for the convective heat transfer between the injector and the surrounding flows.

For the temperature T_{afd} of the feeding air inside the injector, we have:

$$c_{v,afd} C_{afd} \frac{dT_{afd}}{dt} = \frac{Q_{in,afd} - Q_{out,afd}}{l} + k_{afd,INJ}\left(T_{INJ} - T_{afd}\right)\frac{1}{d_{afd}}. \tag{2.13}$$

2.1.5 Dynamic Simulation and Model Validation

The model of the SOFC is obtained by integrating the dynamic equations of all discretization units and following the flow continuity, boundary conditions, and current distribution relations [24]. Based on the equipotential assumption, we have:

$$\begin{cases} U_{cell} = U^j, \quad j = 1,2,\ldots,N_d, \\ \sum_{j=1}^{N_d} I^j = \sum_{j=1}^{N_d} i^j A^j = I_{tot}, \end{cases} \tag{2.14}$$

where N_d is the total number of discretization units; U_{cell} is the cell voltage; I^j and I_{tot} are the currents drawn from the jth unit and the entire cell, respectively.

Given the small pressure drop along the SOFC, it is assumed that the bulk flows through the gas channels are governed by the linear orifice equation as follows:

$$W_{chn} = \alpha_{chn}\left(p_{chn}^{up} - p_{chn}^{down}\right), \qquad chn \in \{afd, a, f\}, \tag{2.15}$$

where α_{chn} is the orifice constant for the gas flow channel chn; p_{chn}^{up} and p_{chn}^{down} are the total pressure of the upper-stream and downstream flows [24].

The tubular SOFC model has been implemented in Matlab/Simulink. The model predicts various temperatures along the flow path, the gas compositions in the fuel and air channels, all the electrochemical-related variables such as voltage and current density as well as the cell efficiency and power output. The SOFC parameters, such as those for the cell materials and geometries, are taken from [23], [24]. The key operation variables for the SOFC cells are summarized in Table 2.2.

Figure 2.4 (a) shows results of different temperature profiles along the flow axis for the five temperature layers. In Figure 2.4, '0' and '1' at the x-axis represent the closed end and the open end of the cell tube (see Figure 2.1). It can be seen that the cell (PEN) temperature first increases and then decreases along the fuel/air flow direction with the maximum temperature occurring at the mid-section of the SOFC. The temperature of the feeding air increases along the injector flow direction, i.e., the direction from the open end to the closed end of the cell tube. These results capture the general trends of those in [23]. Figure 2.4 (b) presents the mole fraction profiles in the fuel/air channel streams. The consumption of hydrogen H_2, methane CH_4, and carbon monoxide CO and production of steam H_2O and carbon dioxide CO_2 can be identified along the cell as the oxidation (Ox) reaction and the internal reforming process (see Table 2.1) proceeds.

Figure 2.5 presents the cell voltage and power density as a function of current density. The simulation results are compared to the actual experimental data of Siemens-Westinghouse tubular SOFCs [1] for voltage and power output corresponding to different current density. This comparison shows a good match between the simulation model and the actual test data as the percent error between the model prediction and experimental data is less than 3% over the entire current density range.

Table 2.2 Nominal operation variables of tubular SOFCs

Key Parameters	Cell Voltage	Current Density	Cell Power	Fuel Utilization	Air Excess Ratio
Value [Unit]	0.67 [V]	2000 [A/m^2]	90 [W]	0.85	4.0
Pre-reformed Fuel	CH_4 = 1.6%, CO_2 = 1.8%, CO = 16.3%, H_2O = 3.7%, H_2 = 32.4%, N_2 = 44.2% (molar fraction ratio, data acquired from [15], [34])				

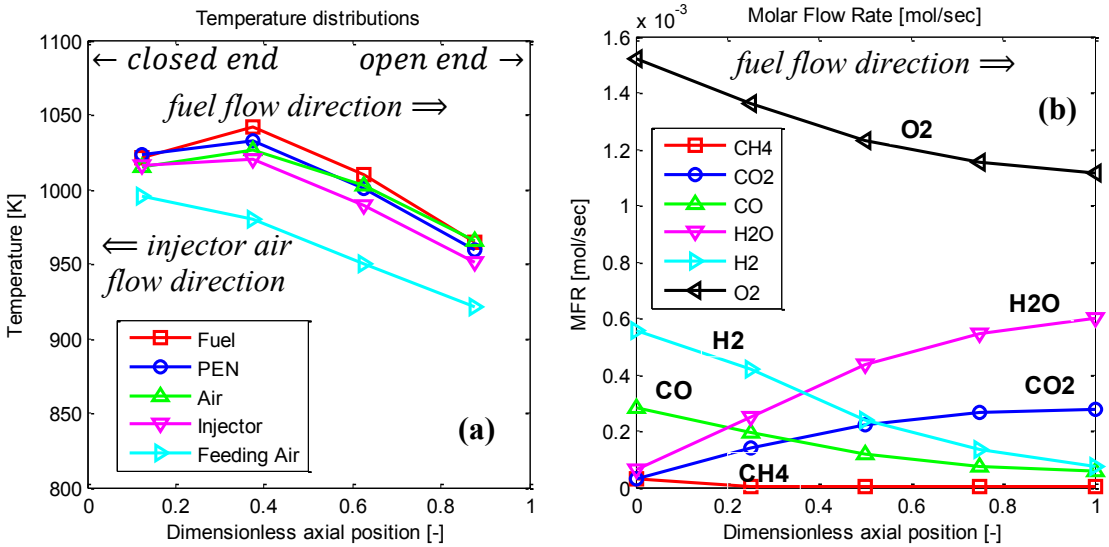

Figure 2.4: Simulation results: (a) temperature distributions and (b) molar flow rates.

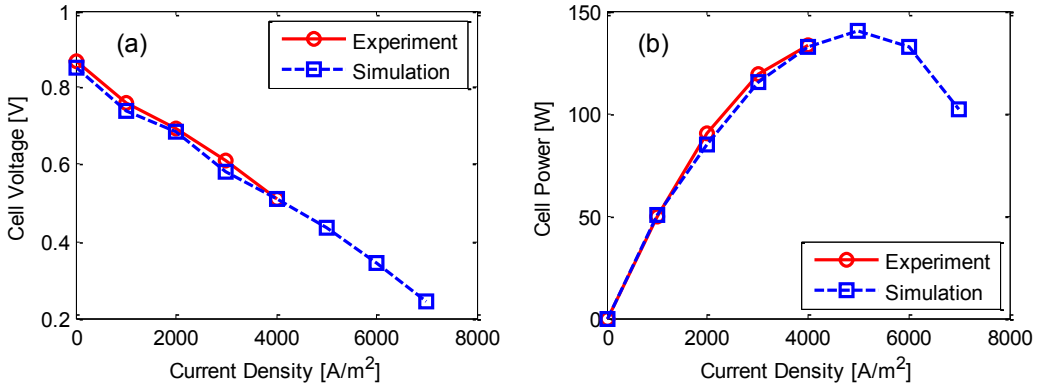

Figure 2.5: Close agreement between the simulation and experiment results: (a) cell voltage and (b) cell power versus current density.

2.2 Modeling of Turbomachinery

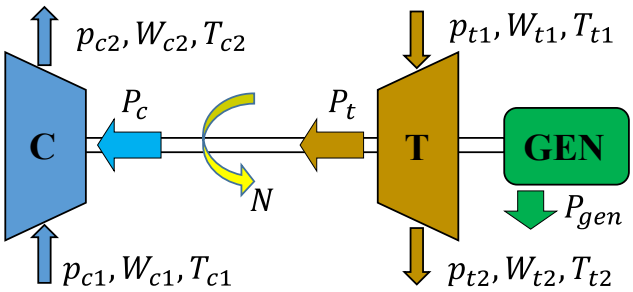

Figure 2.6: Compressor, turbine, shaft and generator schematic.

The turbomachinery model incorporates the shaft dynamics, the compressor and the turbine model. Only the shaft dynamics are considered [15], while map-based models are used for characterizing the GT. This is sufficient for SOFC/GT system modeling [14]. As shown in Figure 2.6, the main variables used in the modeling include mass flow rate W, pressure p, temperature T, and power P. The subscripts denote the component (c for compressor and t for turbine) and inlet and outlet (1 or 2, respectively). For instance, T_{t1} and p_{t1} denotes the turbine inlet temperature and turbine inlet pressure, respectively.

2.2.1 Shaft Rotational Dynamics

The shaft rotational dynamics [15] are determined by the turbine generated power P_t, the power required to drive the compressor P_c and the generator power P_{gen} as:

$$\frac{dN}{dt} = \frac{P_t \eta_m - P_c - P_{gen}}{\alpha \cdot N \cdot J}, \tag{2.16}$$

where N is the turbocharger speed, J is the turbocharger inertia, $\alpha = (2\pi/60)^2$ is a factor used to convert the shaft speed from RPM (revolution per minute) to $rad \cdot \sec^{-1}$ (radian per second), and η_m is the turbine mechanical efficiency that accounts for energy losses due to friction. In addition, instead of using Eqn. (2.16), alternative formulas presented in [35] can also be used to model the speed-dependent bearing loss terms.

2.2.2 Compressor Model

The compressor and turbine models provide the thermodynamic equations for the input-output relations of the working fluid based on the pressure ratio, shaft speed and temperature (referred to as Type-I models in [28]).

Neglecting heat losses and assuming that the specific heat coefficients of air do not change, the power P_c required to drive the compressor can be calculated as:

$$P_c = W_c c_p^{air} (T_{c2} - T_{c1}), \tag{2.17}$$

where W_c is the mass flow rate through the compressor; c_p^{air} is the constant specific heat coefficient of the air; T_{c1} and T_{c2} are the absolute temperature (i.e., with units in Kelvin) at the inlet and outlet of the compressor. The compressor outlet temperature, T_{c2}, can be calculated as follows:

$$T_{c2} = T_{c1} \cdot \left(1 + \frac{1}{\eta_c} \left(\left(\frac{p_{c2}}{p_{c1}} \right)^{\frac{\gamma-1}{\gamma}} - 1 \right) \right), \tag{2.18}$$

where γ is the heat capacity ratio, which is defined to be the ratio of the constant pressure specific heat over the constant volume specific heat as $\gamma = c_p / c_v$; η_c is the compressor efficiency, which accounts for the fact that the compression process is not isentropic [28]. Plug Eqn. (2.18) into Eqn. (2.17), the power required to drive the compressor, P_c, can be calculated as:

$$P_c = W_c c_p^{air} T_{c1} \frac{1}{\eta_c} \left(\left(\frac{p_{c2}}{p_{c1}} \right)^{\frac{\gamma-1}{\gamma}} - 1 \right). \tag{2.19}$$

The relation between speed N, mass flow W_c, and pressure ratio PR (i.e., p_{c2}/p_{c1}) are often presented in the form of compressor map. Figure 2.7 presents such a map for several speed-lines, i.e., lines of operating points of PR versus W_c for constant speeds.

For each speed-line, there are two limits for the air flow range. The upper limit is due to chocking, where the flow reaches the sound's velocity at some cross-section. No further flow increase in this region can be achieved by reducing PR and the slope of the speed-line becomes infinite beyond the choking point. The lower limit is due to the dangerous, aerodynamically/mechanically undesirable "surge" process [57]. During surging, a noisy and often violent flow process can occur, causing backflow through the compressor [28]. It may also damage the rotor bearing and sealing system, compressor driver and affect the whole operation. The value of W_c at which the surge occurs depends on the compressor characteristics and the downstream properties. Typically, this value is where the slope of the speed-line is zero or slightly positive [28]. The lower flow (i.e., the left-hand side in Figure 2.7) extremities of the speed-lines can be joined to form the so-called surge line.

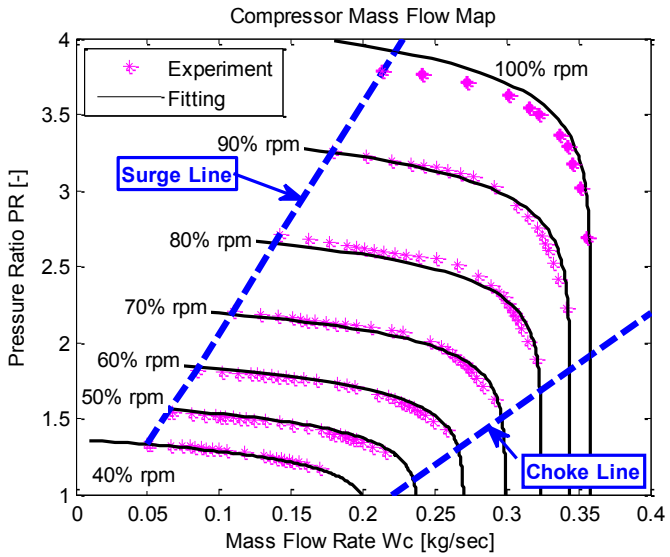

Figure 2.7: Compressor map as a function of mass flow rate and pressure ratio.

Instead of using look-up tables as in [6], it is preferred to use curve fitting [28], [29] techniques to express the GT maps in compact functional forms with coefficients determined from experiment data. This guarantees a smooth interpolation and allows reliable extension of the maps beyond the region where experimental data is available. The fitting expressions and methodology used to derive them are discussed next.

Define the normalized air mass flow rate $\widetilde{W}$, the normalized shaft speed $\widetilde{N}$ and the compressor pressure ratio PR as follows:

$$\widetilde{W} = \frac{W_c}{W_c^{design}}, \qquad \widetilde{N} = \frac{N}{N_c^{design}}, \qquad PR = \frac{p_{c2}}{p_{c1}}, \tag{2.20}$$

where W_c^{design} and N_c^{design} are the airflow rate and the shaft speed at the design point of the compressor. By using these normalized parameters, the user can apply the similarity principle [25] to scale existing compressor maps to meet specific requirements without repeating the curve fitting process or changing the already-fitted coefficients. Analogous to the Zero Slope Line Method (ZSLM) in [28], the flow parameter $\widetilde{W}$ can be expressed as a function of pressure ratio PR and the normalized speed $\widetilde{N}$, as explained as follows.

First, the curve connecting the maximum mass flows on each speed line, i.e., the choke line in Figure 2.7, can be characterized as follows:

$$\begin{cases} \widetilde{W}_{top} = f_{Wtop}(\widetilde{N}) = p_2\widetilde{N}^2 + p_1\widetilde{N} + p_0, \\ PR_{top} = f_{PRtop}(\widetilde{W}_{top}) = c_a\widetilde{W}_{top}^{c_b} + c_c, \end{cases} \tag{2.21}$$

where PR_{top} is the pressure ratio corresponding to the maximum mass flow $\widetilde{W}_{top}$ at each speed-line in the compressor map. Then, the $PR{\sim}\widetilde{W}$ relation for the speed-lines can be modeled as the following exponential function [28]:

$$\frac{\widetilde{W}}{\widetilde{W}_{top}} = 1 + q_0 \exp(q_1\widetilde{N})\left(1 - exp\left(k\left(\frac{PR}{PR_{top}} - 1\right)\right)\right), \tag{2.22}$$

where k, q_0 and q_1 are constant coefficients to be determined from the compressor data-sheet by using curve-fitting techniques, e.g., Matlab Curve Fitting Toolbox.

In order to avoid the dangerous surge process, the compressor surge margin K_{SM}, as defined in Eqn. (2.23) , should always be kept above 1.05-1.10 [36].

$$K_{SM} = \frac{(PR/W_c)_{surge}}{PR/W_c}, \tag{2.23}$$

where $(PR/W_c)_{surge}$ is the value of PR/W_c where compressor surging occurs.

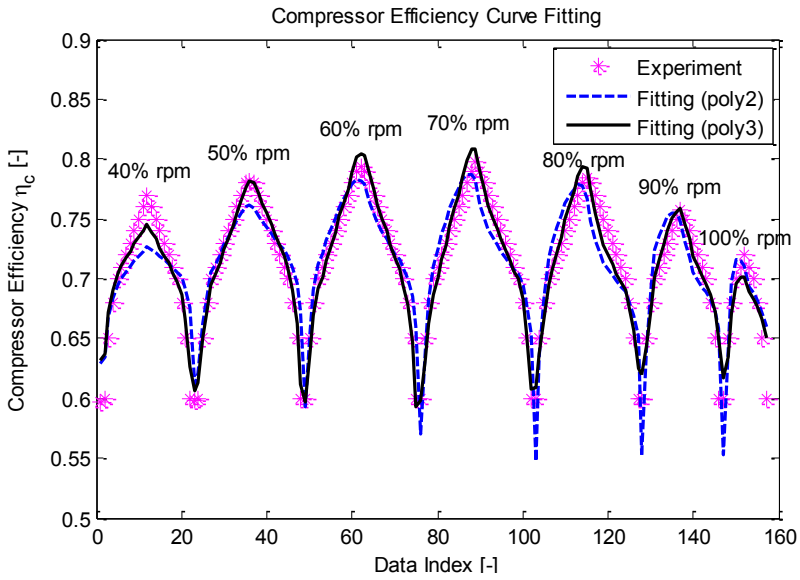

Figure 2.8: Curve fitting of the compressor efficiency map.

Instead of representing the compressor efficiency in the form of look-up tables as in [58], it is preferred to use curve fitting to model the efficiency map. Analogous to [29], the compressor efficiency can be expressed as a second-order polynomial function as:

$$\eta_{comp} = f_{\eta_{comp}}(\widetilde{N}, \widetilde{W}) = e_0 + e_1\widetilde{N} + e_2\widetilde{N}^2 + e_3\widetilde{W} + e_4\widetilde{W}^2 + e_5\widetilde{N}\widetilde{W}, \tag{2.24}$$

where constant coefficients e_i's can be determined by weighted least square method [59].

As shown in Figure 2.7, good agreement between experiment data and the curve fitting results has been achieved for the Garrett [30] GTX2867R centrifugal compressor by using Eqn. (2.20) - Eqn. (2.22). The second-order polynomial in Eqn. (2.24) has been extended to the third order (the expression is not shown here) for better fitting results of the compressor efficiency, as shown in Figure 2.8. The compressor map in Figure 2.7 and Figure 2.8 will be used for the sprinter-SOFC/GT system in this dissertation.

2.2.3 Turbine Model

The turbine is powered by the energy from the SOFC exhaust. Neglecting the heat transfer and treating the exhaust gas as an ideal gas with constant specific heat, the power output of the turbine, P_t, can be obtained from the first law of thermodynamics, as:

$$P_t = W_t c_p (T_{t1} - T_{t2}), \tag{2.25}$$

where W_t is the mass flow rate though the turbine; c_p is the specific heat capacity of the exhaust gas; T_{t1} and T_{t2} are the inlet and outlet temperatures of the turbine, respectively. Note that Eqn. (2.25) has the same form as Eqn. (2.17).

Let η_t denote the isentropic efficiency of the turbine, which accounts for the fact that the expansion process is not isentropic [28]. Similar to the compressor case, we can get the following expressions for the turbine outlet temperature and turbine power:

$$T_{t2} = T_{t1} \cdot \left(1 - \eta_t \left(1 - \left(\frac{p_{t2}}{p_{t1}} \right)^{\frac{\gamma_t - 1}{\gamma_t}} \right) \right), \tag{2.26}$$

$$P_t = W_t c_p T_{t1} \eta_t \left(1 - \left(\frac{p_{t2}}{p_{t1}} \right)^{\frac{\gamma_t - 1}{\gamma_t}} \right), \tag{2.27}$$

where γ_t is the heat capacity ratio of the exhaust gas. It should be noted that variation of the heat capacity ratio values (due to the change of exhaust gas compositions) can often be neglected for the integrated SOFC/GT systems, as discussed in [36].

In the turbine maps [25], it is conventional to use the non-dimensional mass flow parameter ϕ_t, corrected turbine speed N_{tc}, expansion ratio ER, that are defined as:

$$\phi_t = \frac{W_t \sqrt{T_{t1}}}{p_{t1}}, \qquad N_{tc} = \frac{N}{\sqrt{T_{t1}}}, \qquad ER = \frac{p_{t1}}{p_{t2}}. \tag{2.28}$$

Analogous to the compressor, we introduce the normalized mass flow parameter, ϕ_{norm}, and the normalized speed parameter, $\widetilde{N}_{tc}$, for the turbine:

$$\phi_{norm} = \frac{\phi_t}{\phi_{choke}}, \qquad \widetilde{N}_{tc} = \frac{N_{tc}}{N_{tc}^{design}} = \frac{N}{N_t^{design}} \cdot \sqrt{\frac{T_{t1}^{design}}{T_{t1}}}, \tag{2.29}$$

where ϕ_{choke} is the corrected flow capacity where turbine choking occurs, N_t^{design} and T_{t1}^{design} are the turbine speed and turbine inlet temperature at the design point.

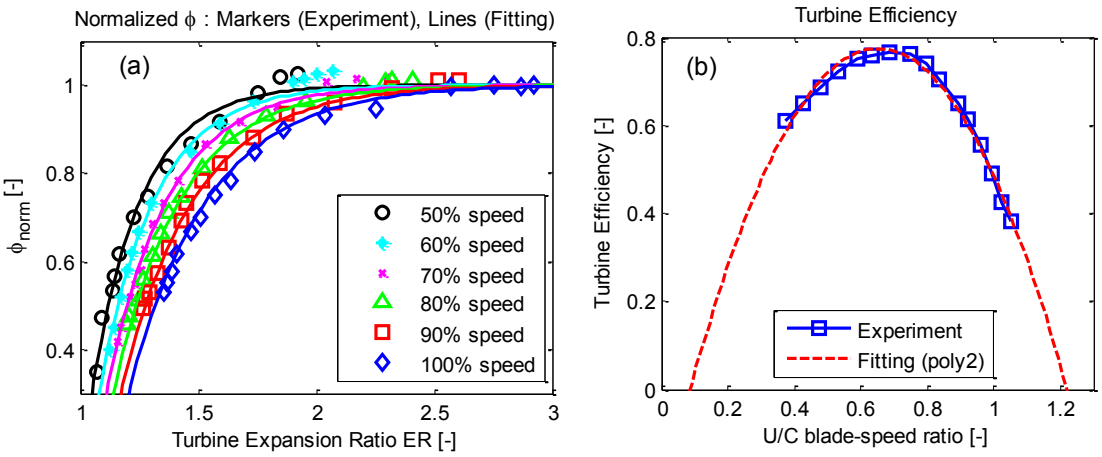

Figure 2.9: Turbine mass flow and efficiency maps: experimental and fitting results.

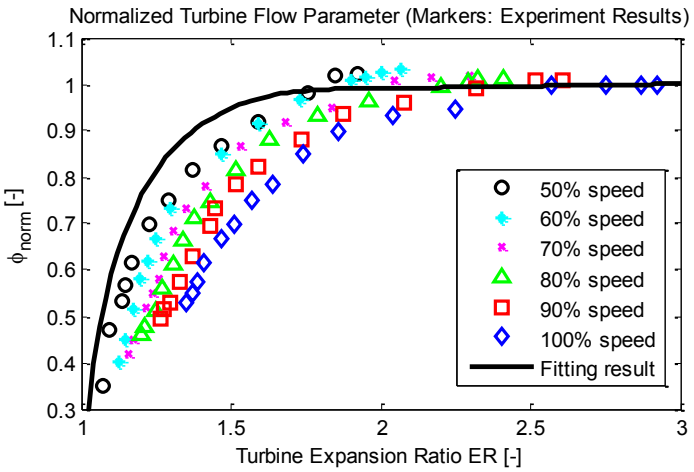

Figure 2.10: Fitting results of the turbine mass-flow map by formulas given in [28].

The relation between the turbine flow parameter, shaft speed and expansion ratio can be represented in the form of turbine map. Figure 2.9 presents the map of a typical radial turbine for diesel engine turbo-chargers in [26], [27]. However, formulas based on typical nozzle flow equations [25] that are used in [28] do not give good fitting results, as shown in Figure 2.10. An alternative fitting method is proposed. The normalized turbine flow parameter ϕ_{norm} can be expressed as a function of the expansion ratio ER:

$$\phi_{norm} = 1 - \phi_b \cdot exp(-ER/\phi_c), \tag{2.30}$$

where the speed-dependent coefficients ϕ_b and ϕ_c are defined as:

$$\phi_b = \phi_{b0} \cdot \widetilde{N}_{tc}^{\phi_{b1}} + \phi_{b2}, \qquad \phi_c = \phi_{c0}\widetilde{N}_{tc} + \phi_{c1}, \tag{2.31}$$

where ϕ_{bi} $(i = 0, 1, 2)$ and ϕ_{ci} $(i = 0, 1)$ are constant coefficients.

As shown in Figure 2.9 (a), close agreement between the curve fitting results and the experiment data has been achieved by using Eqn. (2.30) and Eqn. (2.31). Finally, the isentropic turbine efficiency can often be expressed as a function of the blade-speed ratio [57], which can be expressed as:

$$U/C = \frac{\pi D N_{tc}}{60\sqrt{2c_p T_{t1}\left(1 - \left(\frac{p_{t2}}{p_{t1}}\right)^{\frac{\gamma_t - 1}{\gamma_t}}\right)}}, \tag{2.32}$$

where D denotes the turbine blade tip diameter. Figure 2.9 (b) shows the relation between the blade-speed ratio U/C and the turbine efficiency as well as the fitting results.

2.3 Modeling of the Counter-Flow Heat Exchanger

A counter-flow heat exchanger (HEX) [37], as shown in Figure 2.11, is used to pre-heat the air in the integrated SOFC/GT system and its modeling is described in this

section. The HEX takes the compressed air, with temperature T_{bi}, from the compressor and the exhaust gas, with temperature T_{ai}, out of the turbine as the inputs and changes the temperature, T_{bo}, of the pre-heated air (the inlet air supplied to the SOFC stack) and the temperature, T_{ao}, of exhaust gas (system outlet to the environment) as its outputs. When given the inlet temperatures T_{ai} and T_{bi}, the pre-heated SOFC inlet air temperature T_{bo} and the cooled exhaust gas temperature T_{ao}, can be determined as follows:

$$T_{ao} = T_{ai} - \eta_{HEX}(T_{ai} - T_{bi}), \qquad T_{bo} = T_{bi} + \frac{W_a c_{p,a}}{W_b c_{p,b}} \eta_{HEX}(T_{ai} - T_{bi}), \tag{2.33}$$

where W_j and c_{pj} $(j = a, b)$ are the flow rates and specific heat capacities of flows along channel a and channel b, respectively; η_{HEX} is the HEX's efficiency [37], which depends on the HEX size and material, as well as properties of hot/cold fluids [38].

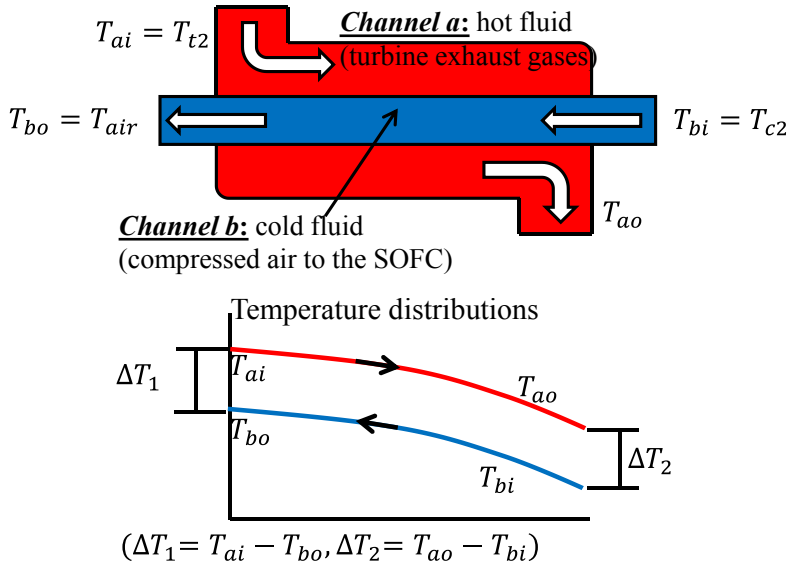

Figure 2.11: Temperature distributions along the counter-flow heat exchanger.

It should be noted that the HEX model expressed in Eqn. (2.33) is a quasi-static model [37], meaning that the output temperatures are steady-state values. However, the HEX cannot react instantaneously to changes in the inflow conditions. In order to account this fact, a first order time delay [60] can be added into Eqn. (2.33) to get the following

dynamic model for the counter-flow HEX as:

$$\begin{cases} \dfrac{dT_{ao}}{dt} = \dfrac{1}{\tau_{HEX}}[T_{ai} - \eta_{HEX}(T_{ai} - T_{bi}) - T_{ao}], \\ \dfrac{dT_{bo}}{dt} = \dfrac{1}{\tau_{HEX}}\left[T_{bi} + \dfrac{W_a c_{p,a}}{W_b c_{p,b}}\eta_{HEX}(T_{ai} - T_{bi}) - T_{bo}\right], \end{cases} \tag{2.34}$$

where τ_{HEX} is the time constant for the HEX.

Let ΔT_1 and ΔT_2 be defined as in Figure 2.11, the logarithmic mean temperature difference ΔT_{LM}, can be defined as:

$$\Delta T_{LM} = \frac{\Delta T_1 - \Delta T_2}{\ln(\Delta T_1/\Delta T_2)} = \frac{Q_{HEX}}{U_{HEX} \cdot A_{HEX}}, \tag{2.35}$$

where Q_{HEX} is the exchanged heat duty (in W), U_{HEX} is the HEX heat transfer coefficient (in $W \cdot K^{-1}m^{-2}$), and A_{HEX} is the exchange area. ΔT_{LM} is a very important parameter to determine the HEX size for the integrated SOFC/GT system [14]. For instance, a value of around 50 Kevin is often selected for ΔT_{LM} to keep the HEX size reasonable [14], [61].

2.4 Modeling of the Catalytic Burner

The catalytic burner (CB) is the device where the unused fuel from the SOFC fuel channel is burned with the remaining air from the SOFC cathode air channel to increase the gas flow temperature before it enters the downstream turbine. In many references [4], [14], a "magic" burner model is used by assuming complete reaction of all combustible gases (CH_4, CO, H_2) from the SOFC stack. For example, a static CB model is developed to calculate the CB's outlet temperature by using conservation of energy in [14]. There is no dynamic state in this model. This method has been used by many researchers.

By assuming adiabatic condition (i.e., no heat loss) and complete reaction of all combustibles, a dynamic CB model is derived in the following by using mass and energy conservation, as well as the ideal gas law.

The dynamics for the mass (m_{cb}) of gases inside the CB can be described as:

$$\frac{dm_{cb}}{dt} = W_{ca} + W_{an} - W_t, \tag{2.36}$$

where W_{ca} and W_{an} are the cathode and anode outlet mass flows, respectively; and W_t is the mass flow through the turbine.

By assuming uniform temperature distribution inside the burner, the temperature dynamics can be expressed using energy conservation:

$$\left(m_{bed}^{cb} c_{p,bed}^{cb} + \sum_k m_k^{cb}\, c_{p,k}^{cb} \right) \frac{dT_{cb}}{dt} = \sum_k N_{k,cb}^{In}\, h_{k,cb}^{In} - \sum_k N_{k,cb}^{Out}\, h_{k,cb}^{Out}, \tag{2.37}$$

$$k \in \{CH_4, CO_2, CO, H_2O, H_2, N_2, O_2\}$$

where $h_{k,cb}^{In}$, $h_{k,cb}^{Out}$ are the inlet and outlet enthalpies of the gas species k; $N_{k,cb}^{In}$, $N_{k,cb}^{Out}$ are the associated inlet and outlet molar flow rates; m_k^{cb} and $c_{p,k}^{cb}$ are mass and specific heat capacity of gas species k in CB, respectively; m_{bed}^{cb} and $c_{p,bed}^{cb}$ are properties of the CB bed reactor and thus are considered as constant [15].

The ideal gas law is used to calculate the pressure in the CB as:

$$p_{cb} = \frac{m_{cb} R T_{cb}}{V_{cb} M_{cb}} = \frac{\left(\sum_{k=1}^{n} m_k^{cb}\right) R T_{cb}}{V_{cb}\left(\sum_{k=1}^{n} M_k^{cb} N_k^{cb} \,/\, \sum_{k=1}^{n} N_k^{cb}\right)}, \tag{2.38}$$

where V_{cb} is the volume of the burner. Hence, there are two independent states, i.e., m_{cb} and T_{cb}, in the dynamic CB model expressed in Eqn. (2.36) - Eqn. (2.38).

It should be pointed out that there are many practical problems regarding the CB operation, especially those associated with mobile applications, need to be investigated. Discussions of these problems and operational safety issues, which are usually missing in the literature, will be presented in the following.

The catalytically-coated substrates, which are made of metal or ceramic materials, must be able to withstand the operating environment, particularly with respect to thermal

gradient and thermal shock [40]. This is important for fast load following operation of the SOFC/GT systems. Metallic substrates, which best fit this need, must be operated below 950℃ to ensure sufficient material strength. Ceramic substrates, which can be operated at higher temperatures, have thermal shock issues [40]. Note that both substrates should be operated above the light-off temperature (e.g., ~600 ℃) for catalytic combustion.

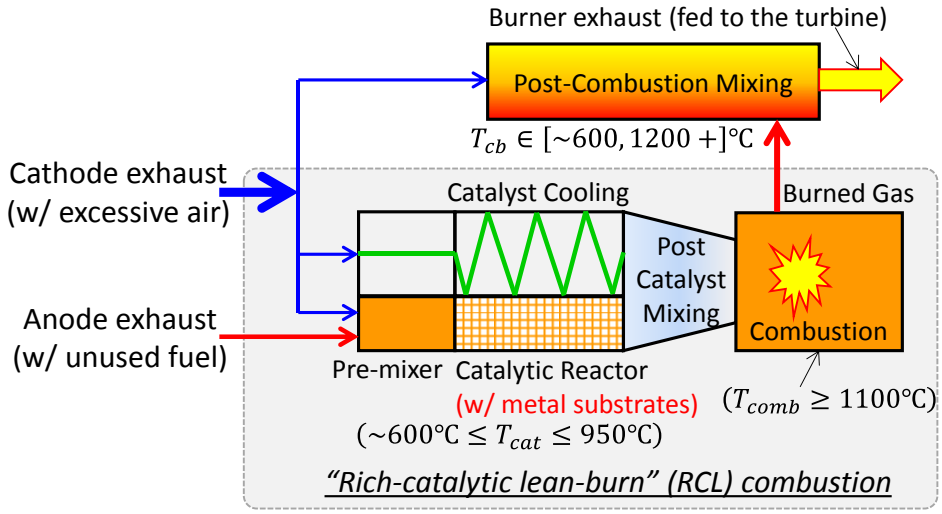

Figure 2.12: Schematic of the multi-stage burner based on RCL combustion [40].

Despite the temperature limitations, the metal substrates have been considered for GTs with high firing temperatures, using advanced design [40]. An example is the metal-based "rich-catalytic lean-burn" (RCL) combustion system in Figure 2.12. At high load conditions, total conversion of all combustible gases might destroy the metal substrates due to the high temperature. In this case, the RCL system [40], which combines fuel-rich operation of catalyst and fuel-lean gas-phase combustion, provides a practical solution.

As shown in Figure 2.12, all the SOFC anode exhaust and part of the cathode air exhaust enter the pre-mixer and then pass through the catalytic reactor where only a part of the anode exhaust is reacted in the catalyst stage. The oxidation of the fuel is limited by the available oxygen; therefore, it is referred to as fuel-rich operation. Part of the air can be used for catalyst cooling, thereby keeping the catalyst temperature in the desired range, e.g., 600 - 950℃. The fuel-rich effluent mixes with the catalyst cooling air prior to the fuel-lean gas-phase combustion, which requires a temperature ≥1100 ℃ for reaction.

If there is more exhaust air from the SOFC, the original RCL design cannot work because the CB temperature will be less than 1100 ℃, which is the minimum temperature required to sustain the gas-phase combustion. In this case, the original RCL design can be modified by appending a bypass valve. The potential new RCL design can be operated as follows: bypass part of the cathode air to the post-combustion mixing chamber and mix it with the burned gas from the fuel lean combustor, as shown in Figure 2.12. In doing so, the CB's outlet temperature could be able to meet the low/high temperature requirements for the SOFC/GT system, as will be shown in Section 4.4.

2.5 System Modeling

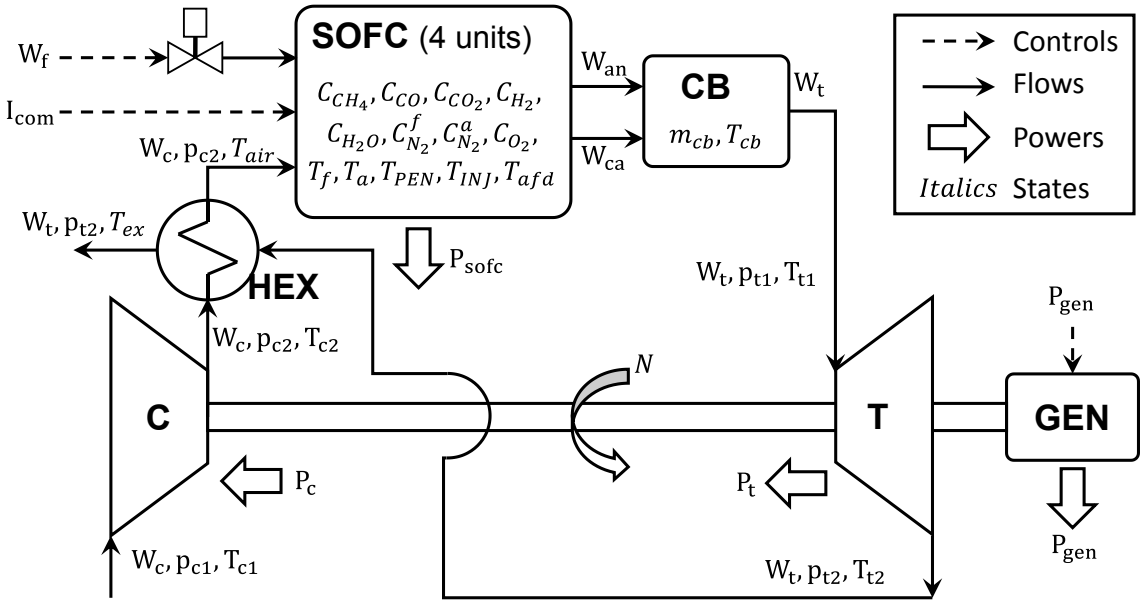

Figure 2.13: Integrated SOFC/GT model schematic including states, inputs and controls.

The overall model of the hybrid SOFC/GT system can be obtained by integrating all above component models. A schematic denoting the states, inputs, controls and main variables is presented in Figure 2.13. The interconnection of different components could also be identified in Figure 2.13. In order to integrate these component sub-models, the following conditions and assumptions are used [14], [15]:

1. The inlet pressure of the SOFC stack is equal to the compressor outlet pressure p_{c2}, by assuming zero pressure drop across the HEX.

2. The turbine inlet pressure p_{t1} and temperature T_{t1} equal to the CB's pressure p_{cb} and temperature T_{cb}, respectively.
3. The mass flow out of the CB, which equals the mass flow through the turbine, W_t, is dictated by the turbine maps, i.e., the turbine maps determine the mass flow W_t when given the turbine inlet pressure p_{t1} and turbine inlet temperature T_{t1}.
4. The air/fuel flows, i.e., W_{ca} and W_{an}, from the SOFC to the CB are determined by the difference between pressure of the last SOFC discretization unit and that of the CB.
5. The fuel flow supplied to the SOFC stack does not have any dynamics and is always equal to the commanded fuel flow input W_f.
6. The generator load P_{gen} is an input to the integrated system and is used to control the shaft speed N through shaft rotational dynamics shown in Eqn. (2.16). The dynamics (e.g., the generator voltage) of the generator/motor operation are not included.

The first three assumptions are commonly used in modeling of automotive turbo-chargers [63], [64] and the calculation error is negligible. Based on the fourth assumption, which is widely used in fluid dynamics, a linear orifice equation can be used to calculate the air/gas flows. The fifth assumption could potentially affect the system performance, though; most systems incorporate a fuel buffer, e.g., gas supply manifold, to achieve fast fuel changes. As shown in Figure 2.13, the integrated SOFC/GT system has three control inputs, namely, the fuel flow rate W_f, the current density I_{com} drawn from the SOFC and the generator/motor power P_{gen}.

The system model shown in Figure 2.13 lays foundation for the subsequent design and control studies. In CHAPTER 3, a 5kW-class R-SOFC/GT-based APU system will be studied. The specifications and GT maps are given in APPENDIX A. In CHAPTER 4 and CHAPTER 5, an S-SOFC/GT system that is intended to be used as a primary electric propulsion unit for military ground vehicles will be investigated. The GT maps shown in Section 2.2 will be used as baseline maps for the proposed S-SOFC/GT system. One can refer to Table 4.2 for more specifications of the S-SOFC/GT electric propulsion system and its recuperating counterpart, which is designed for comparison purposes.

CHAPTER 3
Generator/Motor Dual Mode Operation in Recuperating Systems

In this chapter, in order to extend the dynamic capabilities of R-SOFC/GT system for improved load following performance, the system is augmented by an energy storage unit (e.g., battery) and a dual operating generator/motor (G/M). In particular, this chapter focuses on studying the G/M dual mode operation and its implications on the transient performance and energy storage requirements. Active shaft load control can be achieved by using pre-conditioning of the G/M load for load step-up transitions and absorbing the over-produced power for load step-down transitions, as demonstrated in Section 3.2 and Section 3.3, respectively. Feedback and optimization algorithms have been proposed to implement the G/M dual mode operation. The effectiveness and computational efficiency of these algorithms are demonstrated by the simulation results. By taking full advantage of the dual mode operation of the electric machine (i.e., G/M), better trade-offs between load following and thermal safety can be achieved, power and energy requirements for the battery can be reduced, and overall system performance can be enhanced.

3.1 Introduction

The SOFC/GT system studied in this chapter is intended to be used as an APU for military ground vehicles [7]. The proposed APU, with a rated power around 5 kW, could provide sufficient power to support surveillance and other missions with reduced aural detectability during engine-off operations [6]. The specifications, including the GT maps and other parameters, are listed in APPENDIX A for this APU system. It should be noted that techniques discussed in this chapter can be applied to other size power systems.

As discussed in Section 1.3, the conventional R-SOFC/GT system has very poor dynamic capabilities and load following performance. In this chapter, to ease the power tracking operation and enhance transient capabilities, the SOFC/GT system is augmented

with new components and functionalities, as shown in Figure 3.1. First, an energy storage unit, e.g., a battery or capacitor pack is included to serve as the energy buffer during load transients. Second, the electric machine will be used as either a generator during normal operation or a motor (driven by the battery or the SOFC electrical output) when there is not enough turbine power for air delivery. Meanwhile, the motoring mode operation can also be used to entirely or partially absorb the excessive power during the load step-down transients, thereby reducing the battery power/energy requirements. This G/M dual mode operation, which is similar to the electrically assisted turbocharger used to improve the performance of automotive engines [67], [68], has not been studied for hybrid SOFC/GT systems in the literature, to the best of the author's knowledge.

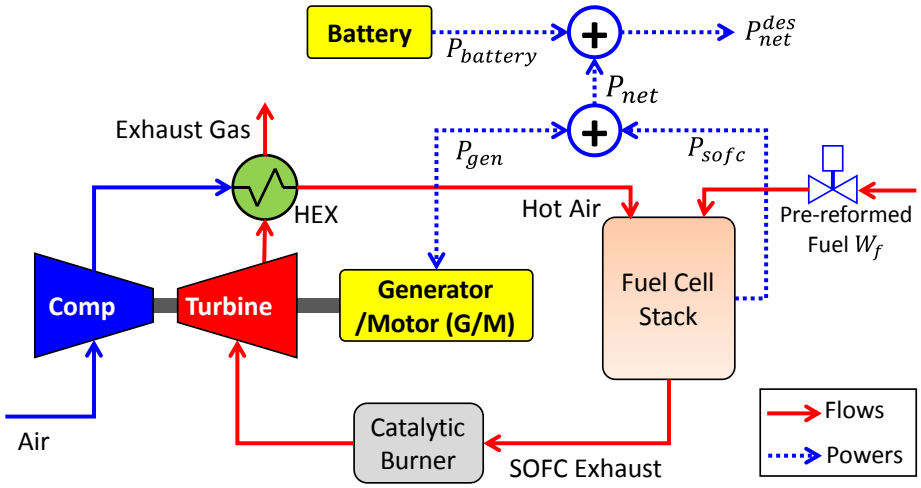

Figure 3.1: Schematic of the recuperating-SOFC/GT system augmented with G/M dual mode operation and energy storage (battery).

The focus of this chapter is to investigate the G/M dual mode operation and its implications on battery sizing and system operation. In particular, we will study whether the motoring operation can help in (1) eliminating system shutdown that is often caused by large/rapid shaft speed drop during load step-up transients; (2) improving transient responses; and (3) reducing the battery power and energy requirements.

Let P_{net} denote the net power of the system when the battery is not included. As shown in Figure 3.1, P_{net} is the sum of the SOFC power P_{sofc}, and the G/M power P_{gen}.

Meanwhile, we assume that the battery is used as an energy buffer to provide the deficit power or absorb the excessive power to meet the desired power demand P_{net}^{des} for perfect load following. Then, the battery power output $P_{battery}$ is equal to ΔP, which denotes the difference between P_{net}^{des} and P_{net} defined as:

$$\Delta P = P_{net}^{des} - P_{net} = P_{net}^{des} - \left(P_{sofc} + P_{gen}\right). \tag{3.1}$$

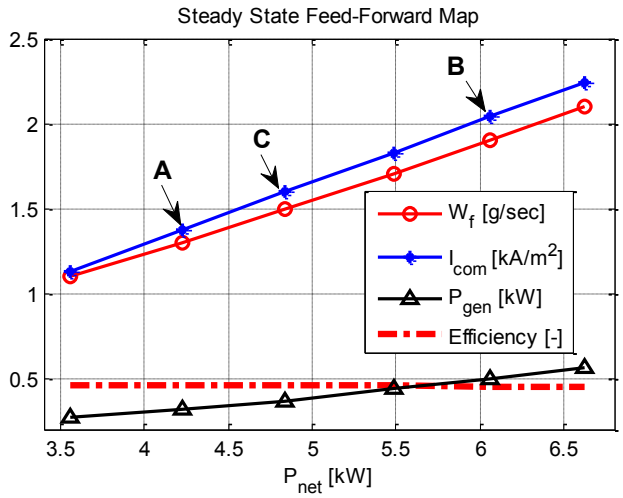

Figure 3.2: Steady-state optimal set-points for current density I_{com}, fuel flow rate W_f and generator power P_{gen} as a function of system net power P_{net}.

Without the battery, the SOFC/GT system has three control inputs, namely, fuel flow W_f, current density I_{com} and generator load P_{gen}. Figure 3.2 presents the static feed-forward map [15] of the optimal set-points (i.e., achieving maximum system efficiency) of these inputs with respect to the system net power P_{net}. As shown in Figure 3.2, around 45% overall efficiency can be achieved by the recuperating-SOFC/GT based APU system over a wide load range.

We will investigate the G/M dual mode operation for load step-up and step-down operations through case studies in Section 3.2 and Section 3.3, respectively. Note that the G/M transient is much faster than those of the SOFC and GT. Therefore, we assume that instantaneous control of the G/M load can be achieved in the following sections.

3.2 Step-Up Transient Operation

In this section, the G/M dual mode operation will be investigated through the load step-up transition from 4.20 kW to 6.06 kW (at time t_1 in Figure 3.3), which correspond to the optimal set-points A and B in Table 3.1, respectively.

Table 3.1 Feed-forward optimal set-points used for case studies in this chapter

Variables	$W_f\ [g \cdot sec^{-1}]$	$I_{com}\ [A \cdot m^{-2}]$	$P_{gen}\ [kW]$	$P_{net}\ [kW]$
Set-point A	1.3	1370	0.32	4.20
Set-point B	1.9	2040	0.50	6.06
Set-point C	1.5	1580	0.34	4.77

3.2.1 Analysis of the Load Step-Up Operation

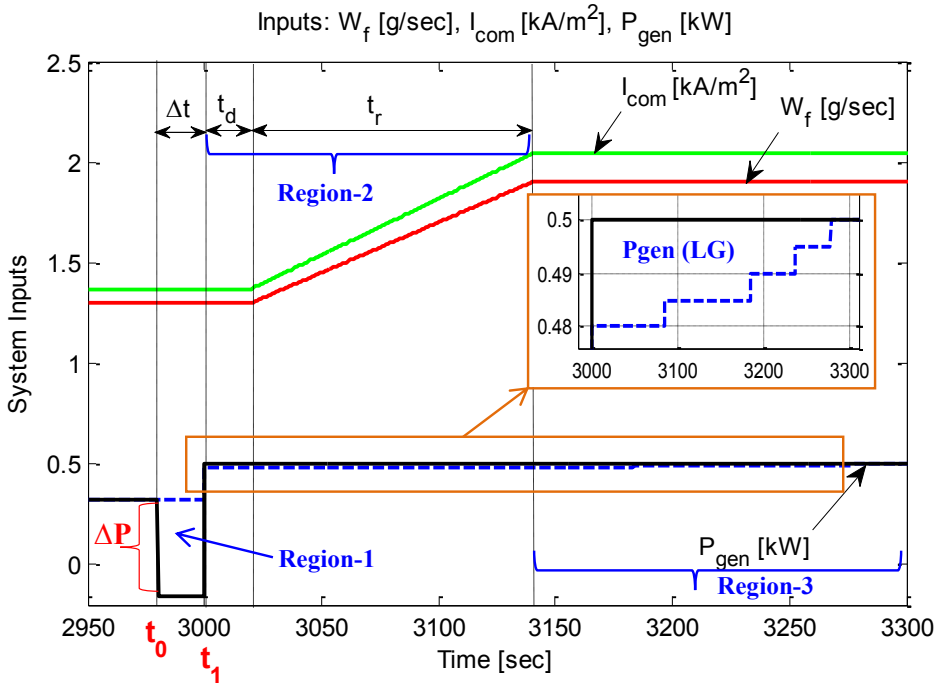

Figure 3.3: Illustration of the load step-up transition. The G/M dual mode operation is evaluated by combining the pre-conditioning (applied at region-1: $[t_0, t_1)$) of the generator load with the load governor (LG) applied after time t_1. Fuel path delay and dynamics are modeled in region-2, while the system settles down at the end of region-3.

Consider Figure 3.3, in ideal situations, the inputs to the SOFC/GT system can be stepped up instantaneously at time t_1 for fast load transition. However, it was shown that such operation can cause system shutdown due to sudden shaft speed drop [15]. To avoid system shutdown, the fuel flow rate W_f and current density I_{com} to the SOFC should be changed slowly for safe transient operation. Besides the fuel path dynamics, which can be represented by the fuel supply ramping time t_r, there is also some time delay t_d caused by the fuel supply and reforming system, as shown in Figure 3.3. This simplification is expected to be a reasonable representation of the complex fuel reforming/supply system, given the focus herein is to investigate the G/M dual mode operation [7]. In addition, to prevent possible hydrogen starvation and/or burner over-heating [15], the current density should be adjusted accordingly to match the fuel supply.

With W_f and I_{com} given in Figure 3.3, simulation indicates that the system could experience a shutdown if the generator load P_{gen} is stepped up from 0.32 kW to 0.50 kW, i.e., from $P_{gen}(A)$ to $P_{gen}(B)$ shown in Table 3.1, at time t_1. This is because increasing of P_{gen} deprives the turbocharger from having enough power for air delivery to support the SOFC operation during transients, causing the shaft to stall, as shown in Figure 3.4.

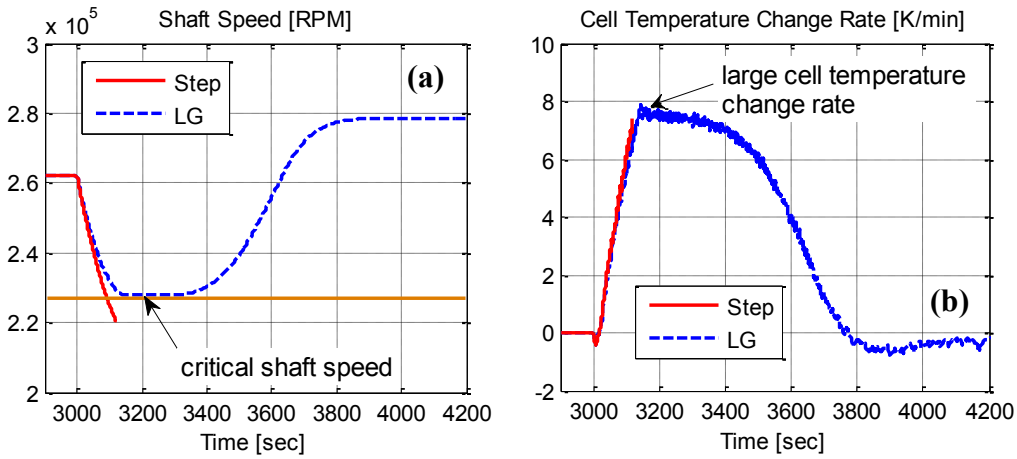

Figure 3.4: Load step-up transient responses (t_d=20sec, t_r=120sec). A direct step-up of P_{gen} from $P_{gen}(A)$ to $P_{gen}(B)$ at t_1 causes the shaft speed to drop below the critical speed, which eventually leads to system shutdown. A load governor (LG) can be used to manipulate P_{gen} for shutdown mitigation.

In order to achieve fast load following while avoiding possible system shutdown, one can identify the maximum permissible step change of P_{gen} at each time step [15] by solving the following optimization problem:

$$\min_{P_{gen}} \left(P_{gen}^{des} - P_{gen}\right), \tag{3.2}$$

$$\text{subject to: no system shutdown and } P_{gen}^{des} \geq P_{gen}, \tag{3.3}$$

where P_{gen}^{des} is the desired generator load.

The solution to Eqn. (3.2) and Eqn. (3.3) can be reformulated as a load governor (LG) problem [78] as follows:

$$\begin{aligned} P_{gen}(k+1) &= P_{gen}(k) + \max_{\lambda \in [0,1]} \lambda \left(P_{gen}^{des}(k) - P_{gen}(k)\right), \\ &\text{subject to: Eqn. (3.3) for } \forall k \text{ such that } k\Delta T \in [t_1, T], \end{aligned} \tag{3.4}$$

where λ is calculated for each time step by a one-dimensional (1-D) optimization search, ΔT is the sampling time, and T is the end of the simulation horizon. The LG results for P_{gen} and shaft speed N are given in Figure 3.3 and Figure 3.4, respectively. Note that for this moderate load step-up, since $P_{gen} > 0$ for all the time, motoring mode operation (i.e., $P_{gen} < 0$) is not required for shut-down mitigation. However, the LG results in Figure 3.3 and Figure 3.4 also reveals two issues: (1) large speed drop at the onset of load step-up, making the shaft speed close to the critical speed, N_{crt}, which corresponds to the lower boundary of the feasible operating region of the compressor; and (2) relatively large cell temperature change rate. Note that safer load transients can be achieved by imposing a more stringent shaft speed limit N_{min} ($N_{min} \geq N_{crt}$) in the LG design.

3.2.2 Leveraging G/M Dual Mode Operation: A Feasibility Study

Given that the rapid shaft speed drop, which is caused by the increase of P_{gen}, was shown to be the main cause of system shutdown, an intuitive solution is to increase the shaft speed by reducing P_{gen} or running the generator at the motoring mode (i.e., $P_{gen} < 0$)

to safely guide the system through transients. This operation, which is applied in region-1 in Figure 3.3, is referred to as the "pre-conditioning" of generator load in this dissertation. In particular, we would like to investigate the implication of pre-conditioning on transient performance and energy storage requirements. To this end, six different cases (Table 3.2), with different levels of G/M load for pre-conditioning, are implemented together with the LG to understand the effects of this particular strategy.

Table 3.2 Generator load during the pre-conditioning phase

Case	P_{gen} [W]	ΔP [W]	Note
#1	320	0	Baseline: LG, no pre-conditioning
#2	160	-160	Reduced P_{gen} for pre-conditioning + LG
#3	0	-320	Disengaging the generator for pre-conditioning +LG
#4	-160	-480	Motoring mode + LG
#5	-320	-640	Motoring mode + LG
#6	-480	-800	Motoring mode + LG

The same fuel flow rate and current density profiles are used for all these cases, as shown in Figure 3.3, where t_d = 20 sec, t_r = 120 sec and Δt = 20 sec. The generator load, P_{gen}, applied at the pre-conditioning phase keeps decreasing from case #1 to case #6, as shown in Table 3.2. For the baseline case (#1), no pre-conditioning operation is applied. The generator is disengaged (i.e., $P_{gen} = 0$) from the system in case #3. The generator is operated in the motoring mode (i.e., $P_{gen} < 0$) in the pre-conditioning phase for case #4, #5, and #6. The LG is used to determine the P_{gen} profile after pre-conditioning operation. The simulation results are presented in Table 3.3 and Figure 3.5.

From Figure 3.5, we see that better power tracking performance and smaller cell temperature variations have been achieved by the pre-conditioning strategy. Meanwhile, compared with the baseline case, i.e., case #1, the minimum shaft speed is kept relatively far away from the critical shaft speed for the last three cases, i.e., case #4 to case #6. This is mainly because of the fast shaft speed increase enabled by the motoring operation at the pre-conditioning phase, as shown in Figure 3.5.

The performance of different power transients is further analyzed in Table 3.3 in terms of three different metrics: (1) the power response and load following performance

measured by the settling time $T_s(P)$ and the RMS power tracking error ΔP_{RMS}; (2) the battery sizing requirements indicated by the battery's maximum discharging power P_{max} and the energy capacity E_{brg}; and (3) SOFC thermal stresses measured by the maximum cell temperature change rate T_{rate}^{max} and the temperature settling time $T_s(T_{cell})$.

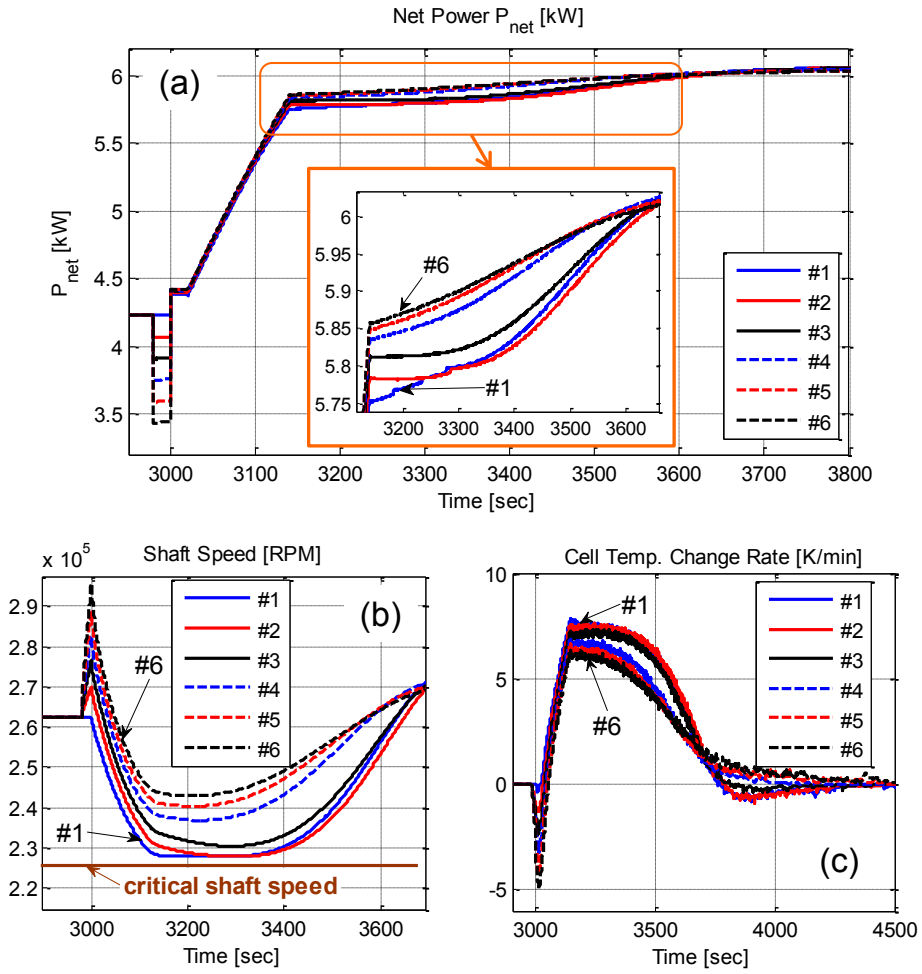

Figure 3.5: System performance in the load step-up transient: (a) net power response; (b) shaft speed; and (c) cell temperature change rate. By reducing P_{gen} in the pre-conditioning phase from case #1 to case #6, the minimum shaft speed keeps increasing while the maximum cell temperature change rate (absolute value) keeps decreasing.

As shown in Table 3.3, the proposed pre-conditioning operation of P_{gen} provides improvements to the system performance for most attributes:

- It shortened the power settling time $T_s(P)$ by up to 15% and reduced the RMS power tracking error ΔP_{RMS} by up to 6%.

- It lessened energy storage requirements by reducing the bridging energy capacity E_{brg} by up to 15%.
- It reduced the maximum cell temperature change rate (the absolute value) by up to 20%, thereby leading to safer thermal transient.

Table 3.3 Results of G/M dual mode operation for load step-up transients

Case	#1	#2	#3	#4	#5	#6
$T_s(P)$ $[sec]$	560 (100%)	576 (102.9%)	552 (98.6%)	488 (87.1%)	476 (85.0%)	476 (85.0%)
ΔP_{RMS} $[W]$	585.73 (100%)	601.77 (102.7%)	564.90 (96.4%)	551.26 (94.1%)	552.68 (94.4%)	556.90 (95.1%)
ΔP_{max} $[W]$	1681.29 (100%)	1655.14 (99.0%)	1647.93 (98.0%)	1636.47 (97.3%)	1633.79 (97.2%)	1631.38 (97.1%)
E_{brg} $[kJ]$	245.67 (100%)	242.00 (98.5%)	233.25 (94.9%)	210.32 (85.6%)	207.61 (84.5%)	207.95 (84.7%)
T_{rate}^{max} $[K \cdot min^{-1}]$	7.70 (100%)	7.60 (97.4%)	7.20 (93.5%)	6.70 (87.0%)	6.37 (82.7%)	6.00 (79.2%)
$T_s(T_{cell})$ $[sec]$	900 (100%)	940 (104.4%)	620 (68.9%)	710 (78.9%)	830 (92.2%)	1000 (111.1%)

It should be noted that further reduction in the generator load P_{gen} (i.e., increasing the motoring power) offered very limited or no further improvement of the overall system performance as shown in case #5 and case #6, compared with case #4. This is especially true for the power tracking performance and the energy storage requirements.

3.2.3 Pre-conditioning Strategy for Load Step-up Transients

The above case study provides evidence that the G/M dual mode operation has the benefit of improving operational safety and load following performance. In particular, we see that system shutdown can be avoided by pumping additional mechanical energy into the shaft through motoring operation. In order to achieve fast (i.e., minimizing the RMS power tracking error ΔP_{RMS}) and safe (i.e., keep limited cell temperature change rates and sufficient distance from the critical shaft speed N_{crt}) load following performance, we can formulate the following trajectory planning problem:

$$\min_{\{P_{gen}(k)\}} \sum_{k=1}^{N_{opt}} \left(P_{net}(k) - P_{net}^{des}(k)\right)^2,$$
$$subject\ to: \begin{cases} (1) no\ system\ shutdown, \\ (2) shaft\ speed\ N \geq N_{min}\ (N_{min} \geq N_{crt}), \\ (3) |dT_{cell}/dt| \leq T_{rate}^{UB}\ (safe\ thermal\ transient), \end{cases} \quad (3.5)$$

where N_{opt} is the number of optimization variables, and T_{rate}^{UB} is the limit of the SOFC cell temperature change rate for safety considerations.

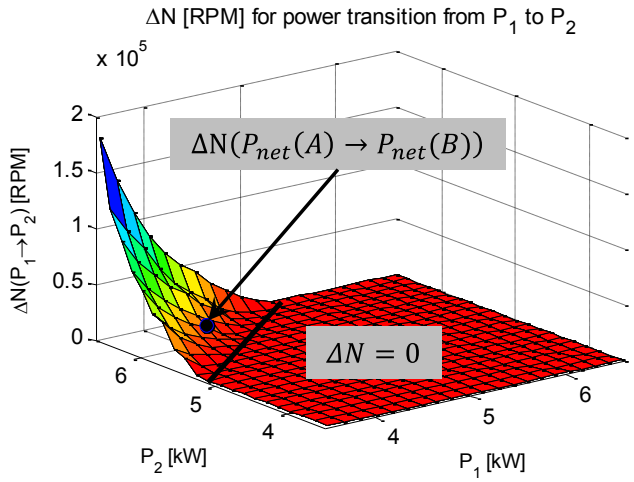

Figure 3.6: The look-up table (LUT) for $\Delta N(P_1 \rightarrow P_2)$. The solid line is the upper boundary for the region of $\Delta N = 0$, i.e., no pre-conditioning of P_{gen} is required for a safe step-up transition for the regions in the lower-right direction of this curve.

However, the trajectory planning problem formulated in Eqn. (3.5) is difficult to solve due to its large dimension and complex system dynamics, thereby making online implementation impossible. The optimization dimension of (3.5) is equal to N_{opt}, where $N_{opt} > 100$ in our case study. An alternative approach can be proposed as follows: First, through an off-line simulation process, we determine the minimum shaft speed increase, ΔN, that is required to sustain the system operation before the actual load increase can be applied. This is equivalent to determining the required additional energy that should be pumped into the shaft by the motoring operation or reducing P_{gen} in the pre-conditioning phase. Once ΔN is determined, the pre-conditioning strategy is formulated by solving the 1-D optimization problem defined in Eqn. (3.6) and (3.7). This 1-D optimization problem

determines the maximum permissible P_{gen} for each sampling time of the pre-conditioning phase. Second, once the desired shaft speed, N_{des}, is achieved by the pre-conditioning, the controller is switched to the LG to increase P_{gen} for fast load following.

The off-line process for ΔN is explained as follows. Using the SOFC/GT system model, N_{des} can be determined by a 1-D search algorithm for different power transitions. Given an initial (P_1) and final (P_2) power level, the incremental shaft speed $\Delta N(P_1 \rightarrow P_2)$ is the speed increase required for a safe transition, and this becomes the control objective for pre-conditioning. The results are given in Figure 3.6, where $\Delta N = 0$ implies that pre-conditioning is not required. If $\Delta N > 0$, the pre-conditioning control will be activated to identify the optimal G/M power to achieve the desired shaft speed. The results shown in Figure 3.6 are stored as a look-up table (LUT) for online implementation.

In order to achieve the desired pre-transition shaft speed N_{des}, the G/M load P_{gen} during the pre-conditioning phase can be determined as follows. At each sampling time $t \in [t_0, t_1)$, i.e., the pre-conditioning phase, consider:

$$P_{gen}(\tau) = P'_{gen} \text{ for } \tau \in [t, t_1), \tag{3.6}$$

where P'_{gen} is determined by solving:

$$\begin{aligned} &\max P'_{gen}, \\ &subject\ to: N(t_1) \geq N_{des}, \end{aligned} \tag{3.7}$$

where $N_{des} = N(P_1) + \Delta N$ with $N(P_1)$ being the steady-state shaft speed corresponding to power P_1 and ΔN given in Figure 3.6. Note that since $dN/dP_{gen} < 0$, the optimization problem in Eqn. (3.7) is well-posed and has a unique solution. The solution to Eqn. (3.7) can be found by using 1-D optimization search such as the bisectional algorithm starting from the search region $[P_{fsb}, P_{infsb}]$ for each time $t \in [t_0, t_1)$, where P_{fsb} and P_{infsb} are a feasible and an infeasible input respectively for the pre-conditioning operation. In order to reduce the computational cost of online implementation, the procedure in Figure 3.7 can be used to reduce the size of the initial search region.

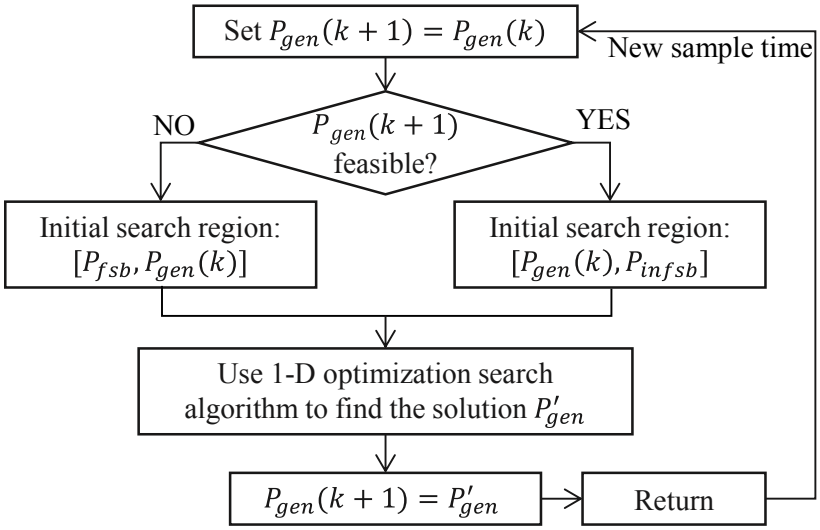

Figure 3.7: Flowchart to identify the G/M load for the pre-conditioning phase.

As shown in Figure 3.6, the incremental shaft speed, ΔN, that is required for the load step-up transition from $P_{net}(A)$ to $P_{net}(B)$ with W_f and I_{com} given in Figure 3.3, is 12853 rpm. Note that N_{min} equals N_{crt} in the design. With $P_{fsb} = -320W$ and $P_{infsb} = 320W$, the G/M load required for the pre-conditioning phase, which can be determined by using the algorithm presented in Figure 3.7, is $P_{gen}(t) = 30W$ for $t \in [t_0, t_1)$. When there is a disturbance in the system, $P_{gen}(t)$ determined by the algorithm in Figure 3.7 will vary with time, as the state, which may be different from the predicted value, will be fed back at each time instant in the 1-D optimization procedure.

3.3 Step-Down Transient Operation

In this section, we investigate the G/M dual mode operation for downward load transition through an example of load step decrease from 6.06 kW to 4.77 kW, which correspond to the optimal set-points B and C in Table 3.1, respectively.

3.3.1 Analysis of Load Step-down Operation

Transient issues associated with downward load transition are quite different from those in upward transition. While system shutdown is not an issue here, the slow transient

and large power tracking error are the main concerns. In this section, we will analyze the dynamic characteristics of step-down operation through case studies, where five different operating strategies summarized in Table 3.4 are applied.

As discussed previously, slow ramping inputs for W_f and I_{com} should be applied to the SOFC for safe operation. If P_{gen} is ramped down accordingly (baseline: case #1), there will be a considerable power tracking error caused by power over-production, as shown in Figure 3.8. Intuitively, the over-produced power can be absorbed by the battery for fast load following. It could also be entirely or partially absorbed by operating the generator at motoring mode, thereby reducing the charging current for the battery. In the sequel, we will investigate the G/M dual mode operation and its implications for load step-down transient operation and battery requirements.

Table 3.4 G/M dual mode operation during load step-down transients

Case	Control of the generator load P_{gen}
#1	Baseline case: directly ramp down P_{gen} from $P_{gen}(B)$ to $P_{gen}(C)$
#2	Pre-scheduled P_{gen} control for fast load following
#3	Direct P_{gen} compensator for fast power tracking
#4 & #5	Feedback control for coordinated power and thermal management

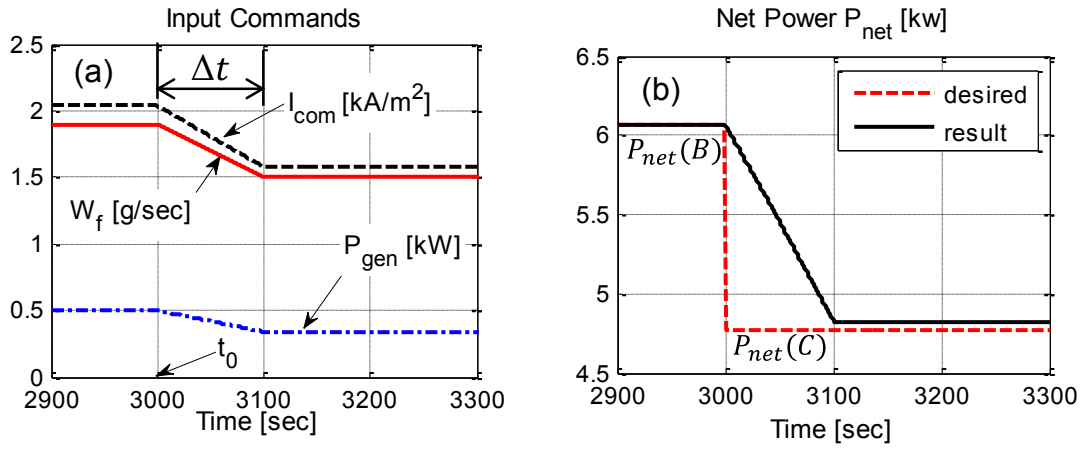

Figure 3.8: The system inputs and the net power response for the baseline case during load step-down operation.

3.3.2 Fast Load Following By G/M Dual Mode Operation

Analogous to Eqn. (3.5) for load step-up transitions, a trajectory planning problem can be formulated for fast load following (i.e., minimizing power tracking error ΔP_{RMS}) for load step-down transitions as:

$$\min_{\{P_{gen}(k)\}} \sum_{k=1}^{N_{opt}} \left(P_{net}(k) - P_{net}^{des}(k)\right)^2, \quad subject\ to: |dT_{cell}/dt| \le T_{rate}^{up}\ (safe\ thermal\ transient). \tag{3.8}$$

Similar to Eqn. (3.5), the trajectory planning problem formulated in Eqn. (3.8) is difficult to solve due to of its large dimension. Therefore, alternative solutions should be developed. Because of the large thermal inertia, the SOFC's electric power output P_{sofc} is dominated by the W_f and I_{com} inputs during transients. Therefore, we can predict P_{sofc} by using the SOFC/GT model and pre-schedule the G/M load to compensate for the slow SOFC power transients. For W_f and I_{com} inputs shown in Figure 3.8, the pre-scheduled P_{gen} control, which corresponds to case #2 in Table 3.4, can be expressed as:

$$P_{gen}(t) = \begin{cases} -800 + 10.40(t - t_0) & (t_0 \le t < t_0 + \Delta t), \\ 240 + 0.5(t - t_0 - \Delta t) & (t_0 + \Delta t \le t < t_0 + 300), \\ 340 = P_{gen}^{SS}(C) & (t_0 + 300 \le \mathrm{t}). \end{cases} \tag{3.9}$$

An alternative method for fast load following is to use P_{gen} to directly compensate the SOFC power P_{sofc}, which can be determined according to the measured voltage and current of the SOFC stack. Therefore, a direct P_{gen} compensator by using:

$$P_{gen}(t) = P_{net}^{des}(t) - P_{sofc}(t)\ for\ t > t_0, \tag{3.10}$$

has also been investigated in case #3, as shown in Table 3.4.

As shown in Figure 3.9 (a) and (b), both the pre-scheduled P_{gen} control (case #2) in Eqn. (3.9) and the direct P_{gen} compensator (case #3) in Eqn. (3.10) achieved extremely good power tracking performance through G/M dual mode operation. However, this is

achieved by risking the thermal transient safety. For operation safety considerations, the cell temperature should be changed slowly, e.g., Siemens-Westinghouse tubular SOFCs often require a 4-6 hour start-up time [1], which corresponds to a temperature change rate of around 4 $K \cdot min^{-1}$. Note that this strict requirement can be smoothed by using the micro-tubular SOFCs [65], [66], which have a high thermal shock resistance.

As shown in Figure 3.9 (c) and (d), rapid drop of the cell temperature, which is represented by the mean PEN temperature in Figure 3.9 (c), and large cell temperature change rate can be observed for case #2 and case #3 in Figure 3.9 (d). The reason is that fast reduction of P_{gen} or even motoring operation accelerates the shaft rapidly, as shown in Figure 3.9 (e). Consequently, more air is delivered to cool the SOFC rapidly, as shown in Figure 3.9 (f) and Figure 3.9 (c). Hence, it can be concluded that fast load following and safe thermal transients are two competing objectives, due to the strong correlation of the cell temperature change rate, the air flow rate, and the shaft speed.

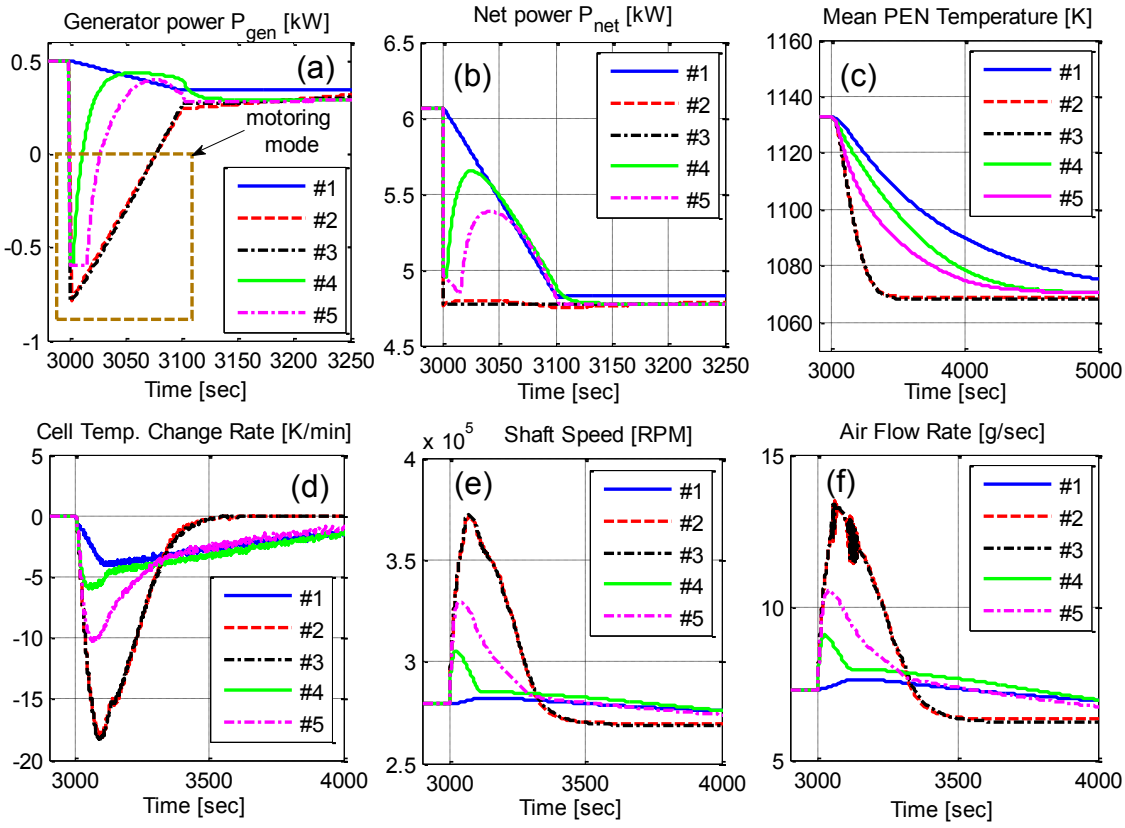

Figure 3.9: Transient response during load step-down transients.

3.3.3 Balancing Power Tracking and Thermal Management

To balance fast load following and safe thermal transient, which are competing against each other, a feedback control scheme, which can be expressed as:

$$P_{gen} = \left[P_{net}^{des} - P_{sofc}\right] + [k \cdot (N - N_0) \cdot 1(N \geq N_0)],$$
$$\text{where } 1(N \geq N_0) = \begin{cases} 1 & (N \geq N_0), \\ 0 & otherwise, \end{cases} \tag{3.11}$$

is proposed for the coordinated power and thermal management in case #4 and case #5. The first term of Eqn. (3.11), which is identical to the direct P_{gen} compensator expressed in Eqn. (3.10), is used for fast power tracking. A proportional controller, i.e., the second term of Eqn. (3.11), is included to limit the shaft speed and airflow, thereby limiting the cell temperature change rate within a reasonable range, as shown in Figure 3.9 (d). This feedback controller is developed based on the strong correlation between the shaft speed and cell temperature change rate, as shown in Figure 3.9. The controller in Eqn. (3.11) has two design parameters: the proportional gain k and the threshold N_0, the latter is used to activate the thermal management through the indicator function $1(N \geq N_0)$.

Table 3.5 Results of G/M dual mode operation for load step-down transients

Case	#1	#2	#3	#4	#5
$T_s(P)$ $[sec]$	~100 (100%)	~0 (~0.0%)	0 (0.0%)	~100 (100%)	~100 (100%)
ΔP_{RMS} $[W]$	773.6 (100%)	17.2 (2.2%)	0.0 (0.0%)	622.9 (80.5%)	432.4 (55.9%)
ΔP_{max} $[W]$	1288.0 (100%)	25.3 (2.0%)	0.0 (0.0%)	878.0 (68.2%)	610.0 (47.4%)
E_{brg} $[kJ]$	68.6 (100%)	1.1 (1.6%)	0.0 (0.0%)	57.6 (84.0%)	39.0 (56.9%)
T_{rate}^{max} $[K \cdot min^{-1}]$	4.0 (100%)	**18.1** (453%)	**18.1** (453%)	5.8 (145%)	10.0 (250%)
$T_s(T_{cell})$ $[sec]$	2468 (100%)	350 (14.2%)	350 (14.2%)	1450 (58.8%)	1153 (46.7%)

Detailed results for the load step-down transition are given in Table 3.5. Almost instantaneous load following can be achieved by the pre-scheduled P_{gen} control in case #2 and the direct P_{gen} compensator in case #3. However, they induce unacceptably large cell temperature change rates. The proposed coordinated power and thermal management, has moderate load following performance (case #4 and case #5), as expected. Moreover, the cell temperature change rates are limited to a proper range for safe SOFC operation. Therefore, the proposed coordinated power and thermal control, as shown in Eqn. (3.11), can manage the trade-offs between cell temperature and power transients effectively. In addition, compared with the baseline case (i.e., case #1), reduced battery requirements, i.e., reduced battery charging power ΔP_{max} and energy capacity E_{brg}, have been achieved through active control of P_{gen} in all the other cases.

3.4 Evaluation of the Proposed Control Strategies

As shown in Figure 3.10, the proposed control strategies are evaluated through a typical load transition profile, in which the pre-conditioning strategy proposed in Section 3.2.3, is applied during load step-up transition while the coordinated power and thermal control expressed in Eqn. (3.11) is used for load step-down transition. Compared with the baseline case, in which the load governor in Eqn. (3.4) and the direct P_{gen} compensator in Eqn. (3.10) are used for load step-up and step-down transitions, respectively, improved load following performance has been achieved during load step-up transition. Meanwhile, the cell temperature change rate is limited in a reasonable range during load transitions, thereby ensuring thermal transient safety.

It should be noted that the control strategy expressed in Eqn. (3.11) produces non-monotonic power response for load step-up transition, as highlighted in Figure 3.10 (a). Similar results have also been observed for case #4 and case #5 in Figure 3.9 (b). This is mainly due to the indicator function, $1(N \geq N_0)$, used in Eqn. (3.11). Once the load step-down is applied, the controller (3.11) will work as the direct P_{gen}compensator in (3.10) since N is less than N_0, as shown in Figure 3.9 (e). Consequently, the actual P_{net} tracks the net power demand perfectly, leading to rapid increase of shaft speed. Once N exceeds the threshold N_0, the thermal management function will be activated to increase P_{gen} and

P_{net}, as shown in Figure 3.9 (a) and (b). In addition, as shown in Figure 3.9 (b), P_{net} starts to decrease in case #4 and #5 about 40 seconds after the load step-down is applied. This is mainly due to the reduced SOFC power caused by the downward-ramping I_{com} input. In the future, alternative control strategies such as model predictive control will be developed to improve the overall performance for load step-down transients.

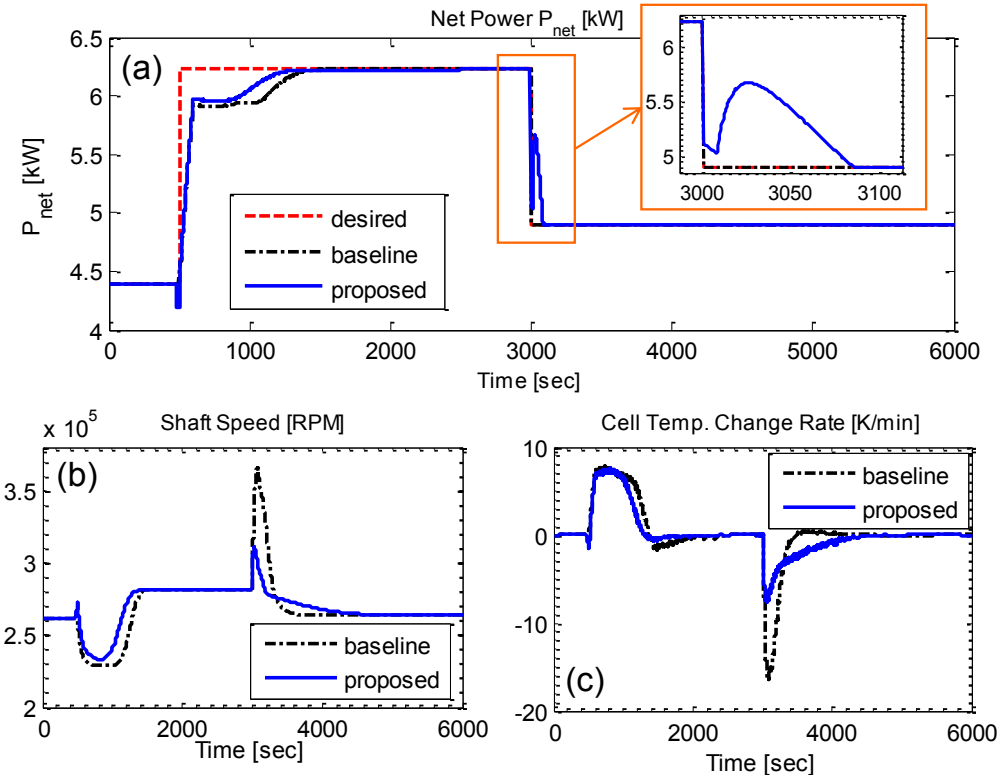

Figure 3.10: Transient performance of the baseline case and the proposed control strategies. A load step-up transition from 4.39kW to 6.23kW is applied at 500 seconds and a load step-down transition from 6.23kW to 4.90 kW is applied at 3000 seconds.

CHAPTER 4
System Design and Steady-State Performance Evaluation of Sprinter SOFC/GT Systems

4.1 Introduction

Many strategies have been developed to improve the load following performance of SOFC/GT systems. However, one common problem of the conventional R-SOFC/GT systems is that their transient performance is limited by the slow dynamics of the SOFC since the SOFC provides about 80% of the system net power. To solve this problem, an S-SOFC/GT system concept is proposed, as explained in Section 1.3.3. In this system, a "down-sized" SOFC stack that is operated at constant temperature provides the constant baseline power while the GT-generator is used for dynamic load following. Compared to the R-SOFC/GT system, the GT-generator, i.e., the component with fast dynamics, has significantly enhanced power generation capability in the S-SOFC/GT system. Therefore, the proposed S-SOFC/GT system is expected to achieve: (1) fast load following by taking full advantage of the GT-generator's fast dynamic capability; (2) efficient and long life-cycle operation by running the SOFC at fairly constant temperature [39].

Although the R-SOFC/GT and the S-SOFC/GT systems have the same layout and base components, as shown in Figure 1.2, they do have differences in (1) the relative size between the GT-generator and the SOFC; and (2) operation principles. Table 4.1 presents detailed comparisons of these two systems. The S-SOFC/GT system has a larger relative size ratio of the GT-generator with respect to the SOFC than its recuperating counterpart since more power is produced by the GT-generator in the sprinter system. Substantial variations of cell temperature, which occur in the R-SOFC/GT system, might damage or seriously degrade the SOFC due to thermal stresses [14]. This problem can be avoided by operating the SOFC at constant temperature in the S-SOFC/GT system.

Table 4.1 Recuperating-SOFC/GT system versus sprinter-SOFC/GT system.

Systems	R-SOFC/GT System	S-SOFC/GT System
SOFC	- Provides ~80% of the net power - Fairly constant FU (e.g., FU equals about 85%) during operation - Varying SOFC power/temperature over the entire load range	- "Down-sized" to provide the constant baseline power - Substantial FU variations (e.g., 50% - 90%) over the load range - Constant SOFC temperature
GT-generator	- Energy recuperation (GT), auxiliary device (generator) - Poor power generation capability mainly due to its limited size - $P_{gen}/P_{sofc} \approx 25\%$, i.e., relatively constant power split ratio	- Important power generation device (to provide the transient power for dynamic load following) - Significantly enhanced power generation capability - P_{gen}/P_{sofc} varies over 20% - 90%
Load following operation	- Both the SOFC and GT-generator are used for load following - Limited by the SOFC's slow dynamic capability - Fast dynamics of GT-generator cannot be used due to its size and power generation capability	- SOFC is not used for dynamic load following; it only provides the constant baseline power - Fast load following by using GT-generator's fast dynamic capability - Long life-cycle operation by keeping constant SOFC temperature

The S-SOFC/GT system investigated in this dissertation is to be used as a primary electric propulsion system for military ground vehicles. It should be able to: (1) provide constant baseline power P_{base} when working in the recuperation mode; (2) meet a much higher power requirement, e.g., the peak power P_{peak}, for tactic/battle-field maneuvers by running the GT-generator in the boosting mode [39]. In order to compare the concept and the operation, an R-SOFC/GT system and an S-SOFC/GT system are developed to cover the same power range over 100-170 kW. When combined with energy storage, e.g., battery, both systems could be used for military vehicles such as the hybrid HUMVEE and mid-sized trucks [72]. Note that while results reported in this chapter are specific for this particular targeted power, the proposed design procedure and analysis methodology are more general, and can be applied to other size power systems.

The remainder of this chapter is organized as follows: an operational strategy to keep fairly constant SOFC power/temperature over the entire load range is presented in Section 4.2 while a design procedure for the sprinter system is elucidated in Section 4.3. The feasible operation regime and steady-state performance are studied in Section 4.4. In particular, the "actual" operation envelope is determined by applying the constant SOFC

power and temperature constraints over the "safe operation regime". In Section 4.5, the steady-state optimization problem to achieve maximum fuel efficiency is investigated.

4.2 Strategy to Maintain Constant SOFC Power and Temperature

Like the R-SOFC/GT system, the S-SOFC/GT system also has three inputs: fuel flow W_f, current density I_{com}, and the generator load P_{gen} [39]. In addition to the W_f and I_{com} inputs, there are some other parameters, e.g., the SOFC inlet airflow rate W_{air} and temperature T_{air}, which will affect the SOFC performance. Note that the SOFC block has four inputs: W_f, I_{com}, W_{air} and T_{air}. The inlet airflow W_{air} can be controlled by P_{gen} [14] while T_{air} is the HEX cold flow channel outlet temperature (Figure 2.11), which depends on the fuel flow W_f, airflow W_{air}, compressor/turbine outlet temperatures T_{c2} and T_{t2}, as well as the HEX parameters (e.g., size and material related coefficients).

In the proposed S-SOFC/GT system, a substantial variation of the turbine power is required to meet the varying power demands over the entire load range because P_{sofc} remains fairly constant at all conditions. In this case, large variations of turbine flow W_t (note: $W_t = W_f + W_{air}$) and turbine inlet/outlet temperatures (which affects T_{air} by the HEX) are expected. All these variations are expected to have significant influence on the SOFC performance given the closed couplings of system components [7]. Hence, it is necessary to perform sensitivity analysis and find effective strategies to coordinate these inputs to keep fairly constant SOFC power and temperature over the entire load range. To this end, an SOFC stack consisting of 960 tubular cells presented in Section 2.1 will be used in the following analysis. The SOFC stack achieves a nominal power around 88 kW when operated at 1040K. A slightly up-scaled (scaled by a factor of 1.091) compressor [30] (see Figure 2.7 and Figure 2.8 for the original maps) and the radial turbine shown in Figure 2.9 are selected in the following case study. In addition, the HEX is sized to keep the SOFC inlet temperature T_{air} within a safe range.

To keep fairly constant SOFC power P_{sofc}, the current density I_{com} is expected to be relatively constant, i.e., with a very limited variation range, over the entire load range. With a fixed I_{com} input, the main degrees of freedom for operating the system are fuel

flow W_f and airflow W_{air} (controlled by P_{gen}). Figure 4.1 shows the SOFC performance for fixed I_{com} (I_{com}=1950 $A \cdot m^{-2}$) and varying W_{air} and W_f inputs. Note that P_{sofc} and U_{sofc} (voltage) have very similar distributions over the W_{air}~W_f plane. This is expected for fixed I_{com} input because $P_{sofc} = U_{sofc} I_{com} A_{sofc}$ where A_{sofc} represents the surface area where the electro-chemical reaction takes place. In addition, when we reduce the air-flow W_{air} while keeping fuel flow W_f fixed, T_{sofc}, P_{sofc} and U_{sofc} all increase due to the reduced cooling effect, as shown in Figure 4.1. Moreover, constant SOFC temperature is achieved, e.g., T_{sofc}=1040K, along the solid lines in Figure 4.1.

Along the constant T_{sofc} line, key operating variables, including P_{sofc}, U_{sofc}, and T_{air}, are plotted in Figure 4.2. As shown in Figure 4.2 (c), when more air (W_{air} increases with respect to W_f) is delivered to the SOFC, T_{air} should be elevated to counteract the cooling effect, thereby keeping constant T_{sofc}. Also, the cell voltage U_{sofc} increases with respect to W_f due to the increased open-circuit voltage U_{OCV}, as shown in Figure 4.2 (b). This can be derived from the Nernst equation in Eqn. (2.2). Consequently, P_{sofc} increases with respect to W_f when both T_{sofc} and I_{com} are fixed, as shown in Figure 4.2 (a). Hence, to keep constant P_{sofc} and T_{sofc} over the entire load range, I_{com} should be a decreasing function of W_f. In addition, T_{grad}, as shown in Figure 4.2 (d), reduces with respect to W_f because the increased airflow helps to smooth the SOFC temperature distributions.

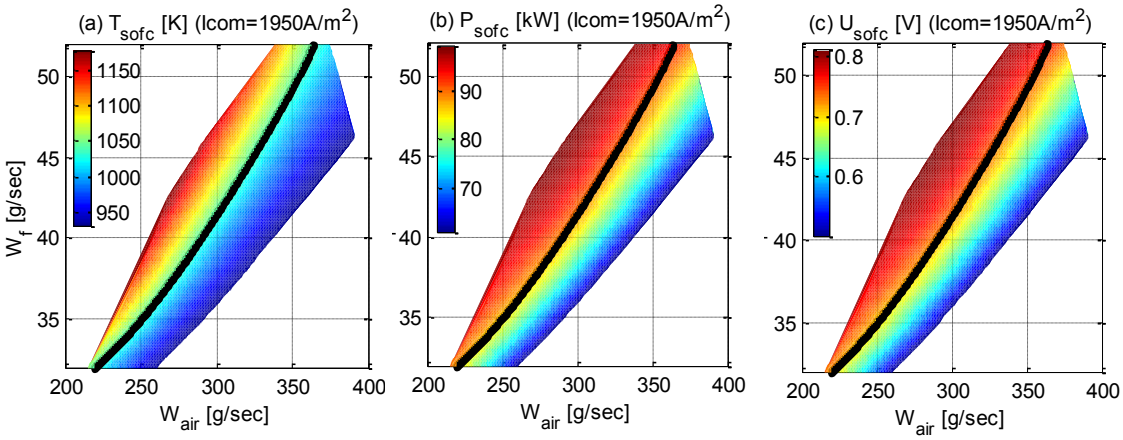

Figure 4.1: SOFC performance with fixed current input ($I_{com} = 1950A \cdot m^{-2}$). The SOFC temperature is constant at 1040K along the solid lines in the figure.

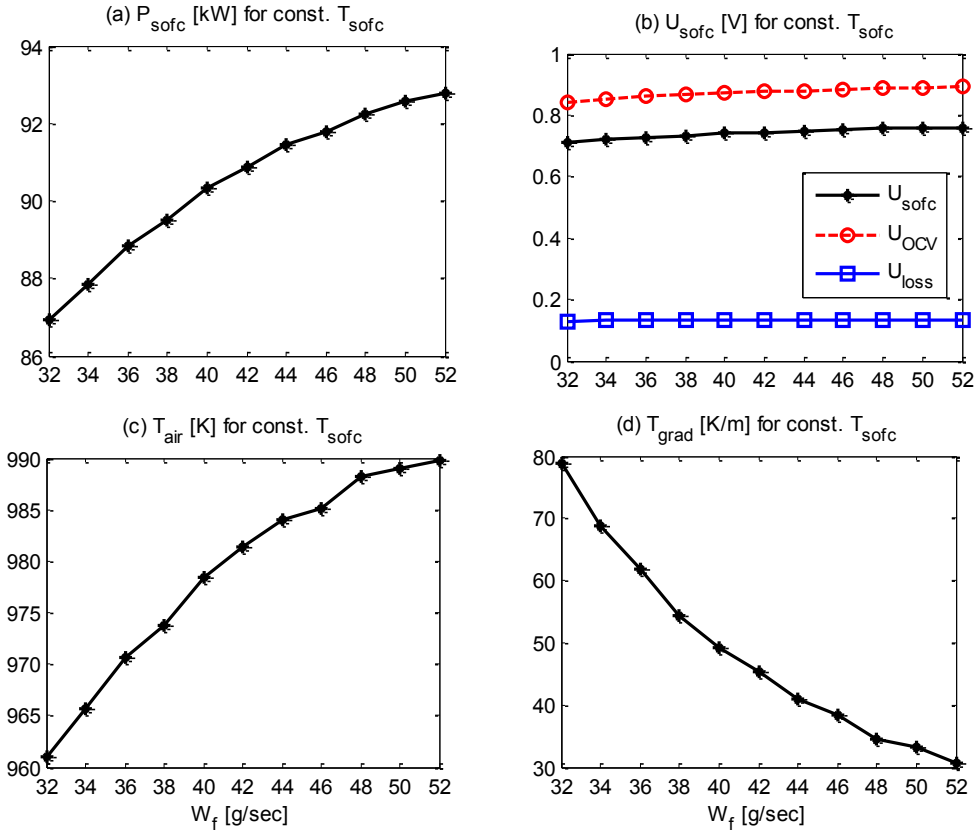

Figure 4.2: Operating variables for constant T_{sofc} operation: (a) SOFC power P_{sofc}; (b) cell voltage; (c) SOFC inlet air temperature T_{air}; and (d) temperature gradient T_{grad}.

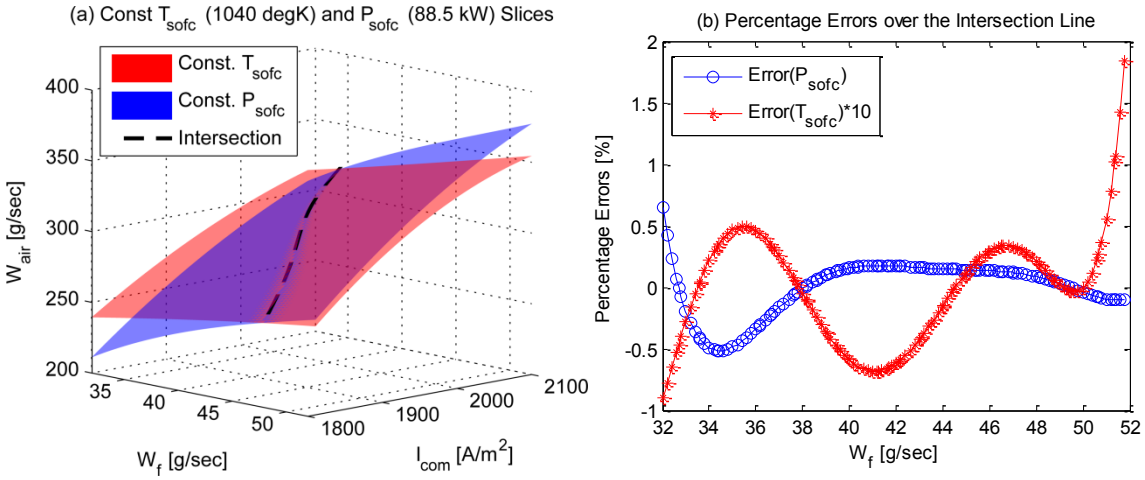

Figure 4.3: Fairly constant SOFC power and temperature have been achieved over the intersection line of the constant T_{sofc} isosurface and the constant P_{sofc} isosurface. Figure (b) shows the percentage errors for P_{sofc} and T_{sofc} along the intersection line.

To keep P_{sofc} and T_{sofc} fairly constant over the whole load range, we will study the relations among system inputs when allowing I_{com} to vary. Figure 4.3 (a) shows the isosurface for a constant P_{sofc} of 88.5 kW, the isosurface for a constant T_{sofc} of 1040K, and the intersection line of these two isosurfaces. In theory, both P_{sofc} and T_{sofc} will be exactly constant along the intersection line. However, small variations are observed, as shown in Figure 4.3 (b), mainly due to the numerical errors in calculating the isosurfaces. Nevertheless, fairly constant P_{sofc} and T_{sofc} can be achieved along the intersection line. In particular, less than 1.0% and 0.2% percentage errors are achieved for P_{sofc} and T_{sofc}, respectively, as shown in Figure 4.3 (b). Figure 4.4 shows relations of the SOFC inputs along the intersection line. These relations can be approximated as follows:

$$W_{air} = f_{Wair}(W_f) = k_{Wair2}(W_f)^2 + k_{Wair1}W_f + k_{Wair0}, \tag{4.1}$$

$$T_{air} = f_{Tair}(W_{air}) = k_{Tair2}(W_{air})^2 + k_{Tair1}W_{air} + k_{Tair0}, \tag{4.2}$$

$$I_{com} = f_{Icom}(W_f) = k_{Icom1}W_f + k_{Icom0}. \tag{4.3}$$

It should be noted that although these results are generated by using specific GT maps and HEX parameters for this specific case study, the relations in Figure 4.4 to keep constant SOFC power and temperature are very strong and are expected to hold (at least, the relations hold at a qualitative level) for various component (e.g., the SOFC and GT) parameters. This has been verified in our simulation studies.

Based on the above analysis, an effective SOFC operating strategy, which can be used to coordinate the SOFC inputs (i.e., W_f, I_{com}, W_{air} and T_{air}) to keep fairly constant T_{sofc} and P_{sofc} over the entire load range, is proposed as follows:

- First, determine the air-fuel ratio: analogous to power sources such as the internal combustion engines (ICEs), a linear relation between the airflow W_{air} and fuel flow W_f is expected for the S-SOFC/GT system. However, it is observed that a quadratic relationship for W_{air} and W_f, as defined in Eqn. (4.1), which is quite close to linear, as shown in Figure 4.4 (a), gives better results in our case study.
- Second, determine the inlet air flow and temperature relation: to keep fairly constant

T_{sofc}, the inlet air temperature T_{air} needs to be increased to counteract the cooling effect when more air is delivered to the SOFC, as shown in Figure 4.4 (b). To this end, a quadratic relation between W_{air} and T_{air}, as expressed in Eqn. (4.2), is used to keep constant T_{sofc} and P_{sofc} over the entire load range.

- Third, find a relation between the current density and fuel flow: both W_{air} and T_{air} can be expressed as functions of W_f by using Eqn. (4.1) and Eqn. (4.2). In this case, there are two independent input variables left for the SOFC block, i.e., W_f and I_{com}. As shown in Figure 4.4 (c), an appropriate relationship between these two variables, which can be used to limit the variations of T_{sofc} and P_{sofc} over the entire load range, can be determined through model-based steady-state simulations.

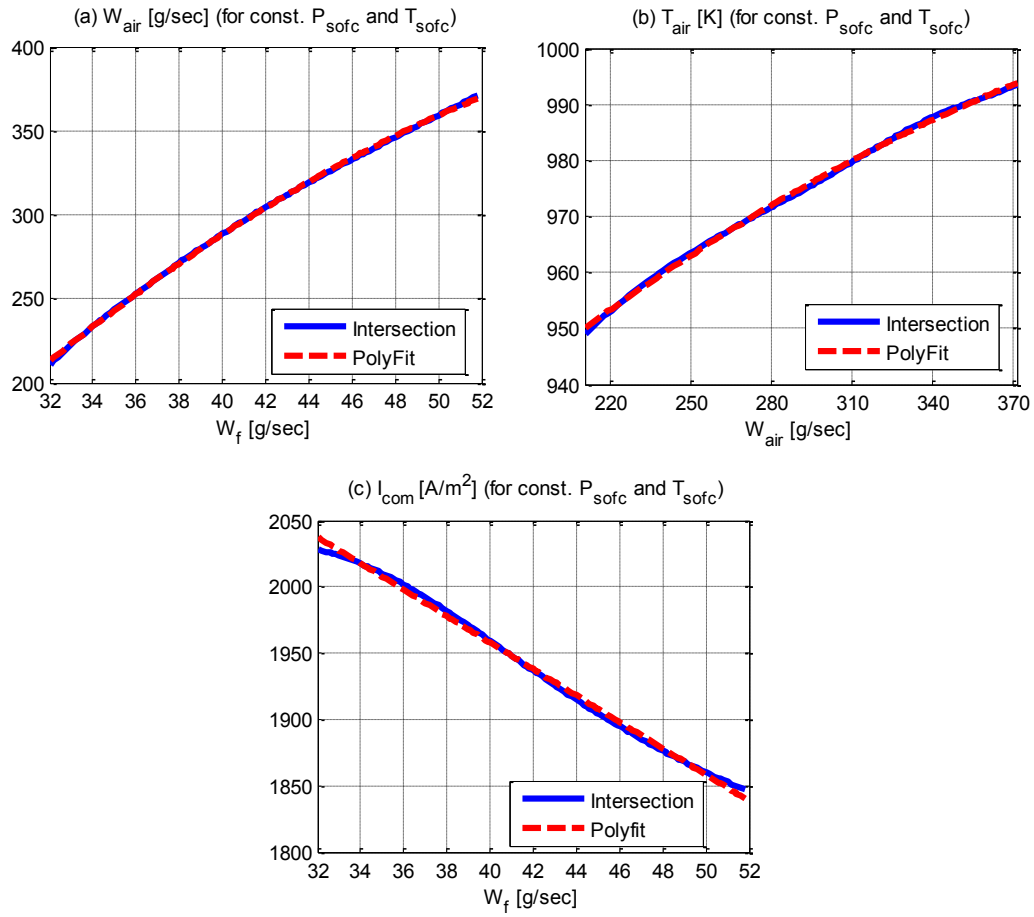

Figure 4.4: Strategies to maintain fairly constant SOFC power and temperature: (a) air flow W_{air}; (b) SOFC inlet air temerpature T_{air}; and (c) current density I_{com}.

4.3 A Design Procedure for the Sprinter Systems

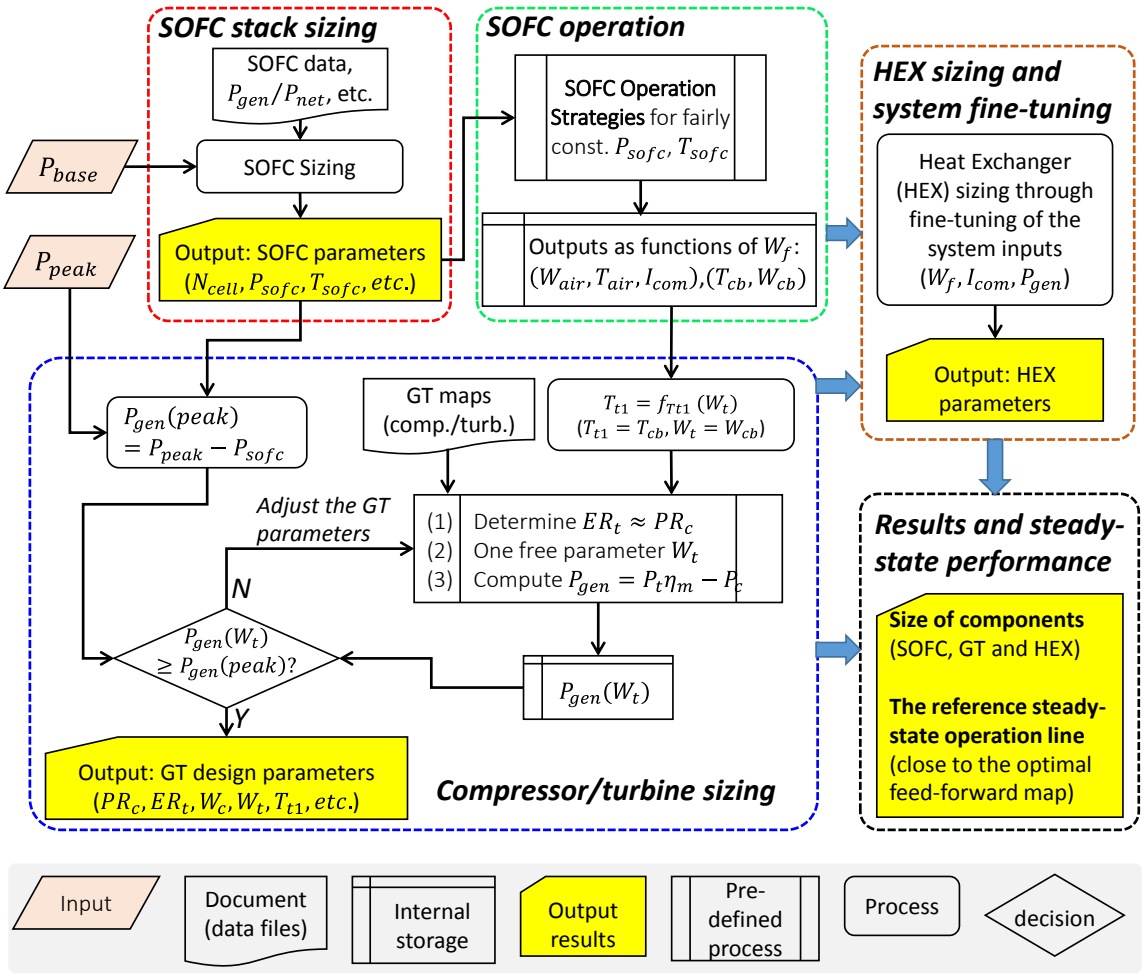

Figure 4.5: A design procedure for the proposed S-SOFC/GT systems.

As shown in Figure 4.5, a design procedure, which helps to determine the sizes of different components (e.g., SOFC and GT) and the reference steady-state operation line, is formulated for the proposed S-SOFC/GT system as follows:

- **Step-I: determine the SOFC stack parameters.** Based on the cell performance data and empirical parameters (e.g., the power split ratio P_{gen}/P_{net}), the SOFC parameters (e.g., cell number N_{cell}, P_{sofc}, and T_{sofc}) can be determined according to the baseline power requirement. For the target system, 960 tubular cells whose specifications are given in Section 2.1 are selected to produce an SOFC power of 88.5kW with a mean cell temperature around 1040K.

- **Step-II: determine the GT parameters.** To this end, the SOFC operational strategy developed in Section 4.2, in which the SOFC block inputs W_{air}, T_{air} and I_{com} can be expressed as functions of W_f, is used to keep fairly constant P_{sofc} and T_{sofc} over the entire load range. Consequently, a relation between the CB temperature T_{cb} and the turbine mass flow W_t, which equals the CB mass flow W_{cb}, can be determined from the simulation results of the SOFC and CB blocks. We can pick the initial values for the compressor pressure ratio and turbine expansion ratio from available GT maps. Then, there is one unknown variable W_t left, which can be determined by matching the associated power $P_{gen}(W_t)$ with $P_{gen}(peak)$ to meet the peak power requirement. In this chapter, a slightly up-scaled (scaled by a factor of 1.091) Garrett compressor (see Figure 2.7 and Figure 2.8 for the original compressor maps) [30] and the radial turbine shown in Figure 2.9 are selected for the target system.
- **Step-III: determine the HEX parameters.** It should be pointed out that in the basic system setup where no active control of T_{air} is available, small variations of the HEX coefficients are required for different loads to keep constant T_{sofc} and P_{sofc} over the entire load range [39]. In this case, we can select the mean value of calculated HEX coefficients and tune the system inputs, e.g., fine-tuning P_{gen} and/or I_{com} for a given fuel flow (W_f) input, to get the desired results. In this study, the HEX is sized to have a logarithmic mean temperature difference ($LMTD$) value of $\Delta T_{LM} \approx 120K$, thereby keeping the SOFC inlet air temperature T_{air} within an appropriate range.

Table 4.2 lists key parameter values by applying the proposed design procedure in Figure 4.5 for the target system. The proposed design procedure also helps to determine the reference steady-state operation line [39], which is expected to be close to the optimal feed-forward map (refer to Figure 5.1 for its location in the compressor map). In addition, to compare the proposed S-SOFC/GT system with respect to its recuperating counterpart, an R-SOFC/GT system has also been designed, as shown in Table 4.2.

A total number of 1320 and 960 tubular cells (see Section 2.1) are selected for the R-SOFC/GT system and the S-SOFC/GT system, respectively. The S-SOFC/GT system has reduced variation ranges for T_{sofc}, $P_{sofc}$and I_{com} than the R-SOFC/GT system. Note

that the S-SOFC/GT system has a larger FU variation range because more fuel is reacted in the CB, e.g., more about 50% of the fuel is burned in the CB in the sprinter system.

Moreover, in order to take full advantage of the GT's fast dynamics, a larger GT-generator with significantly enhanced power generation capability is selected for the S-SOFC/GT system. In particular, the Garrett GTX2867R compressor [30] and the radial turbine from [26], [27] are used for the R-SOFC/GT system while up-scaled ones (scaled by the similarity principle in [25]) are used for the S-SOFC/GT system. Furthermore, low inertia GT-generator set should be used in order to achieve fast load following operation. For example, the low-inertia high-speed motor in [85] is used in this dissertation and the effective shaft inertia of the GT-generator is calculated based on the data in [85], [86].

Analogous to [14], the HEX is sized to have an $LMTD$ value of $\Delta T_{LM} \approx 60K$ for the recuperating system. For the S-SOFC/GT system, a smaller HEX with $\Delta T_{LM} \approx 120K$ is selected in order to recuperate less portion of thermal energy from the turbine exhaust, thereby keeping the SOFC inlet temperature T_{air} within a safe range.

Table 4.2 Key parameters for the recuperating and sprinter SOFC/GT systems

Components	Parameters	R-SOFC/GT	S-SOFC/GT
SOFC Stack	Cell number N_{cell} [-]	1320	960
	SOFC temperature T_{sofc} [K]	800 - 1150	960 - 1080
	SOFC power P_{sofc} [kW]	40 - 150	70 - 96
	Current density I_{com} $[A \cdot m^{-2}]$	700 - 2300	1800 - 2100
	Fuel utilization FU [-]	75% - 90%	50% - 90%
GT-Generator (@ design point)	Compressor pressure ratio PR [-]	~3.50	~3.50
	Compressor flow W_c $[g \cdot sec^{-1}]$	320	360
	Turbine inlet temperature [K]	1273K (1000℃)	1273K (1000℃)
	Turbine expansion ratio ER [-]	~3.50	~3.50
	Corrected turbine swallowing capacity ϕ_{choke} $[kg \cdot K^{0.5} \cdot sec^{-1} \cdot bar^{-1}]$	3.922	4.246
	Designed shaft speed [RPM]	1.500e5	1.436e5
	Effective shaft inertia J $[kg \cdot m^2]$	1.0e-3	1.2e-3
HEX	$LMTD$ value ΔT_{LM} [K]	~60	~120
Integrated System	Net power range (SS-line) [kW]	78.9 - 187.9	103.8 - 171.2
	Net power efficiency (SS-line) [-]	55.5% - 56.1%	46.8% - 50.2%

4.4 Steady-State Operation Envelope and Performance

In Section 4.4.2, we identify the "safe operation regime" by applying constraints pertinent to different operational safety issues and investigate the system performance within the valid operating regimes for the S-SOFC/GT system. In Section 4.4.3, the effect of the maximum permissible CB temperature will be investigated. The "actual" operation envelope that is determined by taking into account the additional constraints of keeping constant SOFC power and constant SOFC temperature will be studied in Section 4.4.4. In order to provide a baseline for comparison purposes, the corresponding results for the R-SOFC/GT system (see Table 4.2) are summarized in APPENDIX B.

4.4.1 System Operational and Safety Issues

In the SOFC/GT system, improper choices of operational variables might cause degradation, reduced life time and even system breakdown. In this section, we investigate some critical safety issues, e.g., SOFC cracking, component overheating, thermal fatigue and compressor surge, and discuss their causes and consequences. The safety factors will be used to determine the feasible operation envelope of the S-SOFC/GT system.

4.4.1.1 SOFC (cell cracking, overheating, and thermal fatigue)

Due to the differences in thermal expansion coefficients of different layers (see Figure 2.1), mechanical stresses will be developed when the cell temperature is different from the zero stress temperature [14], i.e., the temperature at which different layers are adjoined. When exposed to high stresses, the brittle ceramic materials used for the SOFC are likely to crack, thereby degrading the cell performance by creating contact resistances and leakage current. Note that the zero stress temperature (e.g., 1400K) is usually higher than the SOFC operation temperature. This implies that the thermally induced stress and probability of cell cracking will increase for low temperatures. Another cause for the cell cracking is the temperature gradient. Hence, the minimum local cell temperature and the maximum temperature gradient are monitored for issues related to cell cracking.

Note that the cell temperature changing rate will also affect the thermal stresses, which might lead to material fatigue fractures and thus degrade the SOFC. The mean cell temperature is the major indicator and will be used to evaluate cell performance related to

thermal fatigue [14]. In the S-SOFC/GT system, fairly constant cell temperature helps to minimize the thermal fatigue, thereby leading to long life-time operation. In addition, the maximum local cell temperature should be kept within a safe range because overheating of the SOFC may cause irreversible changes in the electrode structure. It should be noted that air starvation and hydrogen depletion should be avoided since they may also damage or degrade the SOFC. For example, the hydrogen molar fraction is kept above 1% during operation in [4] to avoid fuel starvation.

4.4.1.2 GT (compressor surge, turbine overheating, and speed constraints)

The compressor surge will occur if the pressure ratio the compressor has to work against is too high for its current speed. During surging, a noisy and violent flow process can occur causing periods of backflow through the compressor, which might damage the system. A safe distance from the operating point to the surge line should be maintained to avoid compressor surge. Another safety issue is the turbine overheating because too high temperature will lead to material failure which will eventually cause system breakdown [14]. Hence, the turbine inlet temperature should be maintained in a safe range. For safety and efficiency considerations, the GT speed should be constrained within an appropriate range, outside which the GT's efficiency will decrease significantly. The maximum GT speed is bounded by constraints such as the bearing/sealing system limitations [25].

4.4.1.3 Burner (temperature constraints)

Practical problems related the CB operations are discussed in Section 2.4. For the S-SOFC/GT system, the multi-stage high-temperature CB system with metallic substrates (see Figure 2.12) should be used, as will be explained in Section 4.4.3. The burner should not be operated at too high temperature to avoid CB over-heating. Note that the metallic substrates should be operated above the catalyst light-off temperature (e.g., ~600 ℃) to enable catalytic combustion [40]. Therefore, both the minimum and the maximum burner temperatures will be monitored in this chapter.

4.4.1.4 HEX (overheating, thermal shock)

Overheating and thermal shock can attack the HEX, causing reduced life time or even system breakdown. The metallic HEX, which has good performance in the thermal gradient/shock aspects, should be operated below 950℃ to avoid material failure. Similar

to the SOFC and ceramic CB, the ceramic HEX can be operated at higher temperatures, but thermal shock issues have not been resolved. Hence, in this chapter, metallic HEX is selected for both SOFC/GT systems due to its advantages in thermal gradient and shock performance and costs. The inlet temperature of the HEX's hot channel (see Figure 2.11), which equals the turbine outlet temperature, will be monitored for safety considerations.

Table 4.3 Key safety parameters related to the feasible operation regimes

Constraint	Parameters	Operational and safety issues
#C1	Mean value of cell temperature T_{sofc}	SOFC thermal fatigue, system efficiency
#C1a	Max local cell temperature T_{sofc}^{max}	SOFC overheating
#C1b	Min local cell temperature T_{sofc}^{min}	SOFC thermal stress and cell cracking
#C1c	Max cell temperature gradient T_{grad}^{max}	SOFC thermal stress and cell cracking
#C2	SOFC cell voltage U_{sofc}	Very low efficiency for $U_{sofc} \leq 0.45V$
#C3	Gas turbine shaft speed N	GT efficiency, mechanical (e.g., bearing and sealing systems) limitations
#C4	Turbine outlet temperature T_{t2} (note: T_{t2} equals $T_{HEX}(hot\ inlet)$)	HEX overheating, especially for metallic materials
#C5	Burner temperature T_{cb} (note: T_{cb} equals turbine inlet temperature T_{t1})	High T_{cb} leads to CB/turbine overheating; Low T_{cb} reduces catalyst activity

Table 4.4 Constraint values for the SOFC/GT systems

Constraint	Parameters	R-SOFC/GT	S-SOFC/GT
#C1	Cell temperature UB T_{sofc}^{UB} [K]	1400	1400
	Cell temperature LB T_{sofc}^{LB} [K]	800	800
#C2	Cell voltage LB U_{sofc}^{LB} [V]	0.45	0.50
#C3	Shaft speed UB N^{UB} [RPM]	1.567e5	1.500e5
	Shaft speed LB N^{LB} [RPM]	0.600e5	0.600e5
#C4	HEX temperature UB T_{HEX}^{UB} [K]	1223 (950℃)	1223 (950℃)
#C5	CB temperature UB T_{cb}^{UB} [K]	1500 or 1223	1500 or others
	CB temperature LB T_{cb}^{LB} [K]	900	900
	Note: UB and LB denote upper bound and lower bound, respectively.		

Table 4.3 summarizes the operational safety parameters that are used to determine the feasible operation regimes for the SOFC/GT systems. Table 4.4 shows the constraint values that are used to identify the "safe operation regimes" for the R-SOFC/GT system and the S-SOFC/GT system, whose specifications are summarized in Table 4.2. Note that the superscripts UB and LB refer to upper bound and lower bound, respectively.

4.4.2 Operational Region Determined by Safety Issues

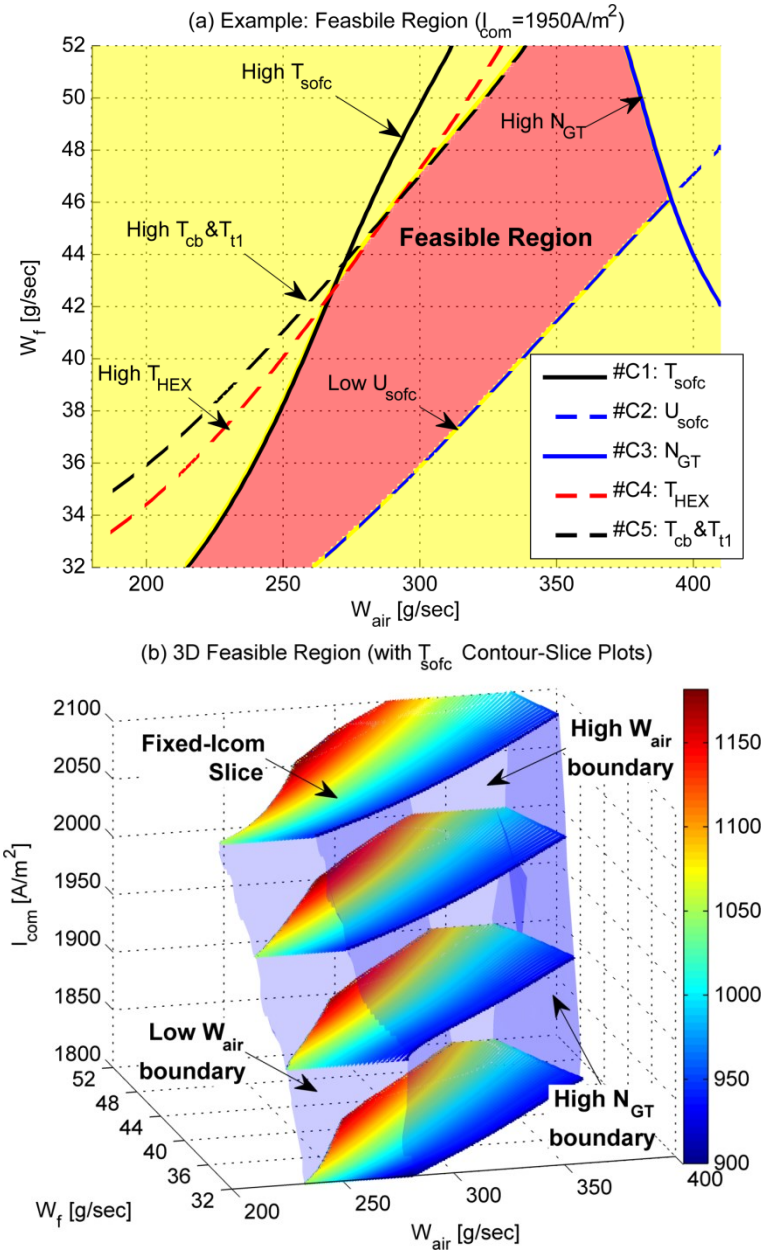

Figure 4.6: The operation regime determined by safety issues for the S-SOFC/GT system. Figure (a) also shows the boundaries corresponding to different safety constraints.

Analogous to the R-SOFC/GT system (refer to APPENDIX B), the "safe" feasible operating regime for the S-SOFC/GT system is identified by considering the constraints pertinent to safety issues listed in Table 4.3. As shown in Figure 4.6, various constraints (refer to Table 4.4 for their values) are applied to identify the "safe operation regime" for

different I_{com} values. To keep constant P_{sofc} over the entire load range, I_{com} should vary in a limited range, e.g., $I_{com} \in [1800, 2100]\ A \cdot m^{-2}$ for the sprinter system designed in Section 4.3 . Figure 4.6 (b) presents the 3D "safe operation regime" together with the low and high airflow (W_{air}) boundaries and different fixed-I_{com} slices. Note that the feasible operating region slightly shifts to the high airflow region as I_{com} decreases. The reason is that more fuel is reacted in the burner to increase the GT power, thereby feeding more air to the SOFC stack, as shown in Figure 4.6 (b).

Figure 4.6 (a) shows the 2D "safe operation regime" ($I_{com} = 1950 A \cdot m^{-2}$) with following issues occurring at certain regimes:

- Overheating appears for low air flow. As shown in Figure 4.6 (a), for the operation regime at the low airflow side of the T_{sofc} constraint line, simulations reveal that the cell temperature is steadily ramping beyond the valid region and causing compressor surge. This is similar to the result for the R-SOFC/GT system in APPENDIX B and the result in [14]. Note that the upper-bound constraint values for the burner, turbine and HEX temperatures, i.e., T_{cb}^{UB} and T_{HEX}^{UB}, determine the low airflow boundaries for regimes with large fuel flow inputs, as shown in Figure 4.6 (a).
- For the case of low fuel flow and high air flow, the SOFC is cooled down strongly, thereby leading to low cell voltage, low system efficiency, and increased risk of cell cracking due to low SOFC temperature. In this chapter, the region with a cell voltage less than 0.50V is considered invalid for the S-SOFC/GT system. This determines the high airflow boundary of the "safe operation regime".
- GT over-speed is likely to occur for very high air flow regions as in Figure 4.6 (a). In order to ensure proper functioning of the GT-generator while maintaining satisfactory efficiencies, the operation regime where the shaft speed lies outside the permissible range [N^{LB}, N^{UB}] (see Table 4.4 for their values) is blinded out.

Three groups of metrics are used to evaluate the SOFC/GT system performance: (1) temperature related variables (see Figure 4.7) including the mean value of T_{sofc}, the maximum/minimum local T_{sofc}, the maximum local temperature gradient T_{grad}, and the turbine inlet/outlet temperatures (TIT/TOT); (2) power related variables (see Figure 4.8)

such as the SOFC power P_{sofc}, compressor power P_{comp}, turbine power P_{turb}, generator power P_{gen}, net power P_{net}, and net efficiency η_{net}; and (3) other variables (Figure 4.9) such as cell voltage U_{sofc}, current density I_{com} for the R-SOFC/GT system or SOFC FU ratio for the S-SOFC/GT system, air excessive ratio AR, shaft speed N, CB pressure p_{cb} (p_{cb} equals the turbine inlet pressure p_{t1}), and power split ratio P_{gen}/P_{net}.

As shown in Figure 4.7, SOFC temperatures and turbine inlet/outlet temperatures all increase with respect to W_f because more fuel is burned in the CB to raise T_{cb} and the SOFC inlet air temperature T_{air}. All these temperatures decrease with respect to W_{air} due to the cooling effect. Moreover, unlike the conventional R-SOFC/GT system, as shown in Figure APX.3 (d) of APPENDIX B, the maximum temperature gradient T_{grad} decreases with respect to the absolute values of W_f and W_{air}, as presented in Figure 4.7 (d). This is because the increased fuel and air flows help to smooth the temperature distributions over the SOFC while the thermal energy released from the electro-chemical reaction remains fairly constant because the amount of fuel reacted in the SOFC remains constant.

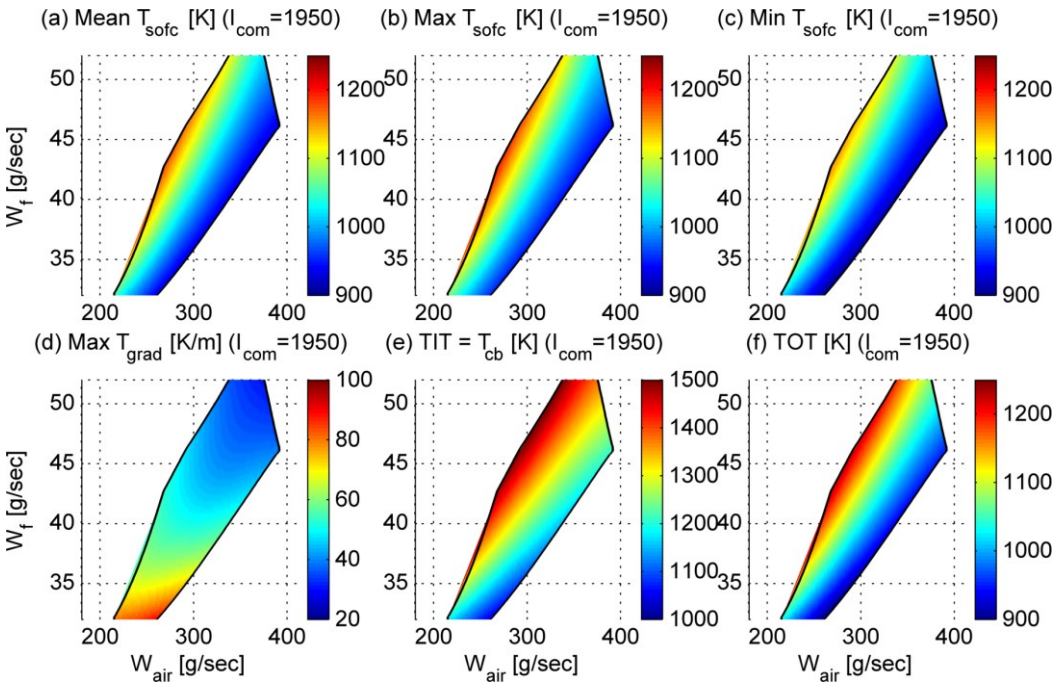

Figure 4.7: Temperature related variables for fixed current density (I_{com}=1950 $A \cdot m^{-2}$). The same colormaps are used for fiugre (a), (b), (c) and (f) to compare the temperatures.

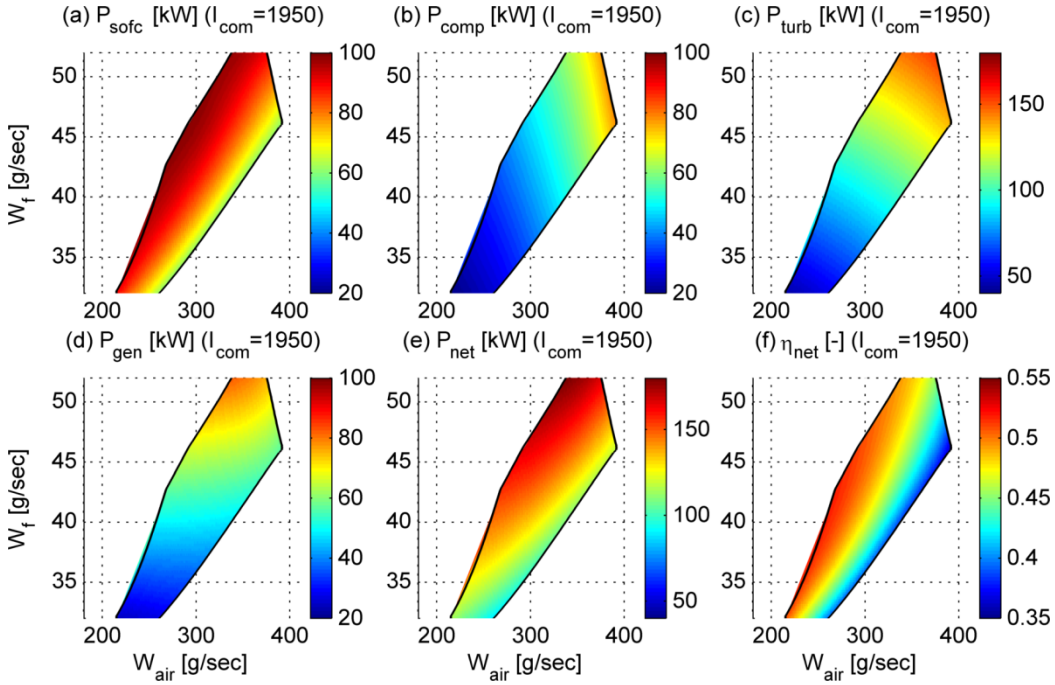

Figure 4.8: Power related variables for fixed current density (I_{com}=1950 $A \cdot m^{-2}$). Figure (a), (b) and (d) use the same colormaps. Figure (c) and (e) use another set of colormaps.

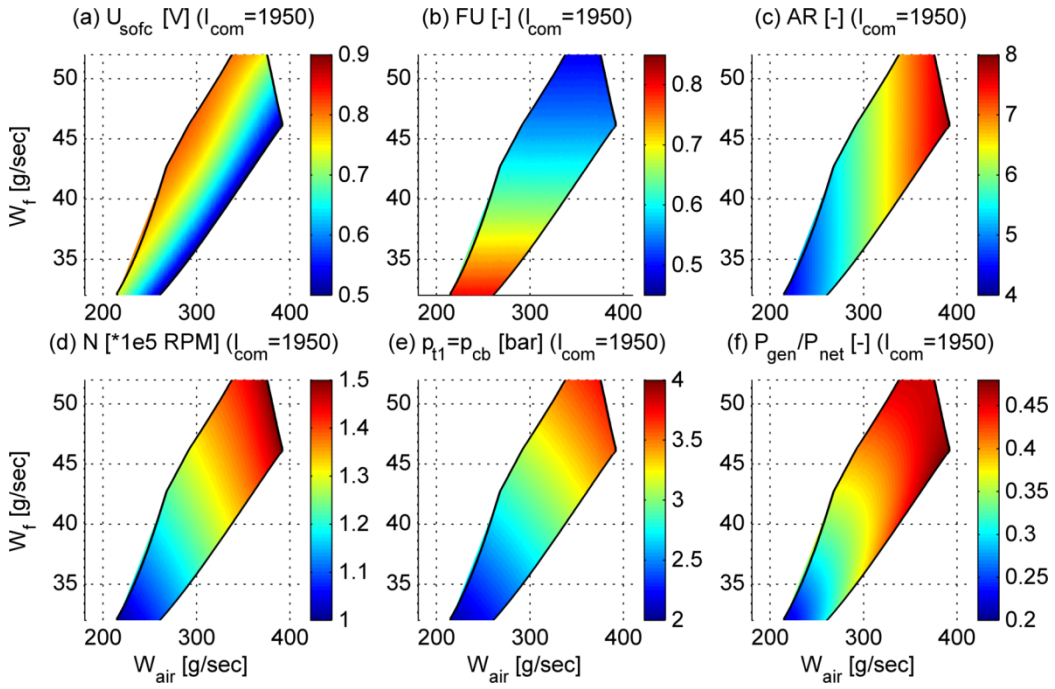

Figure 4.9: Other operational variables for fixed current density (I_{com}=1950 $A \cdot m^{-2}$) in the S-SOFC/GT system. Figure (a) to (c) are related to the SOFC while figure (d) to (f) are related to the GT-generator.

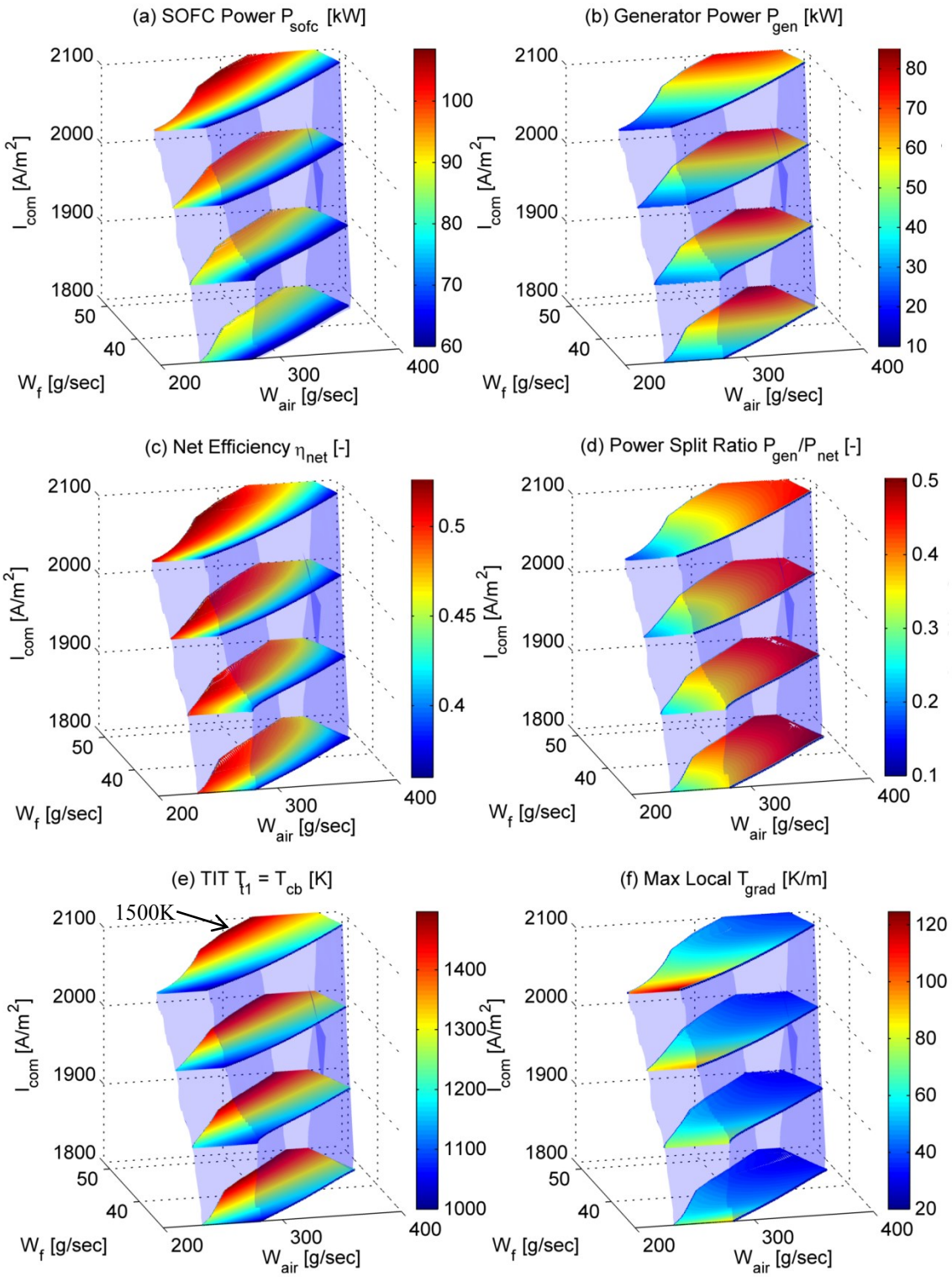

Figure 4.10: The "global" picture of the S-SOFC/GT system performance: (a) SOFC power; (b) generator power; (c) system efficiency; (d) power split ratio; (e) turbine inlet temperature; and (f) the maximum local cell temperature gradient.

Power related variables and other operating variables are presented in Figure 4.8 and Figure 4.9, respectively. Note that cell voltage U_{sofc} in Figure 4.9 (a) increases with respect to W_f due to the increasing open circuit voltage. The voltage U_{sofc} decreases with respect to W_{air} due to the reduced T_{sofc} (see Figure 4.7 (a)) caused by the cooling effect. The SOFC power P_{sofc} as in Figure 4.8 (a) has the same distributions as U_{sofc} for fixed I_{com} input because P_{sofc} is proportional to $U_{sofc} \cdot I_{com}$ [39]. As shown in Figure 4.9 (b), the fuel utilization coefficient FU is only a function of W_f since they are coupled by the fixed I_{com} input. Similarly, the SOFC's air excessive ratio AR in Figure 4.9 (c) is only a function of W_{air} as they are coupled by the fixed I_{com} input [24] as well.

Next, we study the GT-generator performance. As W_f increases, more unused fuel is burned in the CB to raise the turbine inlet temperature, thereby producing more turbine power P_{turb} and generator power P_{gen}, as shown in Figure 4.8 (c) and (d), respectively. The increased shaft power elevates the shaft speed N (Figure 4.9 (d)) and the compressor outlet pressure, which is close to the CB pressure p_{cb} in Figure 4.9 (e). Consequently, the compressor power P_{comp} in Figure 4.8 (b) has a similar distribution to the shaft speed. As shown in Figure 4.8 (e) and (f), both the net power P_{net} and efficiency η_{net} decrease with respect to W_{air} due to the cooling effect. Moreover, the most efficient operation point lies at the low airflow boundary of the feasible operation region, as shown in Figure 4.9 (f). This phenomenon is the same as that observed in the R-SOFC/GT system [14].

In the following, we examine the influence of varying I_{com} inputs and explore the "global" behavior over the 3D "safe operation regime". Figure 4.10 presents the contour-slice plots for the S-SOFC/GT system. The same conclusions as those drawn in the above analysis can be made for every fixed-I_{com} slice. As shown in Figure 4.10 (e), the burner temperature constraint T_{cb}^{UB} (T_{cb}^{UB}=1500K) becomes active over the low W_{air} and high W_f regions, i.e., the upper-left regions in Figure 4.10, for all fixed-I_{com} slices. Moreover, the feasible region slightly shifts to high airflow region as I_{com} decreases, thereby reducing T_{sofc} because of the cooling effect, as shown in Figure 4.6 (b). The fuel cell power P_{sofc} decreases significantly as I_{com} decreases, as shown in Figure 4.10 (a). This is due to the reduced I_{com} input and T_{sofc}. As shown in Figure 4.10 (b), P_{gen} slightly increases as I_{com} decreases, since more fuel is burned in the burner to drive the turbine to produce more

GT power. Consequently, the power split ratio P_{gen}/P_{net} increases as I_{com} decreases, as shown in Figure 4.10 (d). The system efficiency η_{net} shown in Figure 4.10 (c) decreases with respect to I_{com} mainly due to the reduced T_{sofc}. The maximum local T_{grad} (i.e., the spatial cell temperature gradient) shown in Figure 4.10 (f) decreases with respect to I_{com} due to the reduced degree of electro-chemical reactions in the SOFC and the increased airflow that helps to smooth the cell temperature distributions.

4.4.3 Influence of the Burner Temperature Constraint

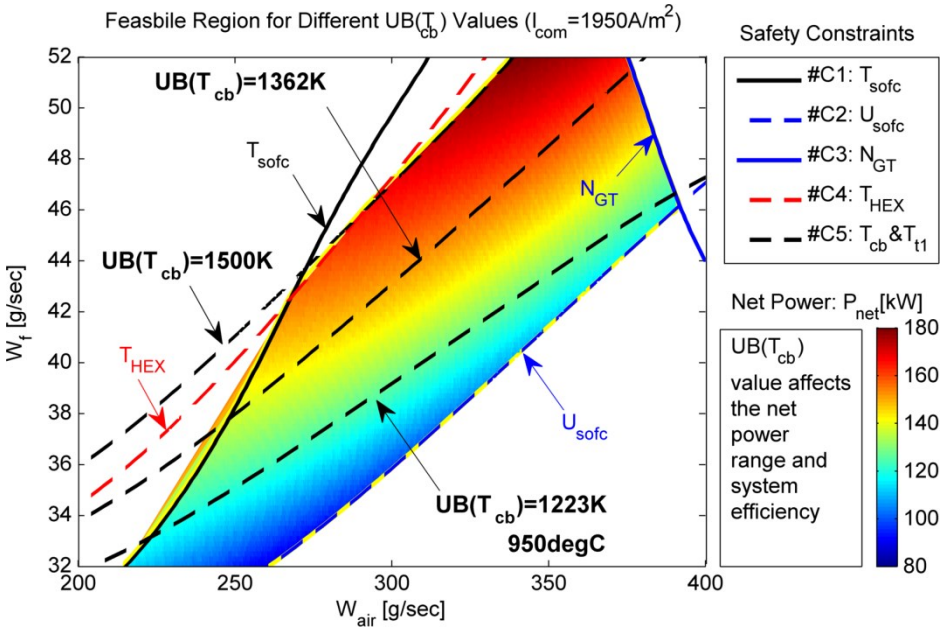

Figure 4.11: Effects of the CB temperature constraint values on the feasible region and net power range. In this figure, the regimes above the T_{cb} lines are considered infeasible because they will cause burner/turbine overheating and even system breakdown.

Table 4.5 Effects of the T_{cb}^{UB} value on the net power range and system efficiency

T_{cb}^{UB} $[K]$	1223	1362	1500
P_{net}^{min} $[kW]$	88.3	88.3	88.3
P_{net}^{max} $[kW]$	121.9	161.4	179.7
η_{net}^{max} [%]	39.9%	47.9%	52.7%

The maximum permissible CB temperature, i.e., the upper bound value T_{cb}^{UB}, has a significant effect on the feasible region, since it determines the low airflow boundary for high fuel flow (W_f) inputs. As shown in Figure 4.11, the feasible operating region shrinks

as T_{cb}^{UB} decreases, reducing the system net power range, as summarized in Table 4.5. For example, T_{cb}^{UB} decreases from 1500K to 1223K if the high-temperature CB in Figure 2.12 is replaced with a single-stage metallic burner. Then, the maximum net power P_{net}^{max} will decrease from 179.7kW to 121.9kW. Therefore, in order to meet the power demand and specific operation requirements for the target system, the multi-stage, high-temperature CB concept discussed in Section 2.4 should be used for the S-SOFC/GT system because (1) it can be operated at high temperatures; and (2) the metal-type substrates used in the CB has good performance with respect to thermal gradient/shock, thereby allowing rapid change of burner temperature for fast load following operations.

4.4.4 The "Actual" Operation Envelope and System Performance

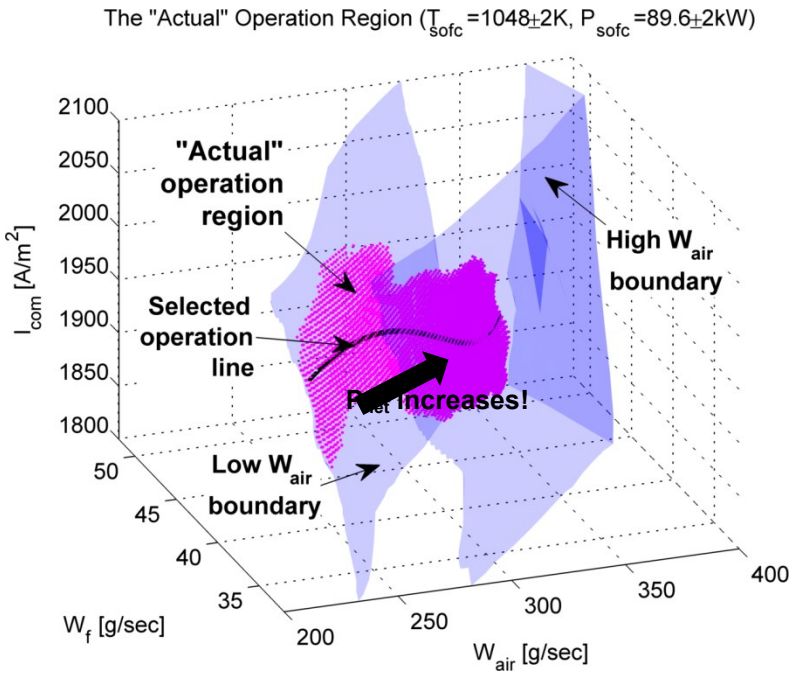

Figure 4.12: The "actual" feasible operation surface generated by applying the additional constraints of keeping constant P_{sofc} and constant T_{sofc} over the whole net power range. Note that P_{net} increases with respect to W_f over the "actual" operation surface.

The additional constraints of keeping constant P_{sofc} and T_{sofc} over the entire load range, which is one of the most important requirements for the S-SOFC/GT system, is not considered when determining the "safe operation regime" in the last section. The "actual" operation regime with the constant P_{sofc} and T_{sofc} constraints incorporated is a subset of

the 3D "safe operation regime" in Figure 4.6. For example, as shown in Figure 4.12, the "actual" operation region corresponding to the additional constraints of $\{T_{sofc} \in 1048 \pm 2K, P_{sofc} \in 89.6 \pm 2kW\}$ is a surface located inside the "safe operation regime". Note that the irregular boundary of this operational surface is because of numerical calculation errors. Moreover, as shown in Figure 4.12 and Figure 4.13, we can get an operation line by fitting the point cloud data over the "actual" operating surface into a single curve. This will give the same results as the strategy in Section 4.2 to keep fairly constant P_{sofc} and T_{sofc}. In particular, as shown in Figure 4.13 (d), less than 1% and 0.1% percentage errors for P_{sofc} and T_{sofc} have been achieved over the fitted operation line.

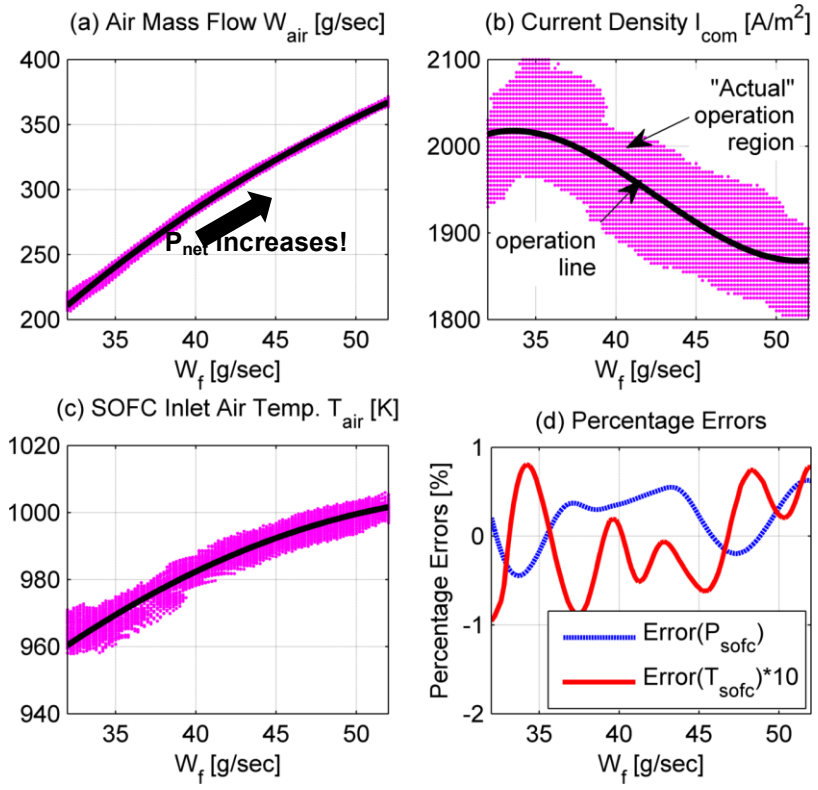

Figure 4.13: The "actual" operating surface and fitted operation line to keep fairly constant SOFC power/temperature. (a) air flow W_{air}; (b) current density I_{com}; (c) SOFC inlet air temperature T_{air}; and (d) P_{sofc} and T_{sofc} errors along the fitted operation line.

However, the "actual" operation surface shown in Figure 4.12, which corresponds to particular values of P_{sofc} and T_{sofc}, only covers a very limited portion of the 3D "safe operation regime". We would like to explore the "global" picture of the sprinter system

and investigate the influence of P_{sofc} and T_{sofc} setting-values (i.e., the desired constant values to be maintained during system operation). To this end, we will study the "actual" operational envelope for the S-SOFC/GT system by investigating the "actual" operational surfaces for different setting-values of P_{sofc} and T_{sofc}, as shown in Figure 4.14 (a). The specific requirement of keeping fairly constant P_{sofc} and T_{sofc} in the S-SOFC/GT system can be satisfied over each of the operational surfaces in Figure 4.14 (a).

Let P_{SET} and T_{SET} denote the setting-values for P_{sofc} and T_{sofc}, respectively. P_{SET} is expected to be an increasing function of T_{SET}. Although different combinations of P_{SET} and T_{SET} setting-values can be used, intensive simulations indicate that we can reduce the number of free variables by applying the P_{SET}~T_{SET} relation presented in Figure 4.14 (b), without sacrificing the system performance. This will simplify our study on the "actual" operation envelope and sensitivity analysis. Figure 4.14 (a) shows a series of operational surfaces with $\{P_{sofc}, T_{sofc}\} \in \{(1 \pm 2\%)P_{SET}, T_{SET} \pm 2K\}$ for different T_{SET} values. Note that the surfaces are color-coded with respect to T_{SET} in Figure 4.14 (a).

It is not easy to perform direct analysis over the operational surfaces presented in Figure 4.14 (a) because we have two degrees of freedom over each T_{SET} surface. In order to further simplify the subsequent analysis, we reduce the dimensionality of the problem as follows. First, for each T_{SET} surface in Figure 4.14 (a), we find a fitted operation line by applying the curve-fitting technique in Figure 4.12 and Figure 4.13. Second, as shown in Figure 4.15, we create a surface by combining these fitted operation lines. This surface is referred to as the "fitted operation surface" in this dissertation. The operational lines in Figure 4.15 are color-coded with respect to T_{SET}. For the "fitted operation surface", there are two free variables, i.e., T_{SET} and W_f, as shown in Figure 4.16.

In order to gain "global" knowledge of the sprinter system, we will investigate the system performance, as described in Figure 4.16 to Figure 4.19, over the "fitted operation surface". We will also study the influence of T_{SET} over the "fitted operation surface". The high W_f and low T_{SET} region, i.e., the upper-left blank region in Figure 4.16, is infeasible because the GT speed constraint N_{GT}^{UB} is violated. On the other hand, the low W_f and high T_{SET} region, i.e., the lower-right blank region in Figure 4.16, is bounded by the low W_{air} boundary of the 3D "feasible operation regime" in Figure 4.15.

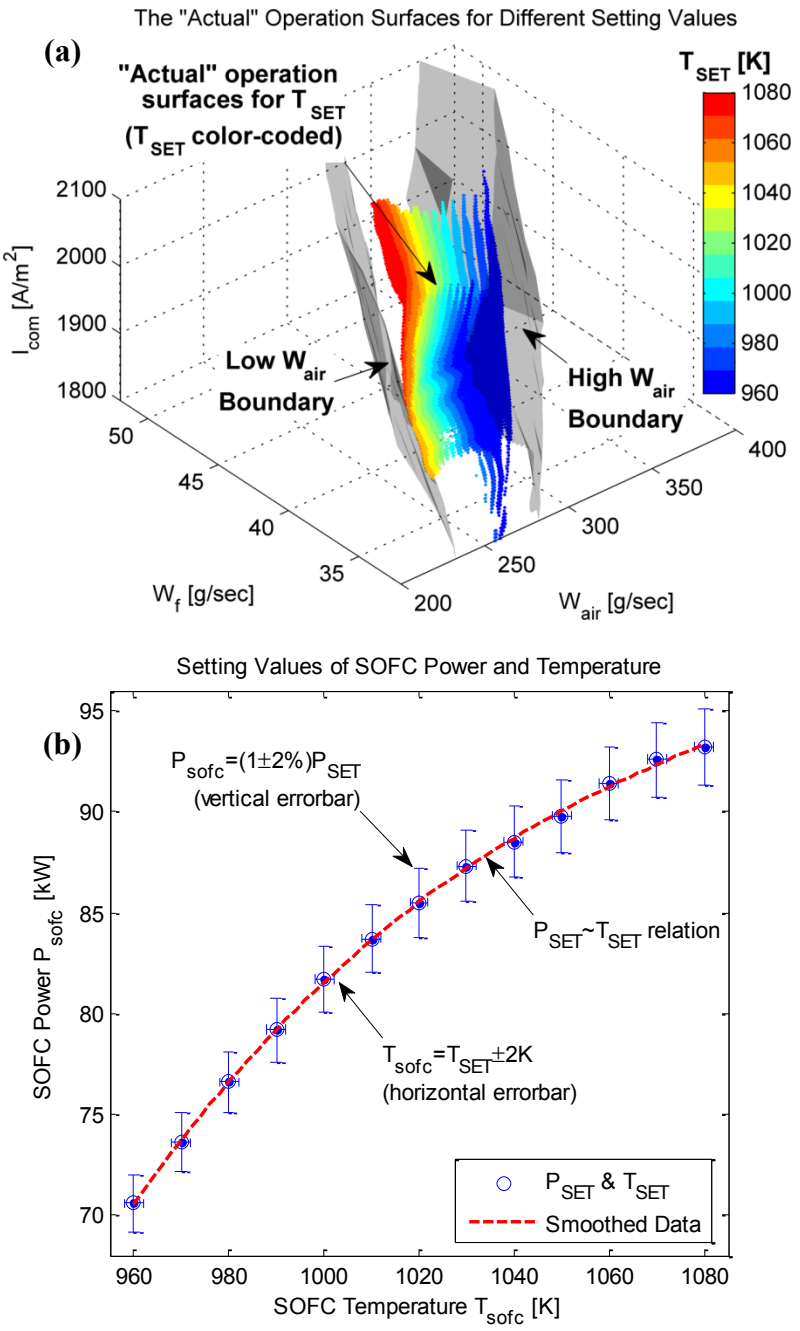

Figure 4.14: The "actual" operation surfaces plotted over the 3D "safe operation regime" in figure (a) for different setting-values presented in figure (b). The SOFC power P_{sofc} equals $(1 \pm 2\%)P_{SET}$ and the cell temperature T_{sofc} equals $T_{SET} \pm 2$K. For each T_{SET} surface presented in figure (a), there are two degrees of freedom and the net power P_{net} increases with respect to the W_f input.

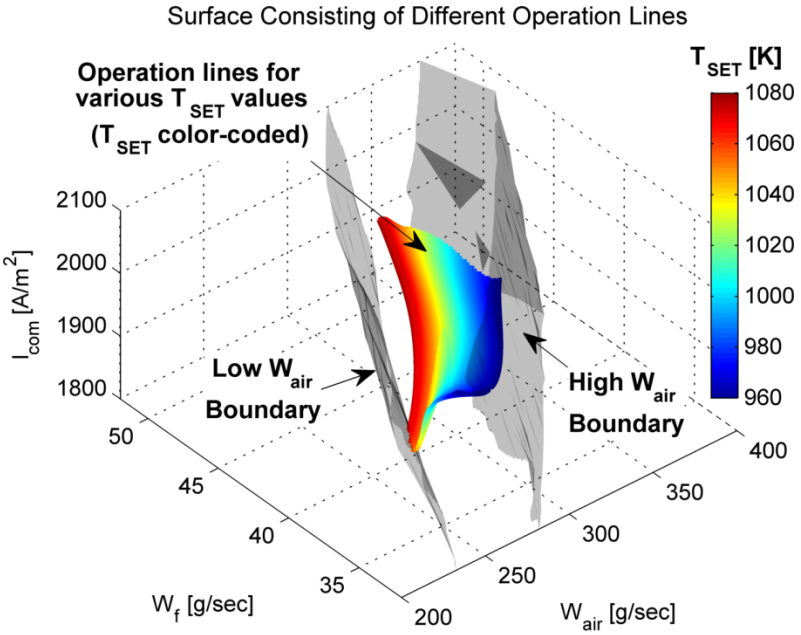

Figure 4.15: The "fitted operation surface" consisting of different operation lines that are generated by applying curve-fitting technique over each T_{SET} surface in Figure 4.14 (a). For each fitted T_{SET} operation line, the net power P_{net} increases with respect to W_f.

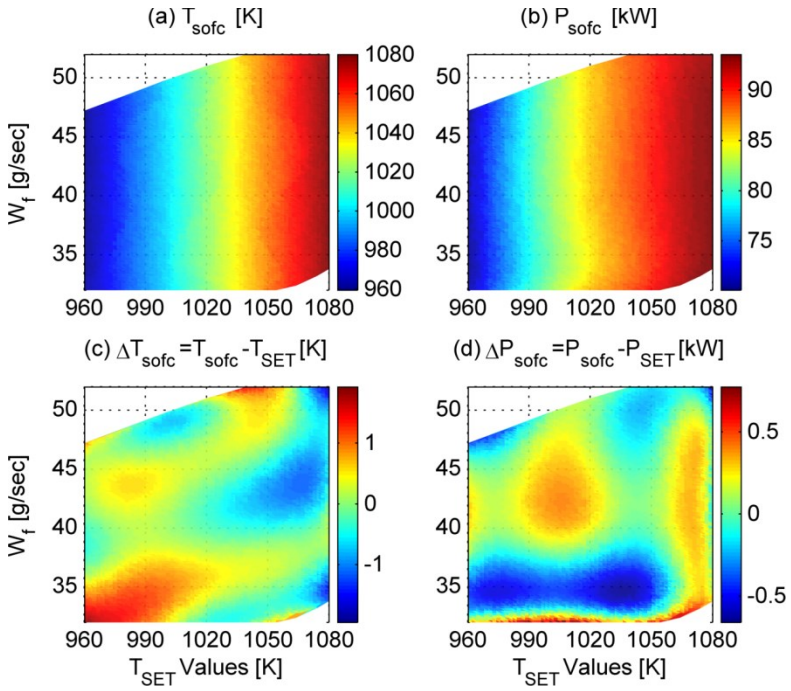

Figure 4.16: Fairly constant T_{sofc} and P_{sofc} are achieved for each T_{SET} vertical line over the "fitted operation surface", as shown in figure (a) and (b), respectively. Figure (c) and (d) show the variations of T_{sofc} and P_{sofc} with respect to their respective setting-values.

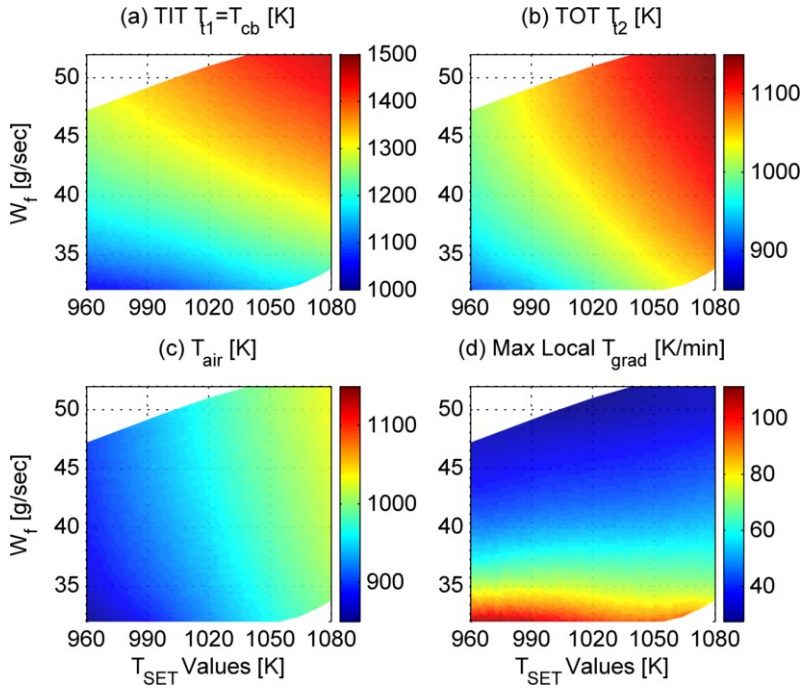

Figure 4.17: Temperature related variables over the "fitted operation surface".

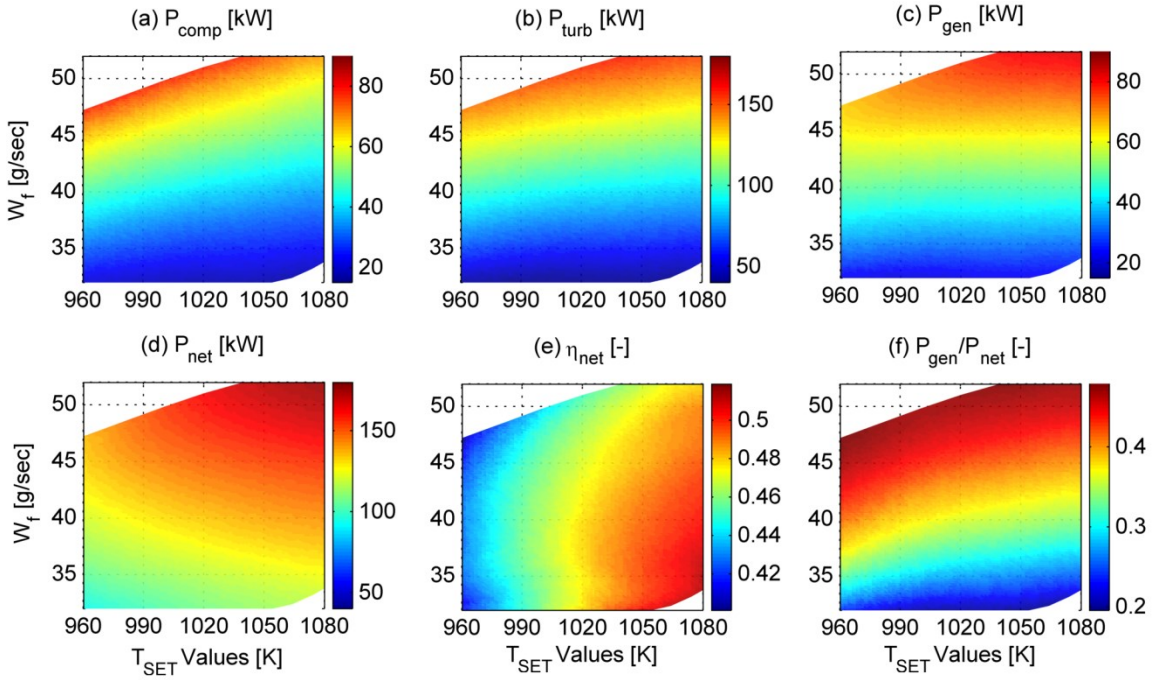

Figure 4.18: Power related variables over the "fitted operation surface". Figure (a) and (c) use the same colormaps while figure (b) and (d) use another set of colormaps.

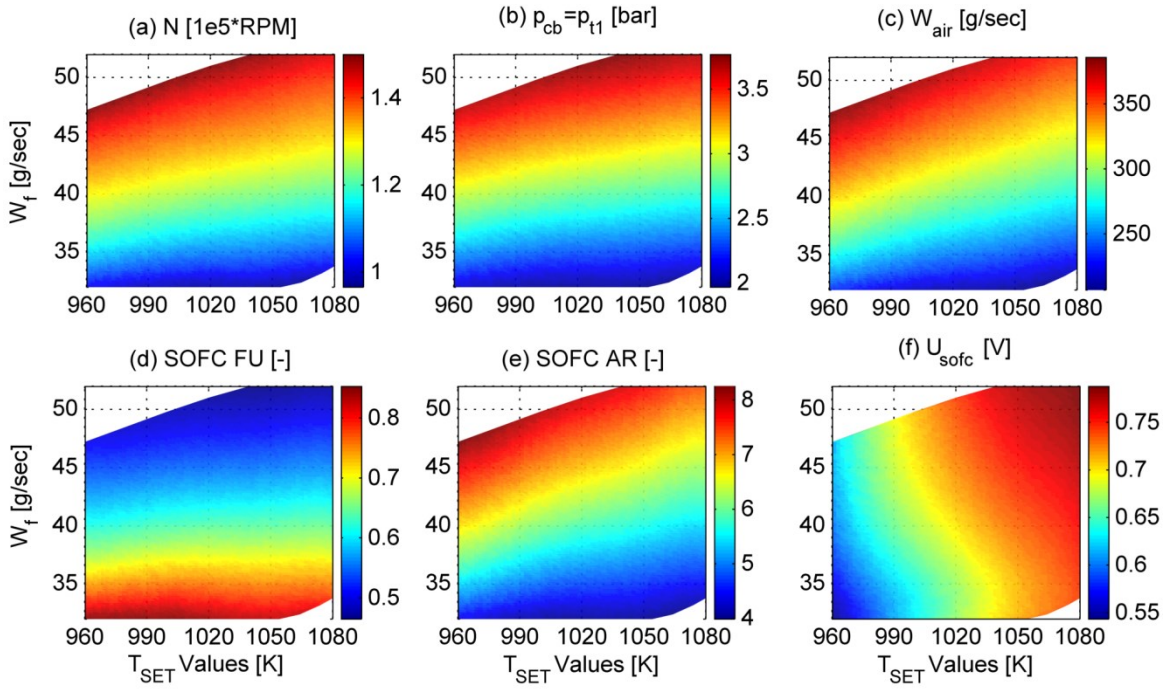

Figure 4.19: Other performance variables over the "fitted operation surface".

First, we check if the constraints of keeping fairly constant T_{sofc} and P_{sofc} can be satisfied for each T_{SET} line over the "fitted operation surface". As shown in Figure 4.16, fairly constant T_{sofc} and P_{sofc} have been achieved for each T_{SET} vertical line. Let ΔT_{sofc} and ΔP_{sofc} denote the differences of the actual values of T_{sofc} and P_{sofc} with respect to their setting values. As shown in Figure 4.16 (c) and (d), very small differences between the actual and the setting values, e.g., $|\Delta T_{sofc}| \leq 2K$, $|\Delta P_{sofc}| \leq 1kW$, are achieved over the "fitted operation surface". Hence, in order to keep T_{sofc} and P_{sofc} at their respective setting-values, we can allocate the S-SOFC/GT system inputs according to those for the constant T_{SET} lines over the "fitted operation surface".

Next, we investigate the system performance over the "fitted operation surface". The temperature, power and other operation related variables are shown in Figure 4.17, Figure 4.18 and Figure 4.19, respectively. In particular, we study the system performance over each constant T_{SET} line and investigate the influence of varying T_{SET} values through sensitivity analysis. Conclusions and highlights acquired from these studies will facilitate the S-SOFC/GT system design and operation in the future.

4.4.4.1 System performance over each constant T_{SET} line

As shown in Figure 4.18 (d), for each constant T_{SET} line, the fuel flow input W_f is an increasing function of P_{net}. The voltage U_{sofc} in Figure 4.19 (f) increases with respect to W_f because U_{OCV} increases with respect to the fuel and air concentrations, according to the Nernst equation shown in Eqn. (2.2). To keep constant P_{sofc}, I_{com} should be reduced when increasing W_f, according to the operational strategy in Section 4.2. Consequently, more fuel will be burned in the CB, thereby elevating the CB and turbine temperatures, as shown in Figure 4.17 (a) and (b). Meanwhile, the SOFC FU ratio, which varies in a wide range, reduces with respect to W_f, as shown in Figure 4.19 (d). Moreover, T_{air} shown in Figure 4.17 (c) increases with respect to W_f since more energy from the turbine exhaust can be recuperated by the HEX. This helps to counteract the cooling effect caused by the increased W_{air}, as shown in Figure 4.19 (c), thereby keeping constant T_{sofc}. In addition, as shown in Figure 4.17 (d), the maximum T_{grad} reduces with respect to W_f because the increased airflow helps to smooth the temperature distributions over the SOFC. This is a benefit compared with the R-SOFC/GT system, in which T_{grad} increases with respect to the air and fuel flows, as shown in Figure APX.3 (d).

Next, we study the power performance, which is shown in Figure 4.18. Over each constant T_{SET} line, the turbine power P_{turb} in Figure 4.18 (b) increases with respect to W_f (which is nearly proportional to P_{net}) due to the increased turbine temperature. This helps to accelerate the shaft speed N and increase the CB pressure p_{cb}, as shown in Figure 4.19 (a) and (b), respectively. P_{comp} increases as more air is delivered, as shown in Figure 4.18 (a). Moreover, P_{gen} is only a function of W_f and the constant P_{gen} contourlines are nearly horizontal, as shown in Figure 4.18 (c). This is not surprising since P_{gen} is expected to be proportional to the thermal energy released from the SOFC fuel exhaust, whose flow rate equals $(1 - FU)W_f$. This part of thermal energy will be used to drive the GT-generator to produce P_{gen}. Moreover, for each T_{SET} line, the power split ratio P_{gen}/P_{net}, as shown in Figure 4.18 (f), increases with respect to W_f because P_{gen} increases with W_f while P_{sofc} remains fairly constant. In addition, as more power is produced by the GT-generator, the system efficiency η_{net}, as shown in Figure 4.18 (e), decreases because the GT-generator has a much lower fuel-to-electrical efficiency than the SOFC [21].

4.4.4.2 Influence of the SOFC temperature setting-values

The SOFC temperature setting-value, T_{SET}, has a significant effect on the system performance. As shown in Figure 4.17, all the temperature related variables increase with respect to T_{SET}. However, the T_{grad} value, as shown in Figure 4.17 (d), is insensitive to T_{SET}. Moreover, for each W_f input, P_{sofc} in Figure 4.16 (b) increases with respect to T_{SET} while P_{gen} in Figure 4.18 (c) remains fairly constant when varying the T_{SET} value. Hence, both P_{net} and η_{net} increase with respect to T_{SET} while the ratio P_{gen}/P_{net} decreases with respect to T_{SET}, as shown in Figure 4.18 (d) to (e). Hence, in order to achieve high system efficiency, the SOFC stack should be operated at high temperature.

However, too high SOFC temperature will affect the system net power range and the power turn-down ratio, which is defined as the ratio of P_{net}^{max} with respect to P_{net}^{min}. As shown in Figure 4.18 (d), a smaller power variation range and a smaller power turndown ratio are achieved for the case of $T_{SET} = 1080K$, compared to the case of $T_{SET} = 1050K$, even though a higher efficiency is achieved in the former case. Thus, a trade-off between the efficiency and the power turndown ratio should be made when choosing T_{SET}. For the S-SOFC/GT system in this chapter, T_{SET} should be around 1050K for efficient operations while meeting the desired power range requirement for dynamic load following.

4.5 Steady-State System Optimization

The S-SOFC/GT system involves multiple actuators and inputs which will dictate the overall system efficiency. In particular, for a given W_f input, there are infinitely many combinations of I_{com} and P_{gen} that generate different net powers. In this section, we will formulate constrained optimization problems to determine the steady-state operation line [14], i.e., the static feed-forward map in [15], for the proposed S-SOFC/GT system. We will also investigate the system performance over the optimal steady-state operation line.

4.5.1 Optimization Problem Formulation

In order to determine the maximum steady-state P_{net} output for a given W_f input while satisfying the safety and SOFC power/temperature constraints for the S-SOFC/GT system, a constrained optimization problem is formulated as:

$$\max_{I_{com},W_{air}} \quad (P_{net})\ for\ a\ given\ W_f,$$
$$such\ that \quad \begin{cases} (1)\{W_f, I_{com}, W_{air}\} \in \mathrm{O}_{\mathrm{safe}}(\mathrm{Sprinter}), \\ (2a)T_{sofc} \in [T_{SET} - \Delta T_{SET}, T_{SET} + \Delta T_{SET}], \\ (2b)P_{sofc} \in [P_{SET} - \Delta P_{SET}, P_{SET} + \Delta P_{SET}], \end{cases} \tag{4.4}$$

where $\mathrm{O}_{\mathrm{safe}}(\mathrm{Sprinter})$ is the feasible set corresponding to the 3D "safe operation regime" (see Figure 4.6 for example) determined by considering the constraints pertinent to safety issues discussed in Section 4.4.1; X_{SET} $(X = P, T)$ and $\Delta X_{SET}(X = P, T)$ are the constant setting-values and permissible errors for the SOFC power and temperature.

Let $\mathrm{O}(\mathrm{Sprinter})$ denote the "actual" feasible set. Then, we have:

$$\begin{aligned} \mathrm{O}(\mathrm{Sprinter}) = \{(W_f, I_{com}, W_{air}) \in \mathrm{O}_{\mathrm{safe}}(\mathrm{Sprinter}) | T_{sofc} \\ \in [T_{SET} - \Delta T_{SET}, T_{SET} + \Delta T_{SET}], P_{sofc} \\ \in [P_{SET} - \Delta P_{SET}, P_{SET} + \Delta P_{SET}]\}. \end{aligned} \tag{4.5}$$

We can visualize the "actual" feasible set $\mathrm{O}(\mathrm{Sprinter})$ for the sprinter system. For example, $\mathrm{O}(\mathrm{Sprinter})$ for the case of $T_{SET} = 1048K$, $P_{SET} = 89.6kW$, $\Delta T_{SET} = 2K$, and $\Delta \mathrm{P}_{SET} = 2kW$ is shown in Figure 4.12. The operating surfaces in Figure 4.14 (a) denote the "actual" feasible sets for different T_{SET} and P_{SET} values shown in Figure 4.14 (b).

Plug Eqn. (4.5) into Eqn. (4.4), the optimization problem is re-formulated as:

$$\max_{I_{com},W_{air}} \quad (P_{net})\ for\ a\ given\ W_f,$$
$$such\ that \quad \{W_f, I_{com}, W_{air}\} \in \mathrm{O}(\mathrm{Sprinter}). \tag{4.6}$$

The optimization problems in Eqn. (4.4) and Eqn. (4.6) can be solved by using the Simulink model and numerical optimization algorithms. By repeating the optimization for different fuel flows, we can get the optimal steady-state operation line within the valid operation regime for the S-SOFC/GT system.

For the S-SOFC/GT system, the SOFC should be operated at high temperatures to achieve high system efficiency. However, too high SOFC temperature will affect the net

power range and power turndown ratio, as discussed in Section 4.4.4. In this chapter, in order to achieve efficient operation while maintaining a satisfactory net power range for dynamic load following, T_{SET} and P_{SET} are taken at 1048K and 89.6kW, respectively. In addition, $\Delta T_{SET} = 2K$ and $\Delta P_{SET} = 2kW$ are selected for the optimization problems. The corresponding "actual" feasible set O(Sprinter) and the "optimal" steady-state operation line identified by Eqn. (4.6) are shown in Figure 4.20.

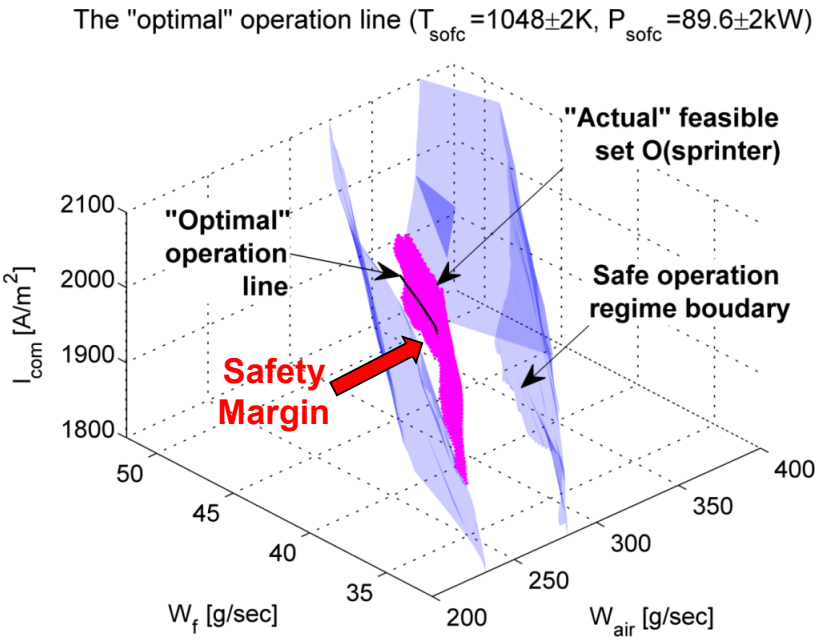

Figure 4.20: The "optimal" steady-state operation line and the "actual" feasible set. The safety margin between the "optimal" operation line and the safety regime boundary allows for less stringent operation requirements as compared to the R-SOFC/GT system.

4.5.2 Performance of the Steady-State Operation Line

Figure 4.21 shows the system performance over the optimal operation line for the S-SOFC/GT system. Compared with its recuperating counterpart in APPENDIX B (P_{net} varies from 78.8kW to 187.9kW), the S-SOFC/GT system has a smaller net power range from 103.8 kW to 171.2 kW. In particular, the upper bound value of P_{net} is limited by the shaft speed constraint while the lower bound value of P_{net} is constrained by the low W_{air} boundary (a lower W_{air} value is infeasible because it will cause compressor surging [14]) of the "feasible operation regime", as discussed in Section 4.4.4.

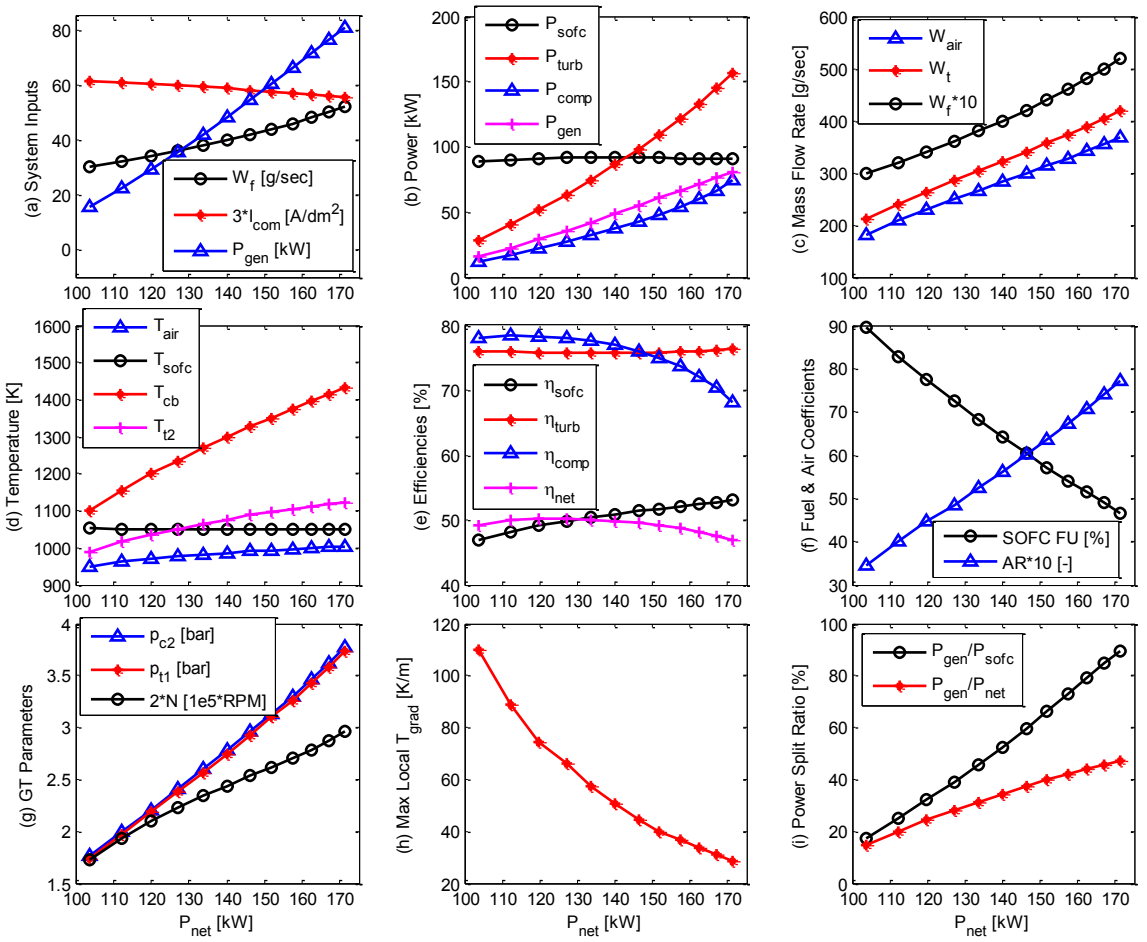

Figure 4.21: The S-SOFC/GT system performance along the optimal operation line.

The three system inputs (i.e., W_f, I_{com} and P_{gen}) that produce the optimal system efficiency are shown in Figure 4.21 (a). Note that W_f and P_{gen} are increasing functions of P_{net}, as expected. However, I_{com} slightly decreases with P_{net} to limit the P_{sofc} and T_{sofc} variations according to the operational strategy delineated in Section 4.2. This is different from the R-SOFC/GT system, in which I_{com} is an increasing function of P_{net}, as shown in Figure APX.12 (a) in APPENDIX B.

Fairly constant P_{sofc} and T_{sofc} have been achieved over the whole load range, as shown in Figure 4.21 (b) and (d). However, this is achieved by sacrificing the efficiency. Compared with its recuperating counterpart ($\eta_{net} \approx 55.8\%$), the S-SOFC/GT system has a poor efficiency, which varies from 46.8% to 50.2%, as shown in Figure 4.21 (e). In the

low P_{net} region, η_{net} increases with respect to P_{net} due to the reduced T_{grad}, as shown in Figure 4.21 (h). The reason is that uniform cell temperature distributions will lead to high efficiency operations [14]. In the medium to high P_{net} region, η_{net} decreases with respect to P_{net} because (1) more power is produced through the less-efficient GT-generator; and (2) the compressor efficiency η_{comp} decreases with respect to the net power.

As the net power P_{net} increases, the GT shaft speed N shown in Figure 4.21 (g) is increased to deliver more airflow, as shown in Figure 4.21 (c), to the SOFC while more unused fuel is reacted in the burner to drive the GT-generator to produce a considerable amount of electric power P_{gen}. The turbine gas flow W_t, turbine inlet temperature T_{t1} and inlet pressure p_{t1} are elevated to produce more P_{gen} as P_{net} increases, as shown in Figure 4.21 (c), (d) and (g), respectively. Compared with the conventional R-SOFC/GT system, in which P_{gen}/P_{net} varies around 20% [3], substantial variation of the power split ratio P_{gen}/P_{net} is achieved in the S-SOFC/GT system. As shown in Figure 4.21 (i), the power split ratio P_{gen}/P_{net} varies from 14.9% to 47.3% over the entire load range.

Compared with the R-SOFC/GT system, in which the SOFC FU ratio varies in a limited range, substantial variation of the SOFC FU ratio is observed. As shown in Figure 4.21 (f), the SOFC FU ratio decreases from 90% to less than 50% as P_{net} increases. In addition, unlike the R-SOFC/GT system, in which AR decreases with respect to P_{net}, as shown in Figure APX.12 (f) in APPENDIX B, the AR ratio is an increasing function of P_{net} in the S-SOFC/GT system, as shown in Figure 4.21 (f). This leads to a more uniform SOFC temperature distribution, e.g., the maximum T_{grad} decreases with respect to P_{net}, as shown in Figure 4.21 (h). This is a benefit of the proposed S-SOFC/GT system, which helps to reduce the risk of cell cracking for long life-cycle operation.

Table 4.6 summarizes the steady-state performance of the proposed S-SOFC/GT system and that of the conventional R-SOFC/GT system. Note that the "optimal" steady-state operation line is located at the feasible region boundary in the R-SOFC/GT system, as shown in Figure APX.11 (d) of APPENDIX B. In comparison, in the sprinter system, the "optimal" operation line is a subset of the "actual" feasible set $\mathrm{O(Sprinter)}$, as shown in Figure 4.20. Note that there is some safety margin left between the "optimal" operation

line and the boundary of the safe operation region. Compared to the R-SOFC/GT system, the safety margin allows for less stringent requirements for the S-SOFC/GT system.

Table 4.6 Steady-state performance of the SOFC/GT systems

Performance	R-SOFC/GT system	S-SOFC/GT system
System inputs	- W_f, P_{gen} and I_{com} are all increasing functions of P_{net}	- W_f and P_{gen} increase with P_{net} - I_{com} slightly decreases with P_{net}
Temperature related variables	- SOFC, CB and turbine temperatures increase with respect to P_{net} - Substantial variation of T_{sofc} - The temperature gradient T_{grad} increases with respect to P_{net}	- CB and turbine temperatures increase with respect to P_{net} - Fairly constant T_{sofc} - The temperature gradient T_{grad} decreases with respect to P_{net} - Higher CB/turbine temperatures than the R-SOFC/GT system
Power related variables	- SOFC, GT, and generator powers all increase with respect to P_{net} - Substantially varying P_{sofc} - Limited GT-generator power - $P_{gen}/P_{net} \approx 20\%$, relatively constant power split ratio	- GT and generator powers increase with respect to P_{net} - Fairly constant P_{sofc} - Significantly enhanced P_{gen} - P_{gen}/P_{net} varies in a large range, e.g., from 10% to 50%
SOFC FU and AR ratio	- The SOFC FU ratio varies in a small range, e.g., $FU \approx 85\%$ - The AR ratio decreases with P_{net}	- The SOFC FU ratio varies in a large range, e.g., FU=50% - 90% - The AR ratio increases with P_{net}
Steady-state operation line	- P_{net} varies in [78.9, 187.9] kW - η_{net} varies in [55.5%, 56.1%] - Located at the boundary of the safe feasible operation regime	- P_{net} varies in [103.8, 171.2] kW - η_{net} varies in [46.8%, 50.2%] - Located inside the safe feasible operation regime with certain safety margin

CHAPTER 5
Control Analysis and Design of Sprinter SOFC/GT systems

The feasibility of the S-SOFC/GT concept is established in CHAPTER 4, where it is shown that the system can indeed achieve constant SOFC power and temperature while supporting the load in the wide spectrum of net power range. In this chapter, the transient capabilities of the S-SOFC/GT system will be addressed. In particular, control analysis and feedback design will be presented. In Section 5.1, the BIBO stability of the steady-state operating points is investigated through numerical simulations and linearized system analysis of a simplified model that captures the dominating dynamics of the S-SOFC/GT system. Meanwhile, a PI-type shaft speed feedback controller is proposed to stabilize the system at the desired operating point. In order to gain fundamental insights on transient characteristics and operation challenges of the system, open-loop and RGA (relative gain array) analyses are performed in Section 5.2 and the control implications of these analysis results are discussed. Feedback control design is presented in Section 5.3. Both load step-up and step-down transients are investigated. Compared to the conventional R-SOFC/GT system, the S-SOFC/GT system achieves far superior transient performance.

5.1 Stability Analysis of Steady-State Operation Points

The hybrid SOFC/GT system has three inputs: fuel flow W_f, current density I_{com}, and generator load P_{gen}. As discussed in [14], the R-SOFC/GT system is claimed to be unstable with a constant P_{gen} input in some regions of the feasible operation regime. The reason is that a step up or step down in P_{gen} will accelerate or decelerate the shaft with no new equilibrium can be found within the valid bounds of the shaft speed [14]. Variable shaft speed control is often used to solve this problem [4], [14]. In Section 5.1.1, we will demonstrate the stability problem through numerical examples and develop appropriate

control strategy for the sprinter system. Theoretical analysis for the BIBO (bounded input bounded output [70]) stability of the steady-state operations is given in Section 5.1.2.

5.1.1 Numerical Case Study

Without loss of generality, the optimal set-point for P_{net} = 118.7kW is used in the following case studies. The point (A) in Figure 5.1 corresponds to the selected set-point. For the initial condition, the system is assumed to be working at set-point (A) at steady-state. Figure 5.2 presents simulation results of the following case studies while Figure 5.1 shows the corresponding trajectories plotted in the compressor map.

Case-C1: **a small (20-Watt) step decrease of P_{gen} is applied to the system**. As shown in Figure 5.2 (a) and (d), an abrupt increase of shaft speed can be observed due to the rapid increase of net shaft power ΔP, which is defined in Eqn. (5.1). Consequently, a significant amount of airflow is delivered to cool the SOFC rapidly, thereby leading to extremely low SOFC power generation, as shown in Figure 5.2 (e) and (f). Note that the hybrid system will eventually settle at the point (B), which is located at the high airflow region in Figure 5.1. However, both T_{sofc} and P_{sofc} are far away from their respective desired setting values, as shown in Figure 5.2 (case-C1).

$$\Delta P = P_{tc} - P_{gen} = P_t \eta_m - P_c - P_{gen}. \tag{5.1}$$

Case-C2: a small (20-Watt) step increase of P_{gen} is applied to the system. The shaft decelerates rapidly because there is not enough shaft power to meet the desired P_{gen} demand, as shown in Figure 5.2 (a) and (d). Further drop of net shaft power ΔP due to the reduced GT shaft speed will lead to an irreversible process, which will cause the eventual system shutdown [15], as shown in Figure 5.2. Therefore, the S-SOFC/GT system tends to be unstable with a fixed P_{gen} input at operation point (A).

Case-C3: shaft speed control is used to stabilize the system. Feedback control of the airflow or shaft speed is often used to stabilize the SOFC/GT systems [4], [14]. In this section, a PI-type shaft speed controller, as expressed in Eqn. (5.2), is implemented to stabilize the S-SOFC/GT system:

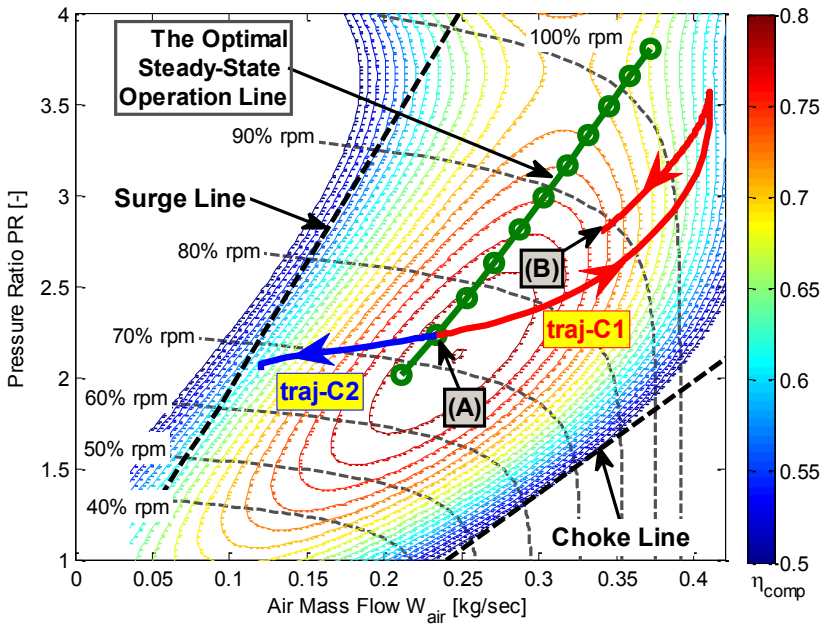

Figure 5.1: The optimal operation line and simulated trajectories in the compressor map. A small step decrease/increase of P_{gen} is applied for Case-C1/Case-C2, respectively.

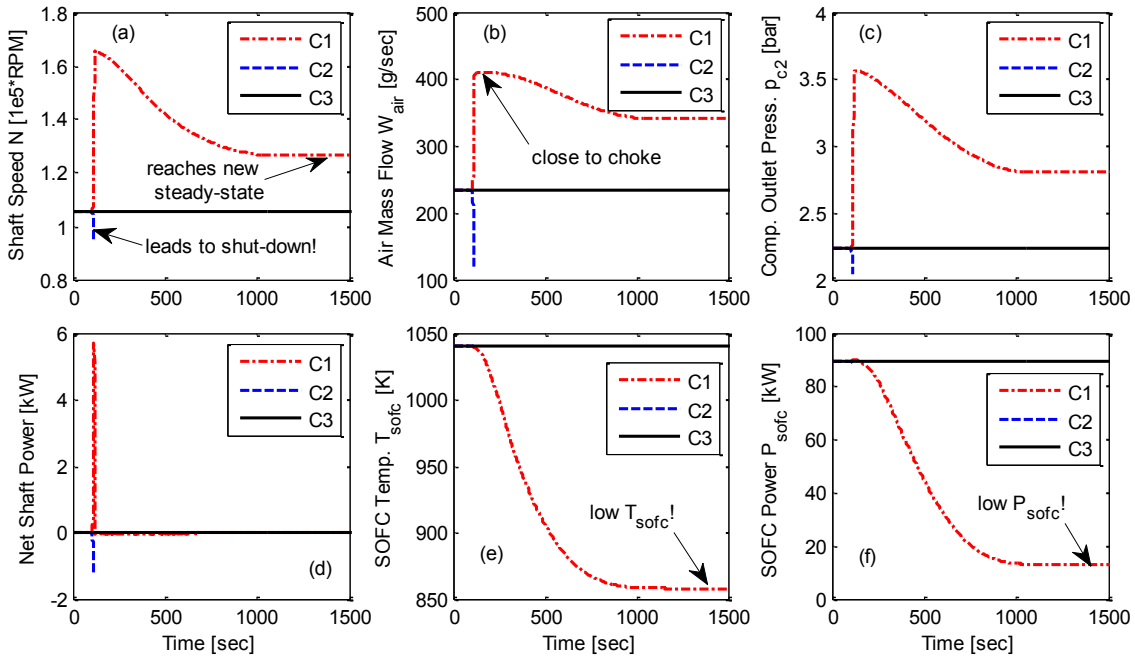

Figure 5.2: Simulation results for steady-state operations of the S-SOFC/GT system. A small (<0.1%) step decrease of P_{gen} and a small (<0.1%) step increase of P_{gen} are applied to the system in Case-C1 and Case-C2, respectively. For Case-C3, a PI-type shaft speed control stabilizes the system when shaft power perturbation is applied.

$$P_{gen}(s) = (k_P + k_I/s)\big(N(s) - N_{des}(s)\big), \tag{5.2}$$

where N_{des} is the desired shaft speed corresponding to the selected steady-state set-point for net power demand P_{net}^{des}. The relation between N_{des} and P_{net}^{des} can be determined from the feed-forward map in Figure 4.21. In Case-C3, a step-up perturbation and a step-down perturbation are applied to the GT-generator shaft to emulate varying resistance torque at 100-sec and 1000-sec, respectively. The amplitudes of the shaft perturbation power are less than 0.1% of P_{gen}. The feedback controller (k_P=$\frac{10W}{RPM}$, k_I=$\frac{20W}{RPM}$) in Eqn. (5.2) is able to stabilize the system at desired operation point, as shown in Case-C3 of Figure 5.2,

Similar analysis has been performed for other operation points along the optimal steady-state operation line in Figure 4.21. Simulation results indicate that the steady-state operation points tend to be unstable with a fixed P_{gen} input, especially for those located at the low/medium airflow regions. Detailed stability analysis for steady-state operations of the S-SOFC/GT system will be performed in the next section.

5.1.2 Theoretical Analysis

In this section, a simplified "2-state" model will be developed to depict the main dynamics of the S-SOFC/GT system. The BIBO stability for steady-state operations will be investigated through linearized analysis of this nonlinear "2-state" model.

Section 5.1.1 reveals that the power/energy balance on the shaft is critical to the system stability. Recall that the shaft rotational dynamics is governed by:

$$\frac{dN}{dt} = \frac{P_t\eta_m - P_c - P_{gen}}{\alpha \cdot N \cdot J} = \frac{P_{tc} - P_{gen}}{\alpha \cdot N \cdot J}, \tag{5.3}$$

where the shaft's acceleration dN/dt is a function of the GT shaft power P_{tc} minus the generator load P_{gen} over the speed N and the shaft inertia J. A step-up of P_{gen} from an equilibrium will cause the shaft speed to drop because $dN/dt < 0$, as demonstrated in Case-C2 of Figure 5.2.

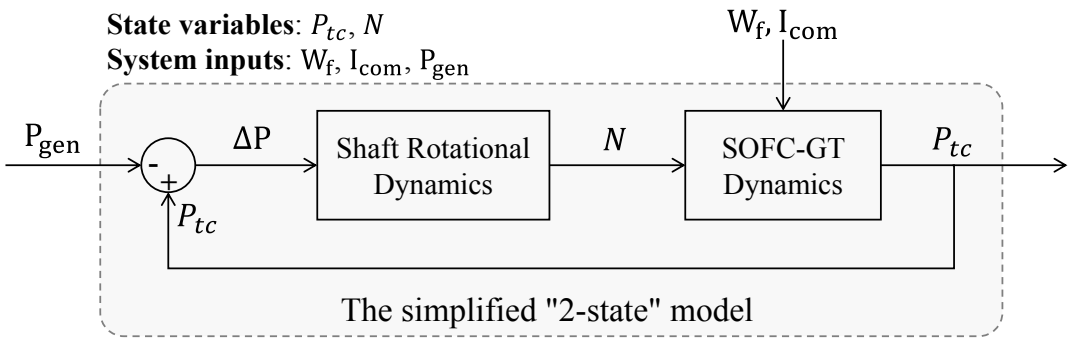

Figure 5.3: Schematic of the simplified "2-state" model for the SOFC/GT system.

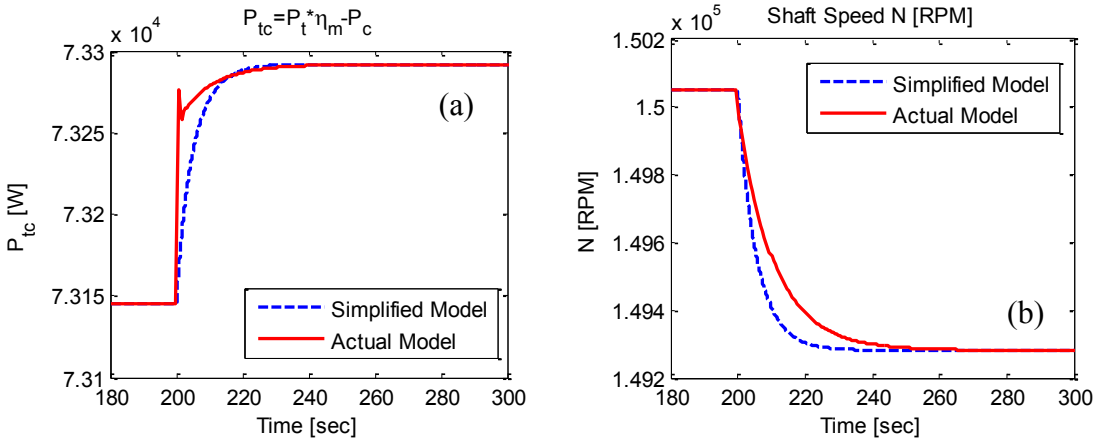

Figure 5.4: Validation of the simplified "2-state" model.

Given that the use of full-order model for analytic investigation of the stability is prohibitive due to its complexity, we attempt to develop a simplified equivalent model to capture the effects of P_{gen} on the shaft rotational dynamics. The equivalent schematic of the SOFC/GT system is given in Figure 5.3, where the shaft dynamics is separated from the SOFC and GT models. To capture the effects of P_{gen} input, we ignore the effects of W_f and I_{com} for the moment and approximate the dynamics from N to P_{tc} with first-order dynamics $1/(\tau s + 1)$. At steady state, as shown in Figure 5.5, the relation between N and P_{tc} can be approximated by the following second-order polynomial [15]:

$$P_{tc}^{SS} = P_{gen}^{SS} = aN^2 + bN + c. \tag{5.4}$$

Plugging the first-order dynamics for P_{tc} into Eqn. (5.4), the dynamic relationship between N and P_{tc} can be expressed as:

$$\frac{P_{tc}(s)}{P_{tc}^{SS}(s)} = \frac{1}{\tau s + 1} \implies \dot{P_{tc}} = \frac{(aN^2 + bN + c) - P_{tc}}{\tau}, \tag{5.5}$$

where τ is the time constant for the first-order dynamics.

Integrating Eqn. (5.3) and Eqn. (5.5), the equivalent second-order system, i.e., the "2-state" model (state variables: P_{tc} and N), can be expressed as:

$$\begin{bmatrix} \dot{P_{tc}} \\ \dot{N} \end{bmatrix} = \begin{bmatrix} (aN^2 + bN + c - P_{tc})/\tau \\ (P_{tc} - P_{gen})/(\alpha N J) \end{bmatrix}. \tag{5.6}$$

As shown in Figure 5.4, the simplified "2-state" model is able to capture the main dynamics of the full-order SOFC/GT system. In the following, the local BIBO stability around the equilibrium point $[P_{tc}^{SS}, N^{SS}]$ will be investigated through linearized analysis [71] of the nonlinear second-order system (i.e., the "2-state" model) shown in Eqn. (5.6).

The Jacobian matrix corresponding to point $[P_{tc}^{SS}, N^{SS}]$ is computed as:

$$A = \begin{bmatrix} -\frac{1}{\tau} & \frac{2aN^{SS} + b}{\tau} \\ \frac{1}{\alpha J N^{SS}} & -\frac{P_{tc}^{SS} - P_{gen}^{SS}}{\alpha J (N^{SS})^2} \end{bmatrix} = \begin{bmatrix} -\frac{1}{\tau} & \frac{2aN^{SS} + b}{\tau} \\ \frac{1}{\alpha J N^{SS}} & 0 \end{bmatrix}, \tag{5.7}$$

where $P_{tc}^{SS} = P_{gen}^{SS}$ is used, assuming steady state equilibrium.

The characteristic polynomial of the linearized system is given as:

$$\det(\lambda I - A) = \lambda^2 + \frac{1}{\tau}\lambda - \frac{2aN^{SS} + b}{\alpha J \tau N^{SS}}, \tag{5.8}$$

and the system is stable if and only if $2aN^{SS} + b < 0$.

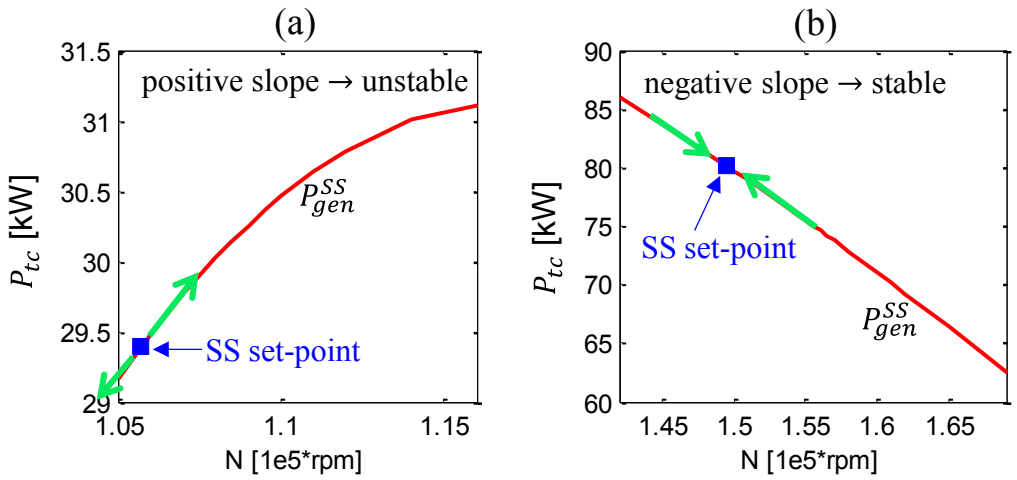

Figure 5.5: Steady-state generator power P_{gen}^{SS} expressed as a function of shaft speed N. The $N \sim P_{gen}^{SS}$ curve is calculated by using results of the original full-order model. The positive/negative slope leads to unstable/stable system operation, respectively.

Note that $\left(dP_{gen}^{SS}/dN\right)\big|_{N^{SS}} = 2aN^{SS} + b$, the stability depends on the slope of the $N \sim P_{gen}^{SS}$ curve, as shown in Figure 5.5. Therefore, we can conclude that:

$$The\ system\ is\ stable\ if\ and\ only\ if \left(\frac{dP_{gen}^{SS}}{dN}\right)_{N^{SS}} = 2aN^{SS} + b < 0. \qquad (5.9)$$

It should be noted that the slope-based stability criterion expressed in Eqn. (5.9) provides an approach to characterize the stable/unstable operating regions of the sprinter system. This has been verified through intensive numerical simulations in our study. For example, the stable and unstable steady-state operation regions for the case of I_{com}=2050 $A \cdot m^{-2}$ are presented in Figure 5.6. The S-SOFC/GT system is open-loop stable at high air (which is equivalent to high shaft speed) and high fuel flow region. Similar conclusion can be drawn for other values of I_{com}. For the same W_f input, the low airflow region has higher efficiency due to reduced cooling effect. However, this will reduce the stability margin, as shown in Figure 5.6. In order to achieve efficient and safe operation, feedback control, e.g., the shaft speed control expressed in Eqn. (5.2), should be used.

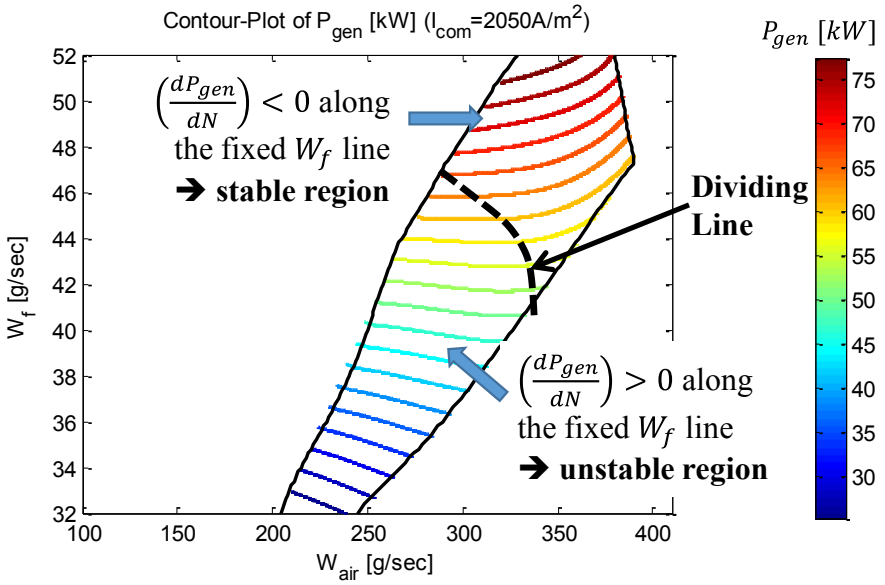

Figure 5.6: Characterization of the stable/unstable steady-state operation regions.

5.2 Transient Operation Analysis

5.2.1 Transient Operation Requirements

From the steady-state analysis in CHAPTER 4, it is known that the S-SOFC/GT system can operate the full range of net power within the system operating requirements. With the "optimal" operation line determined for steady-state, it is essential to develop an operating strategy to control the integrated system during transients in a way it returns to the operation line after load changes for fast and safe load following. The control strategy determines the way the system proceeds from one operating point to another.

A suitable control strategy for the normal operation of the proposed S-SOFC/GT system must meet the following requirements:

- **Safe operation of the system:** incidents that may cause damage or degradation to the SOFC or other components (see Section 4.4) must be avoided or mitigated. It should be noted that the safety margin between the optimal operation line and the safety region boundary (see Figure 4.20) indicates that safety issues are less likely to occur in the S-SOFC/GT system as compared with the R-SOFC/GT system.
- **Maintaining fairly constant SOFC operation condition:** fast changes in SOFC operation are often prohibited because a sudden large change can seriously impact

the cell and its service life due to thermal stresses [60]. It is also preferred to keep constant cell temperature to limit thermal fatigue and degradation [14]. In order to meet these special requirements for safe SOFC operation in the sprinter system, we limit the variation range and variation rate of T_{sofc}, P_{sofc} and I_{com}.

- **Fast load following:** the operating strategy should be able to follow a load profile quickly and accurately. The load profiles depend on the type of application [14]. In this chapter, step-wise load profiles will be used to evaluate the control strategy and quantify the transient capabilities of the S-SOFC/GT system.
- **High efficiency:** efficient operation should be ensured by the control strategy. In this chapter, this is achieved by the "optimal" feed-forward map through keeping the operation conditions in favorable regions.

5.2.2 Actuator Authority Evaluation

In order to gain insights on the system's operation and understand the interactions between actuators and various system parameters, we proceed in analyzing time-domain responses of various variables to actuator signal variations. In the following, the actuator authority is evaluated with respect to its effect on SOFC temperature T_{sofc}, SOFC power P_{sofc}, net power P_{net}, CB temperature T_{cb}, airflow rate W_{air}, and shaft speed N. The first three variables are selected because they are performance indicators for the SOFC and the entire system. The last three variables are also important because they dominate the load following performance and thermal safety management, as will be shown later.

Table 5.1shows the initial conditions used in the following open-loop simulations. This particular set-point, which is located at the high airflow region, is selected because it is open-loop stable. Note that we cannot performance open-loop analysis for the unstable set-points located at the low/medium airflow region and any attempt to apply step change would result in system shutdown, as demonstrated in Section 5.1. In addition, it should be noted that many operating points have been investigated in our study and similar results have been observed for the open-loop responses. Therefore, conclusions drawn from this particular example is expected to hold for general cases.

Table 5.1 Initial conditions for the open-loop simulations

Parameters	W_f	I_{com}	P_{gen}
Values	50.0 $[g \cdot sec^{-1}]$	1850 $[A \cdot m^{-2}]$	73.146 [kW]
Parameters	N	T_{sofc}	P_{net}
Values	1.5000e5 [RPM]	1004.0 [K]	155.760 [kW]

Given the nonlinear nature of the hybrid system, step responses from the actuators to aforementioned variables are investigated for both step-up and step-down directions, as shown in Figure 5.7 to Figure 5.9. The characteristics of the responses are summarized in Table 5.2. This table indicates whether the response of a variable exhibits overshoot (O) or undershoot (U) during a 0.5% step-up/step-down change in the corresponding actuator, whether the DC gain is positive or negative, and finally, whether the transfer function has a non-minimum phase (NMP) behavior. Those characteristic are explained below and the main conclusions are presented.

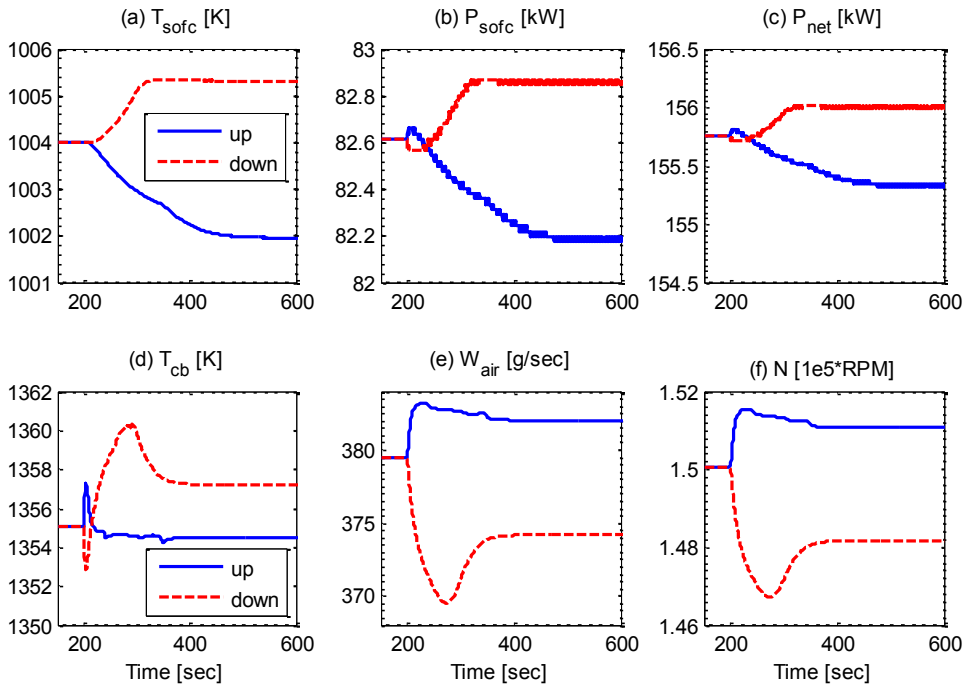

Figure 5.7: Time responses for 0.5% step-changes in fuel flow rate W_f.

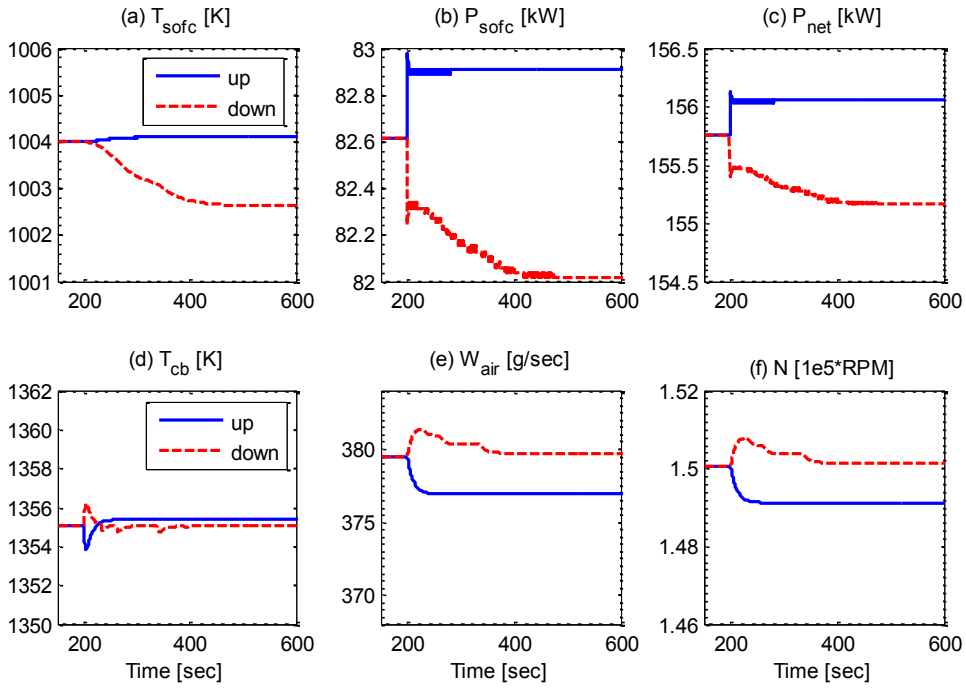

Figure 5.8: Time responses for 0.5% step-changes in current density I_{com}.

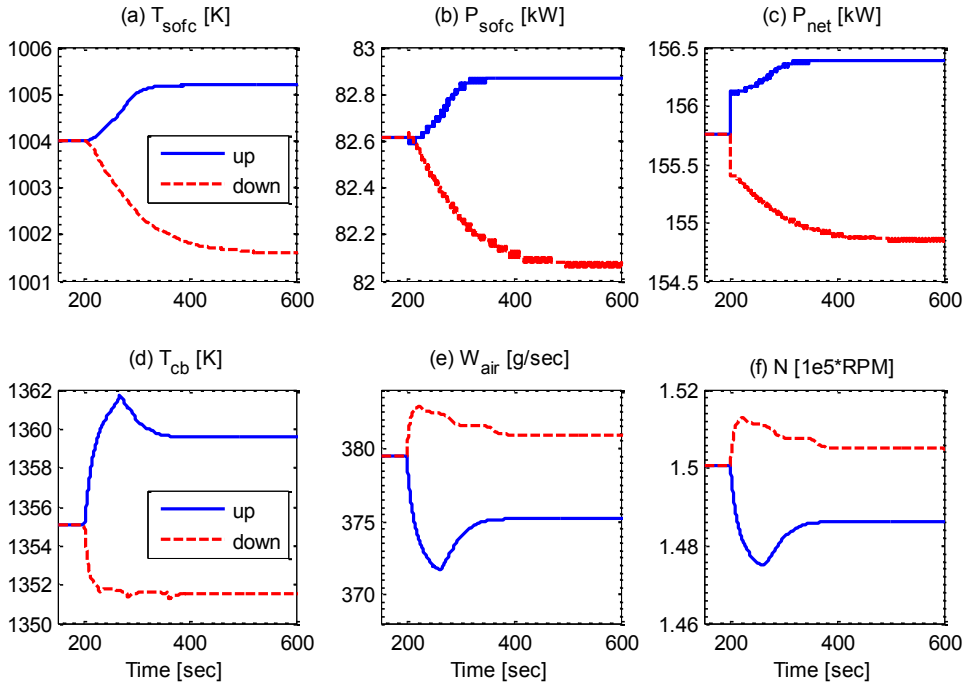

Figure 5.9: Time responses for 0.5% step-changes in generator power P_{gen}.

Table 5.2 Actuator authority table (open-loop responses of load step-up transients)

	T_{sofc}			P_{sofc}			P_{net}		
	O/U	DC	NMP	O/U	DC	NMP	O/U	DC	NMP
W_f	U	−	no	U	−	yes	U	−	yes
I_{com}	U	+	no	O	+	no	O	+	no
P_{gen}	U	+	no	U	+	yes	U	+	no
	T_{cb}			W_{air}			N		
	O/U	DC	NMP	O/U	DC	NMP	O/U	DC	NMP
W_f	U	−	yes	O	+	no	O	+	no
I_{com}	U	+	yes	U	−	no	U	−	no
P_{gen}	O	+	no	U	−	no	U	−	no

O/U: overshoot/undershoot. $+/-$: positive or negative DC gain. NMP: non-minimum phase

Effects of the W_f Actuator

As shown in Figure 5.7, with fixed I_{com} and P_{gen} inputs, a step increase in W_f will feed more fuel into the SOFC and more un-reacted fuel into the CB, which cause initially an increase in P_{sofc}, P_{net}, and T_{cb}. The increased CB temperature produces more turbine power and accelerates the shaft speed. In turn, higher speed allows for more air to cool down the SOFC. Consequently, P_{sofc} and P_{net} both decrease due to the cooling effect. T_{cb} also decreases as the cooling effect of the increased air supply exceeds the thermal energy released by the increased W_f input. Hence, the DC gain of T_{cb} with respect to W_f is slightly negative, as shown in Figure 5.7 (d).

The simulation results in Figure 5.7 reveal an important fact: the airflow W_{air}, which is strictly coupled with the shaft speed, dominates the system performance. In particular, without any feedback in place, P_{sofc} and P_{net} both decrease with respect to W_f. This is unexpected because P_{net} should, at least, be an increasing function of W_f. Therefore, proper airflow management, which can be achieved by shaft speed control through manipulating P_{gen} [14], is required for the S-SOFC/GT system.

Effects of the I_{com} Actuator

As shown in Figure 5.8, with fixed W_f and P_{gen} inputs, a step increase in I_{com} will cause initially a decrease in T_{cb} since less unused fuel will be burned in the CB. Hence, the shaft speed decelerates since less turbine power is produced. In turn, lower

speed allows for less air to be delivered into the SOFC stack, thereby increasing T_{sofc} slightly. For the step-down case, T_{sofc} decreases due to (1) the increased airflow and cooling effect and (2) less thermal energy released by the reactions in the SOFC.

Note that I_{com} has a strong control authority on P_{sofc}, as shown in Figure 5.8 (b). For example, substantial decrease of P_{sofc} with respect to I_{com} is observed in the step-down case. The reason comes in two-folds. First, less fuel is reacted in the SOFC due to the reduced I_{com} input. Second, T_{sofc} decreases due to increased airflow and cooling effect. Because of the high sensitivity of P_{sofc} to I_{com}, the use of I_{com} will be dictated by the need to maintain constant P_{sofc} for the S-SOFC/GT operation.

On the other hand, as shown in Figure 5.8 (d), I_{com} has a very limited control authority on T_{cb}. This is because the small change of I_{com} (note that very limited I_{com} variations are allowed in the S-SOFC/GT system) does not affect the amount of fuel reacted in the CB, which dominates T_{cb} and the turbine power. In addition, I_{com} also has limited control authorities on W_{air} and N, as shown in Figure 5.8 (e) and (f). This is because both W_{air} and N are dictated by the turbine power.

Effects of the P_{gen} Actuator

The generator power P_{gen} has strong effects on all the investigated variables because P_{gen} dominates the shaft speed and air supply. For example, a step increase in P_{gen} reduces the shaft power and decelerates the shaft speed. This decreases the air delivered to the SOFC, thereby causing less cooling effect. Consequently, the SOFC temperature T_{sofc}, burner temperature T_{cb}, SOFC power P_{sofc}, and net power P_{net} all increase, as shown in Figure 5.9. These simulation results emphasize the importance of airflow management for the S-SOFC/GT operation.

Conclusions and Control Implications

From the above analysis, main conclusions and control implications can be drawn for the proposed S-SOFC/GT system as follows. It should be noted that more insights on system operation and control implications will be derived in subsequent sections.

First, the shaft speed N and airflow W_{air} are strictly coupled and they dominate the S-SOFC/GT system performance, as shown in Figure 5.7 to Figure 5.9. In particular, as shown in Table 5.2, W_{air} and N have the same DC gains, which are directly opposite to the those for T_{sofc}, T_{cb}, P_{sofc} and P_{net}. In addition, for the unstable set-points, changes in actuator inputs will cause system shutdown when there is no feedback control in place. Therefore, active shaft speed control and air-flow management are crucial for successful functioning of the proposed S-SOFC/GT system.

Second, the current density input I_{com} has limited effect on N and W_{air}, as shown in Figure 5.8. However, it has a very strong control authority on P_{sofc} by regulating the amount of fuel reacted in the SOFC. In addition, I_{com} should be changed slowly in the S-SOFC/GT system for safe operation of the fuel cell, as discussed in CHAPTER 4. Hence, I_{com} is mainly used to regulate the SOFC power in the following control design.

Third, the fuel flow W_f and generator power P_{gen} have strong control authorities on N and W_{air}. This is because that the shaft rotational dynamics is governed by the GT power and the generator load, as shown in Eqn. (5.3). The GT power is dictated by the amount of fuel burned in CB, which depends critically on the W_f input.

Therefore, the control task for the S-SOFC/GT system is essentially to coordinate the system inputs, especially W_f and P_{gen} (note that small/slow I_{com}variations are used to control P_{sofc}), in an appropriate way to achieve fast and safe load following.

5.2.3 System Analysis and Operation Challenges

The S-SOFC/GT system investigated herein is a so-called multiple input multiple output (MIMO) system. We check if the system can be decoupled and perform Relative Gain Array (RGA) analysis [81], [83] to understand the dependencies between different variables. Next, we identify the input and output variables for the RGA analysis.

Input and Output Variables

The input variables to the hybrid system are fuel flow W_f, SOFC current density I_{com}, and the generator power P_{gen}. Note that other variable sets can also be used, such as the SOFC power P_{sofc} instead of I_{com}. To perform RGA analysis, the system should be stable under all input-output pairings, which is not the case if P_{gen} is used as an input, as

demonstrated in Section 5.1. In the following, W_{air} is used to substitute P_{gen} as an input for the RGA analysis because W_{air} is strictly coupled with P_{gen} [14].

Outputs are system variables to be varied in a certain desired manner. The system has only one output variable relevant for the user, i.e., the net power P_{net} [14]. However, fairly constant SOFC power and cell temperature need to be maintained during transients. Therefore, T_{sofc} and P_{sofc} are regarded as system outputs. Note that other variables such as the CB temperature T_{cb} and shaft speed N can also be regarded as outputs.

The input and output variables used in the following analysis are:

$$u = [W_{air} \quad W_f \quad I_{com}]^T, \tag{5.10}$$

$$y = [T_{sofc} \quad P_{sofc} \quad P_{net}]^T. \tag{5.11}$$

RGA Analysis and Input/Output Dependencies

In general, the MIMO system requires multiple control loops and the system can be complicated through loop interactions that result in variables with unexpected effects. Decoupling the variables will simplify the control design and improve the performance. RGA is a useful tool for the control design and analysis of MIMO systems that could be decoupled [83]. In particular, it provides a quantitative way to analyze the input-output interactions and pairings. For system that cannot be decoupled, MPC and neural networks [82] are better choices than RGA [83].

We determine if the system can be decoupled and perform RGA analysis based on the steady-state gain matrix [83], which is defined as follows:

$$G = \begin{bmatrix} g_{11} & \cdots & g_{1n} \\ \vdots & \ddots & \vdots \\ g_{n1} & \cdots & g_{nn} \end{bmatrix} \; with \; g_{ij} = \frac{\partial y_i}{\partial u_j}, \tag{5.12}$$

where g_{ij} is the steady-state partial derivative of system output y_i with respect to input u_j. Beware that a RGA has to have the same number of controlled variables and manipulated variables. Therefore, the gain matrix G in Eqn. (5.12) should be a square matrix.

Given the steady-state gain matrix G, we can determine whether the system can be decoupled as follows. We perform singular value decomposition (SVD) on G and find the condition number (CN), which is defined to be the ratio of the maximum to the minimum eigenvalues of the SVD. The rule of thumb is that the system is too hard to decouple if the condition number CN is greater than 50, as discussed in [83].

Given the gain matrix G, the RGA can be computed as follows:

$$RGA = [\lambda_{ij}]_{n\times n} = G.* (G^{-1})^T, \tag{5.13}$$

where element-wise multiplication instead of normal matrix multiplication is used.

Table 5.3 Singular value decomposition results for different load cases

Load [kW]	Steady-state gain matrix	SVD eigenvalues	Condition number	Can be decoupled?
118.7 (low load)	$\begin{bmatrix} -0.6321 & -1.1944 & -0.9065 \\ 0.9529 & 1.6592 & 2.1019 \\ -0.6492 & -0.9380 & -1.3460 \end{bmatrix}$	3.7003 0.3778 0.0695	53.2652	No
146.5 (medium load)	$\begin{bmatrix} -0.5810 & -0.7630 & -0.6600 \\ 0.5573 & 0.7966 & 1.5048 \\ -0.4332 & 0.2846 & -0.3409 \end{bmatrix}$	2.1217 0.5679 0.3541	6.0000	Yes
167.1 (high load)	$\begin{bmatrix} -0.5179 & -0.5523 & -0.7388 \\ 0.4660 & 0.5584 & 1.2823 \\ -0.2554 & 0.5231 & -0.1957 \end{bmatrix}$	1.7985 0.6207 0.2231	8.0610	Yes

Based on the steady-state simulation results in CHAPTER 4, we can calculate the steady-state gain matrix, the condition number CN and the RGA. The results for different load cases are shown in Table 5.3 to Table 5.5. Note that the system is hard to decouple at low load case because CN is too large. One explanation is that the S-SOFC/GT system is operated at recuperation mode at low load conditions. In this case, it can be regarded as an R-SOFC/GT system, in which the SOFC is the primary power source and the system depends on the closed mechanical/thermal couplings to achieve high efficiency [7]. Thus, RGA analysis is only performed for medium and high load cases in this section and the results are presented in Table 5.4 and Table 5.5, where each row of the RGA represents one of the outputs and each column represents a manipulated variable [83].

Table 5.4 RGA analysis at medium load

P_{net}=146.5 kW	W_{air}	W_f	I_{com}
T_{sofc}	**0.9531**	0.8261	-0.7791
P_{sofc}	-0.5852	-0.1640	**1.7491**
P_{net}	0.6321	**0.3379**	0.0300

Table 5.5 RGA analysis at high load

P_{net}=167.1 kW	W_{air}	W_f	I_{com}
T_{sofc}	**1.6221**	0.5240	-1.1461
P_{sofc}	-0.9253	-0.1957	**2.1211**
P_{net}	0.3032	**0.6718**	0.0250

Table 5.6 General guideline for the RGA analysis [83]

λ_{ij}	Interpretation	Possible pairing
$\lambda_{ij} = 0$	Input m_j has no effect on output y_i	Avoid m_j~y_i pair
$\lambda_{ij} = 1$	m_j affects y_i w/o any interaction from other loops	Pair m_j with y_i
$\lambda_{ij} < 0$	System will be unstable whenever m_j is paired with y_i	Avoid m_j~y_i pair
$\lambda_{ij} \in (0, 0.5)$	Effects from other loops are greater than the m_j~y_i pair	Avoid m_j~y_i pair
$\lambda_{ij} \in (0.5, 1)$	The m_j~y_i pair has greater influence than other loops	Pair m_j with y_i
$\lambda_{ij} > 1$	The m_j~y_i pair dominates the system, but other loops are still affecting the control pair in the opposite direction	Pair m_j with y_i

Table 5.6 presents the guidelines in understanding and analyzing the RGA. The soliciting input/output pairings are marked bold in Table 5.4 and Table 5.5. In the sequel, we list the remarks and control implications that can be derived from the RGA analysis. Note that some of those implications are similar to those in Section 5.2.2.

- The airflow W_{air} should be used to control the SOFC temperature T_{sofc}. Note that the RGA value $\lambda_{11} > 1$ at high load, which indicates that the control pair is dominant in the system while other loops are still affecting the pair in the opposite direction.
- The fuel flow input W_f should be used to control P_{net}. Note that $P_{sofc} \approx 1.8 * P_{gen}$ in the medium load case. W_{air} has a dominant effect on P_{sofc} because it dictates T_{sofc}. Hence, we have $\lambda_{31} > \lambda_{32}$ in Table 5.4, i.e., W_{air} has greater effect on P_{net} than W_f in the medium load case. However, this is achieved by changing T_{sofc} and P_{sofc}, both of which should be kept constant in the sprinter system. Hence, we use W_f to control

P_{net} because W_f determines the amount of fuel burned in the CB, which dictates the GT-generator power and net power P_{net} in the S-SOFC/GT system.

- The current density I_{com} should be used to control the SOFC power P_{sofc} because it determines the amount of fuel reacted through electro-chemical reaction in the SOFC. It should be noted that I_{com} has very little effect on P_{net} since $\lambda_{33} \approx 0$.
- There are strong interactions between the control loops for the SOFC temperature and net power. For example, W_{air} that is used to control T_{sofc} has a strong effect on P_{net} because the change of W_{air} will affect T_{cb} and thus the GT-generator power and net power significantly due to the strong cooling effect of the air. In addition, W_f that is used to control P_{net} will also affect T_{sofc}, especially for the high load case, as shown in Table 5.5. These interactions are inevitable because they are caused by the closed mechanical/thermal couplings of the SOFC/GT system, as shown in Figure 1.2.

Special Transient Operation Challenges for the S-SOFC/GT System

In the conventional R-SOFC/GT system, load following is mainly achieved by the SOFC while the GT-generator has very limited effect since P_{gen} only contributes to about 20% of system net power. In fact, P_{gen} is primarily used to regulate the airflow for SOFC thermal safety management rather than load following purposes [14]. Hence, fast change of P_{gen} is prohibited in the R-SOFC/GT system for thermal safety considerations. Hence, the most commonly used control strategy for the R-SOFC/GT system is to achieve rapid load following by the SOFC stack and use P_{gen} to regulate the airflow for thermal safety management, as demonstrated in [14], [45] - [47], [49] - [52], [62].

However, the aforementioned operating strategies developed for the R-SOFC/GT system do not apply to the S-SOFC/GT system. The reason is that both the load following and thermal management are dominated by the GT-generator in the S-SOFC/GT system while the SOFC stack that is operated at constant temperature only provides the baseline power. Hence, fast load following requires rapid change of GT-generator power, which will in turn affect the SOFC air supply and cell temperature due to the closed couplings in the hybrid SOFC/GT system. Hence, it is very challenging to achieve fast load following while keeping constant cell temperature in the proposed S-SOFC/GT system.

5.3 Feedback Control Design

In this section, transient operation strategy and control algorithms that can achieve fast and safe load following will be developed for the proposed S-SOFC/GT system. Both load step-up and load step-down transients will be investigated. We will also quantify the transient capabilities of the S-SOFC/GT system and compare it against the conventional R-SOFC/GT system.

5.3.1 System Control Layout

Due to the complexity and nonlinear behavior of the integrated SOFC/GT system [14], full state feedback controllers [81], [82] that require state observers will not be used here. Instead, based on our analysis in Section 5.2, a cascade feedforward-feedback (FF-FB) type control strategy is designed for the S-SOFC/GT system.

The schematic of the system control layout is shown in Figure 5.10. The proposed control strategy consists of three sub-controllers, namely, shaft speed controller, fuel flow controller, and current density controller. Schematics of these controllers are presented in Figure 5.11 to Figure 5.14. There are three feedback signals used in the proposed control, namely, shaft speed N, CB temperature T_{cb}, and net power P_{net}. These feedback signals can either be measured or calculated based on other measured signals, as summarized in Table 5.7. For example, the SOFC power P_{sofc} can be calculated from the measured cell voltage U_{sofc} and the I_{com} input. Therefore, observer design is not required.

Table 5.7 Measured and calculated signals for feedback control

Feedback signal	Note (measurement or calculation)
Shaft speed N	Measured by the speed sensor installed on the GT-generator
CB temperature T_{cb}	Measured by a thermocouple installed on the CB
Cell voltage U_{sofc}	Measured by a voltage sensor
SOFC power P_{sofc}	$P_{sofc} = kU_{sofc}I_{com}$ where k is constant coef. for the SOFC stack
Net power P_{net}	$P_{net} = P_{sofc} + P_{gen}$

Before we proceed further, we can create some look-up table (LUT) functions to represent the static feedforward map shown in Figure 4.21. In particular, we can use the LUT function to express the one-to-one relation between any two variables in the vector

$(W_f, I_{com}, P_{gen}, N, T_{cb}, P_{net})$. For example, the function $W_f{}^{LUT}(T_{cb})$ denote the fuel flow corresponding to T_{cb} while $N^{LUT}(P_{net})$ represents the shaft speed corresponding to P_{net}. The proposed control strategy uses many LUTs, as shown in Figure 5.11 to Figure 5.14.

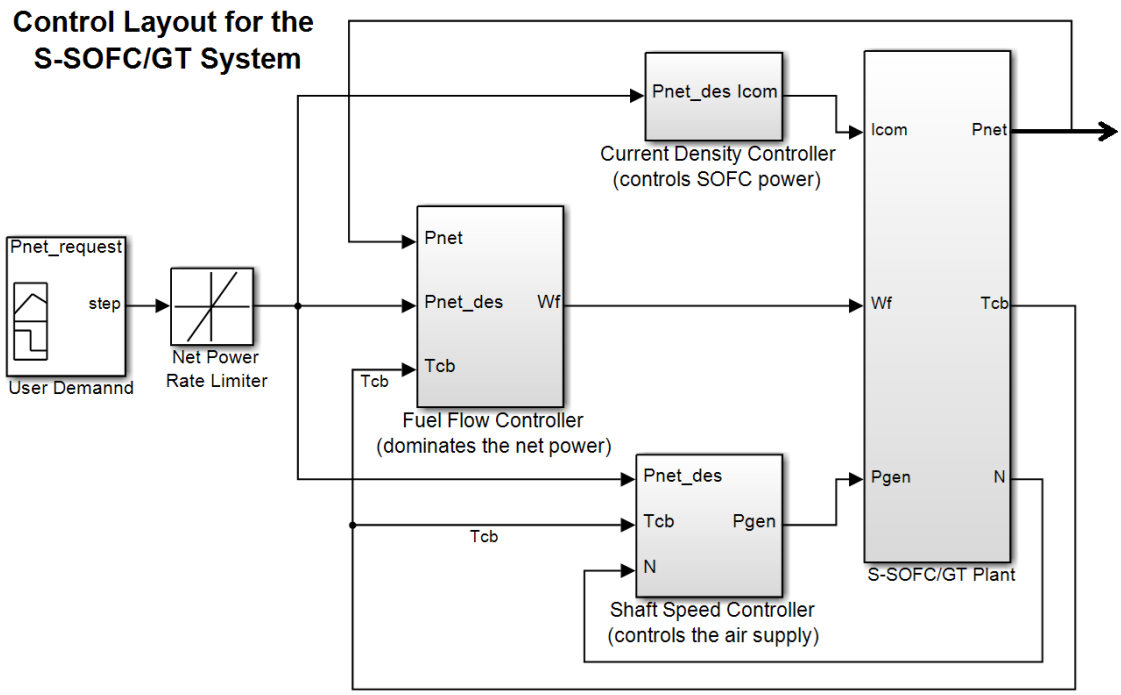

Figure 5.10: Schematic of the control layout for the S-SOFC/GT system. The shaft speed controller is designed to regulate the SOFC airflow for thermal management. The fuel flow controller is used to regulate the fuel supply to control the CB temperature which dominates the GT-generator power and net power for fast load following. The feed-forward current density controller is used to regulate I_{com} for safe SOFC operations. The intermediate variable T_{cb} is used to coordinate the air and fuel flows to achieve fast load following while enforcing SOFC thermal safety management.

In the following, we present design considerations for each sub-controller and the techniques used to handle the interactions between different control loops. In particular, as shown in Section 5.2, a critical challenge for the S-SOFC/GT system control design is to handle the strong interactions between load following (P_{net}) and SOFC thermal (T_{sofc}) management, which are caused by the strong thermal/mechanical couplings of the system. This problem is addressed as follows. As shown in Figure 5.10, based on the feedforward map (Figure 4.21), we coordinate the shaft speed controller (which dictates the air supply)

with the fuel flow controller through the intermediate feedback variable T_{cb}. The burner temperature T_{cb} is chosen because it dominates the net power. Meanwhile, it also has a significant effect on T_{sofc} because T_{cb} affects the SOFC inlet air temperature through the HEX. Further analysis on this subject will be given in the following once we elucidate the objectives, feedback signals and design considerations of those sub-controllers.

5.3.1.1 Shaft Speed Controller

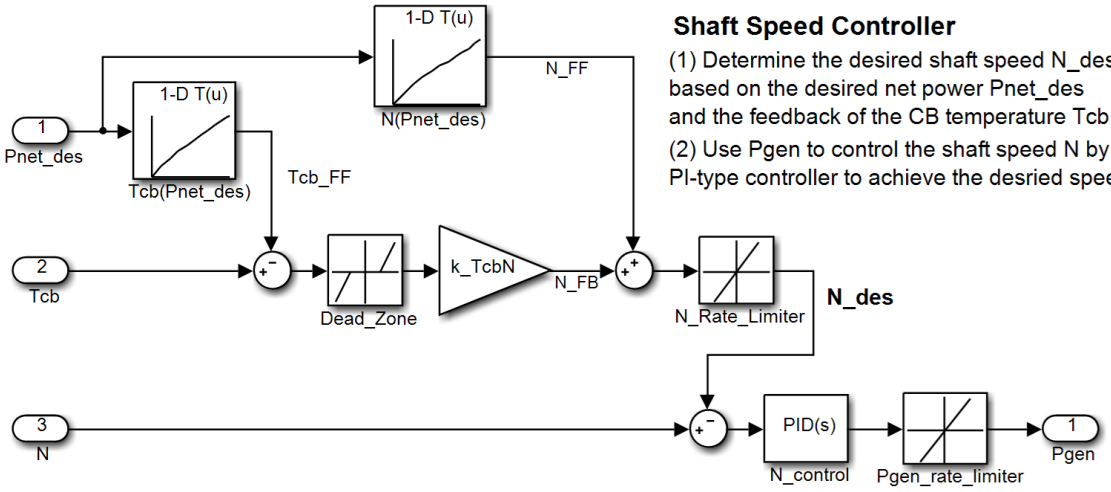

Figure 5.11: Schematic of the shaft speed controller.

The shaft speed controller can be used to stabilize the system at the desired shaft speed N_{des} by controlling P_{gen} for steady-state operations, as shown in Section 5.1. In the transient operations, the shaft speed controller is mainly used to regulate the airflow W_{air} for thermal management. As shown in Figure 5.11, the shaft speed controller is:

$$P_{gen}(s) = \left(k_{N,P} + \frac{k_{N,I}}{s}\right)(N(s) - N_{des}(s)), \tag{5.14}$$

where $k_{N,P}$ and $k_{N,I}$ are the proportional and integral controller gains, respectively; N_{des} is the desired shaft speed which can be determined based on T_{cb} as follows:

$$N_{des} = N^{LUT}\left(P_{net}^{des}\right) + k_{T_{cb}N}\left(T_{cb} - T_{cb}^{LUT}\left(P_{net}^{des}\right)\right), \tag{5.15}$$

where $k_{T_{cb}N}$ is a constant coefficient whose value (see Table 5.9) can be calculated as the slope of N over T_{cb} in the feedforward map.

The reason of using T_{cb} feedback to determine N_{des} in Eqn. (5.15) is explained as follows. As shown in Figure 5.12, during load step-up and step-down transients, the CB temperature T_{cb} usually exhibits responses similar to that of a first-order system. In order to enforce SOFC thermal safety management, the shaft speed that dominates the airflow should be controlled to match the CB temperature, which will in turn affect T_{sofc} though the HEX thermal feedback. Otherwise, T_{sofc} will increase/decrease if the shaft speed and the airflow supply are larger/smaller than their desired values. Therefore, by using the T_{cb} feedback expressed in Eqn. (5.15), which is further explained in Figure 5.12, coordinated load following and thermal management of the S-SOFC/GT can be achieved.

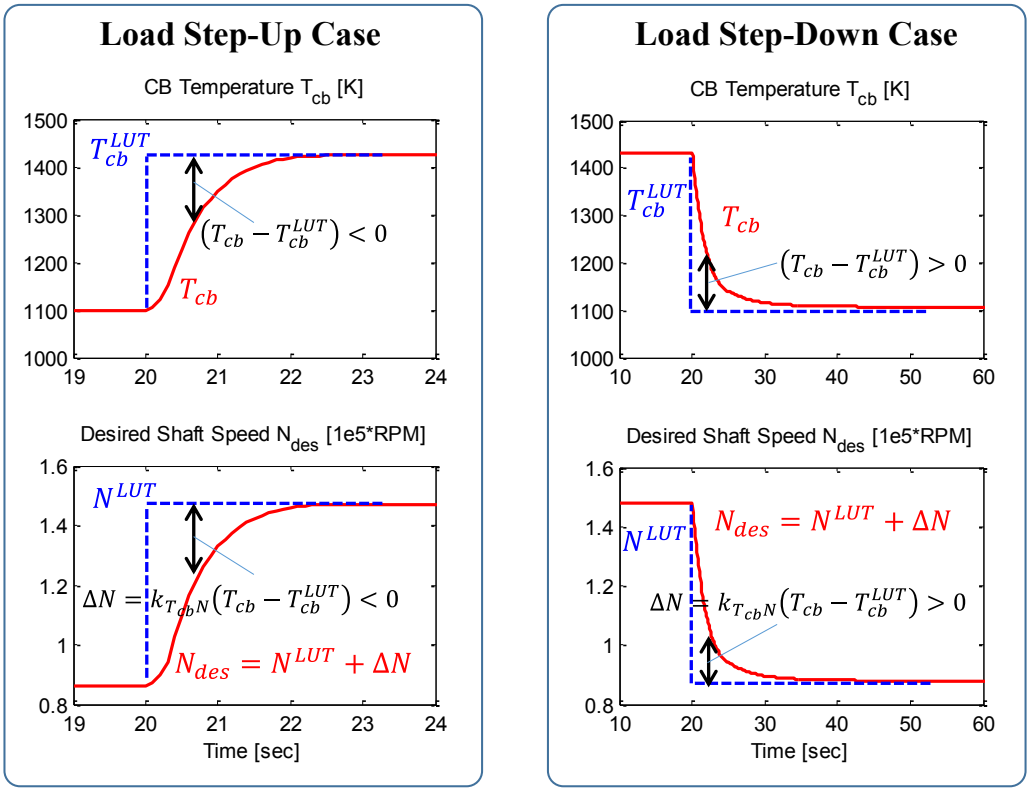

Figure 5.12: Determine the desired shaft speed based on the T_{cb} feedback signal. This helps to coordinate the air and fuel flows for fast load following and thermal safety.

If the feedback term in Eqn. (5.15) is not used, rapid increase/decrease of the shaft speed will lead to undesired results. For example, fast decrease of P_{gen} or even motoring mode operation is required to quickly accelerate the shaft speed for load step-up transient, thereby resulting in a considerable power tracking error. This will also affect the thermal safety because of the rapid increase of air supply. For the load step-down case, a rapid decrease of shaft speed will cause dangerous compressor surge [84] or backflow of gas from the CB to the SOFC anode channel and reversal of electro-chemical reactions [14]. These incidents must not occur in any operation circumstance. Therefore, a rate limiter is applied on N_{des} in order to achieve safe operations, as shown in Figure 5.11. Note that a rate limiter is also applied on the generator to avoid over-ambitious change of P_{gen}.

Once the integrated system approaches steady-state, i.e., the absolute value of the T_{cb} feedback term in Eqn. (5.15) is below a predefined threshold T_{cb}^{DZ}, it is desirable to fix the shaft speed and the air supply because any change of N or W_{air} will in turn affect T_{cb}. To this end, a dead-zone block is used in the shaft speed controller shown in Figure 5.11. This helps to improve the system responses.

5.3.1.2 Fuel Flow Controller

The schematic of the fuel flow controller is shown in Figure 5.13. There are three inputs to the controller: the desired net power P_{net}^{des}, the feedback signals of P_{net} and T_{cb}. The fuel flow controller is used to control the fuel supply to the system in order to reach the desired CB temperature T_{cb}^{des} quickly for fast load following because T_{cb} dominates the GT-generator power and system net power. The fuel flow controller is realized in two steps, as shown in Figure 5.13.

First, we determine the desired CB temperature T_{cb}^{des} according to the net power demand P_{net}^{des} and the actual power output P_{net}. In particular, T_{cb}^{des} is expressed as:

$$\begin{aligned} T_{cb}^{des} &= T_{cb}^{LUT}\left(P_{net}^{des}\right) + \frac{P_{net}^{des} - P_{net}}{P_{net}^{des}} T_{cb}^{LUT}\left(P_{net}^{des}\right) \\ &= \frac{2P_{net}^{des} - P_{net}}{P_{net}^{des}} T_{cb}^{LUT}\left(P_{net}^{des}\right). \end{aligned} \tag{5.16}$$

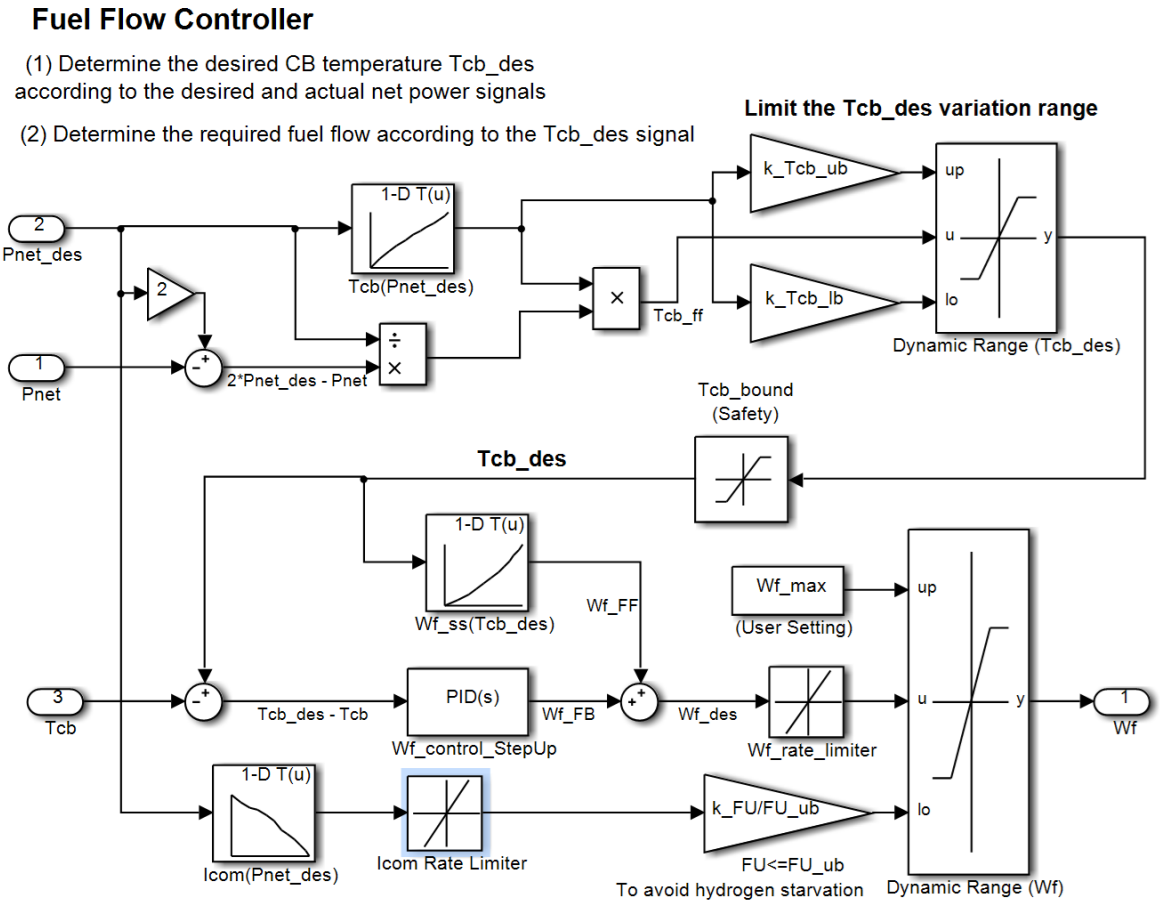

Figure 5.13: Schematic of the fuel flow controller.

Therefore, the T_{cb}^{des} formula expressed in Eqn. (5.16) helps to facilitate the system power response by using the P_{net} feedback signal. It should be noted that T_{cb}^{des} should be controlled to keep a limited distance away from the feedforward value $T_{cb}^{LUT}\left(P_{net}^{des}\right)$. This is because over-adjustment of T_{cb} will affect the SOFC temperature. Therefore, as shown in Figure 5.13, a dynamic range block is used to limit the T_{cb}^{des} output of Eqn. (5.16). In addition, a saturation block is applied to keep T_{cb}^{des} within the safety range.

Second, we determine the required fuel flow (W_f) according to T_{cb}^{des} identified by Eqn. (5.16) in the first step. To this end, a FF-FB type controller is developed, as shown in Figure 5.13. The controller can be expressed as follows:

$$W_f(s) = W_f^{LUT}\left(T_{cb}^{des}\right) + \left(k_{W_{f,P}} + \frac{K_{W_{f,I}}}{s}\right)\left(T_{cb}^{des} - T_{cb}\right), \tag{5.17}$$

where $k_{W_{f,P}}$, $K_{W_{f,I}}$ are the proportional and integral controller gains, respectively.

As shown in Figure 5.13, a rate limiter is used for W_f to account for the fact that infinite rate of change in fuel flow is not possible. In addition, a dynamic range block is applied to keep the W_f command within a valid region. W_f is bounded from above by the maximum allowable fuel flow W_f^{max}. In order to avoid hydrogen starvation, the lower bound for W_f is calculated based on the net power demand P_{net}^{des} as follows:

$$W_f^{min} = \frac{k_{FU}}{FU_{UB}} \cdot I_{com}^{FF} = \frac{k_{FU}}{FU_{UB}} \cdot I_{com}^{LUT}\left(P_{net}^{des}\right), \tag{5.18}$$

where k_{FU} is a constant coefficient of the SOFC stack; FU_{UB} is the maximum allowable SOFC FU ratio to avoid fuel (hydrogen) starvation [14].

5.3.1.3 Current Density Controller

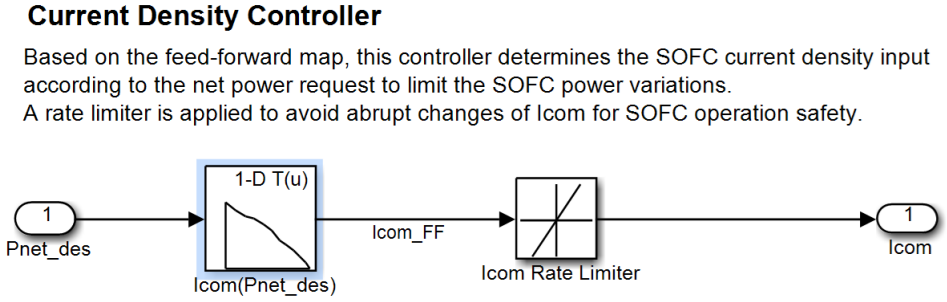

Figure 5.14: Schematic of the current denstiy controller.

The schematic of the current density controller is presented in Figure 5.14. Recall that only small and slow I_{com} variations are allowed in the proposed S-SOFC/GT system. Therefore, I_{com} is determined by the feed-forward command as follows:

$$I_{com} = I_{com}^{LUT}\left(P_{net}^{des}\right). \tag{5.19}$$

Table 5.8 Limiters used in the proposed control strategy

Parameter	Value	Note
System net power (user demand)		
Pnet_rate_ub	150 $[kW \cdot sec^{-1}]$	Rate limiter (UB) for P_{net} user-demand
Pnet_rate_lb	-150 $[kW \cdot sec^{-1}]$	Rate limiter (LB) for P_{net} user-demand
Shaft speed controller (Figure 5.11)		
N_rate_ub	1.25e4 $[RPM \cdot sec^{-1}]$	Rate limiter (UB) for N_{des}
N_rate_lb	-6.25e3 $[RPM \cdot sec^{-1}]$	To avoid gas backflow or comp. surge
Pgen_rate_ub	400 $[kW \cdot sec^{-1}]$	Generator power rate limiter (UB)
Pgen_rate_lb	-400 $[kW \cdot sec^{-1}]$	Generator power rate limiter (LB)
Fuel flow controller (Figure 5.13)		
k_Tcb_ub	1.005 [-]	Dynamic range limiter (UB) for T_{cb}^{des}
k_Tcb_lb	0.995 [-]	Dynamic range limiter (LB) for T_{cb}^{des}
Tcb_des_ub	1480 $[K]$	Safety bound (UB) for T_{cb}^{des}
Tcb_des_lb	1000 $[K]$	Safety bound (LB) for T_{cb}^{des}
Wf_rate_ub	300 $[g \cdot sec^{-1}]$	Fuel flow rate limiter (UB)
Wf_rate_lb	-300 $[g \cdot sec^{-1}]$	Fuel flow rate limiter (LB)
Wf_max	85.0 $[g \cdot sec^{-1}]$	Maximum fuel flow rate
Current density controller (Figure 5.14)		
Icom_rate_ub	200 $[A \cdot m^{-2} sec^{-1}]$	I_{com} rate limiter (UB) for safe operation
Icom_rate_lb	-200 $[A \cdot m^{-2} sec^{-1}]$	I_{com} rate limiter (LB) for safe operation

Table 5.9 Designed controller constants

Parameter	Value	Note
Shaft speed controller (Figure 5.11)		
k_{TcbN}	188.13 $[RPM \cdot K^{-1}]$	Constant coefficient to calculate N_{des}
T_{cb}^{DZ}	2.5 $[K]$	Dead-zone threshold for T_{cb} feedback
$k_{N,P}$	2e-2 $[kW \cdot RPM^{-1}]$	Shaft speed controller proportional gain
$k_{N,I}$	4e-2 $[kW \cdot RPM^{-1}]$	Shaft speed controller integral gain
Fuel flow controller (Figure 5.13)		
k_{FU}	1.31e-2 $[m^2 \cdot g \cdot s^{-1} A^{-1}]$	Coef. for W_f^{min} to avoid H_2 starvation
FU_{UB}	0.92 [-]	The maximum allowable FU ratio
$k_{W_f,P}$	0.15 $[g \cdot sec^{-1} K^{-1}]$	Fuel flow controller proportional gain
$k_{W_f,I}$	2e-3 $[g \cdot sec^{-1} K^{-1}]$	Fuel flow controller integral gain

Table 5.8 summarizes the range and rate limiters used in our control strategy. The limiter applied on the requested net power is because that a large step change of the net power demand is impractical and will cause numerical issues in our Simulink model. A

lower rate limiter is applied on the shaft speed to avoid backflow of gas from the CB to the SOFC and the dangerous compressor surge during load step-down operation. Limiters for the fuel flow controller are explained in Section 5.3.1.2. In addition, a rate limiter is applied on I_{com} (see Figure 5.14) to limit I_{com} variation for safe SOFC operations.

The designed controller constants are summarized in Table 5.9. It should be noted that the proposed cascade FF-FB control strategy relies on the feedforward map (i.e., the LUTs in Figure 5.11 to Figure 5.14) to achieve high system efficiency.

5.3.2 Simulated Transient Responses

In this section, the proposed cascade controller is investigated through numerical simulations for both load step-up and load step-down transients. In order to evaluate the effectiveness of the control strategy over the entire load range, the load step-up transient from P_{base} to P_{peak} and the load step-down transient from P_{peak} to P_{base} are investigated in this section. Load transients for other power levels are evaluated in Section 5.3.4.

5.3.2.1 Load Step-Up Transient Responses

The simulation results for load step-up operation from P_{base} to P_{peak} are given in Figure 5.15 to Figure 5.18. In particular, system inputs and the SOFC FU ratio are given in Figure 5.15 while the SOFC thermal transients are shown in Figure 5.16. The power responses are shown in Figure 5.17 while other variables are shown in Figure 5.18.

During the load step-up transient, a significant amount of fuel W_f is supplied into the system, which helps to increase the CB temperature T_{cb} and the turbine power P_{turb} rapidly for fast load following, as shown in Figure 5.15 and Figure 5.17. Consequently, more generator power P_{gen} and net power P_{net} can be produced very quickly to meet the desired net power demand, as shown in Figure 5.17. We see that the power settling time is about 5 seconds for a load step-up operation from P_{base} to P_{peak}.

As shown in Figure 5.18 (c), a considerable amount of turbine power is used to accelerate the shaft speed. This part of energy will be stored in the form of kinetic energy in the shaft. Therefore, some obvious shortages of net power output are resulted during the short period of power transient. In practice, this deficit power can be provided by a

battery or capacitor pack. Let ΔP_{net} and ΔP_{net}^{norm} denote the actual and normalized power tracking error, respectively. They can be computed as follows:

$$\Delta P_{net} = P_{net} - P_{net}^{des}, \qquad \Delta P_{net}^{norm} = 1 - P_{net}/P_{net}^{des}. \tag{5.20}$$

As shown in Figure 5.18 (d), the maximum absolute values for ΔP_{net} and ΔP_{net}^{norm} during the power transient are 66.9KW and 39.1%, respectively.

The current density I_{com} varies slowly in a limited range in order to achieve safe SOFC operation. Note that the SOFC power P_{sofc} increases by about 10kW in the short period of power transient, as shown in Figure 5.17. This is due to the quick burst of fuel supply shown in Figure 5.15, which elevates the voltage U_{sofc} because of the increased species concentrations, as shown in the Nernst equation in Eqn. (2.2).

Meanwhile, the proposed controller also accelerates the shaft speed and delivers more airflow W_{air} to match the increased T_{cb} to limit the SOFC temperature variations. As shown in Figure 5.18, the proposed controller achieves very good performance in SOFC thermal management. In particular, the difference between the actual T_{sofc} and the setting-value T_{SET} is limited in $\pm 2K$ while the T_{sofc} changing rate (the absolute value) is less than 5 $K \cdot min^{-1}$, as shown in Figure 5.16 (a) and (b), respectively. T_{sofc} takes about 380 seconds to settle, this is much faster than the R-SOFC/GT system (see Figure 5.23).

Table 5.10 summarizes the performance of the proposed controller during a load step-up transient from the baseline power to the peak power in the S-SOFC/GT system.

Table 5.10 Summary of the load step-up operation

Performance metric parameters	Units	Value
The 2% net power settling time $T_s(P_{net})$	$[sec]$	5.3
The maximum (absolute value) of ΔP_{net}	$[kW]$	66.9
The maximum (absolute) value of ΔP_{net}^{norm}	[%]	39.1
SOFC temperature settling time $T_s(T_{sofc})$	$[sec]$	~380
Maximum (absolute value) T_{sofc} rate	$[K \cdot min^{-1}]$	~4.1

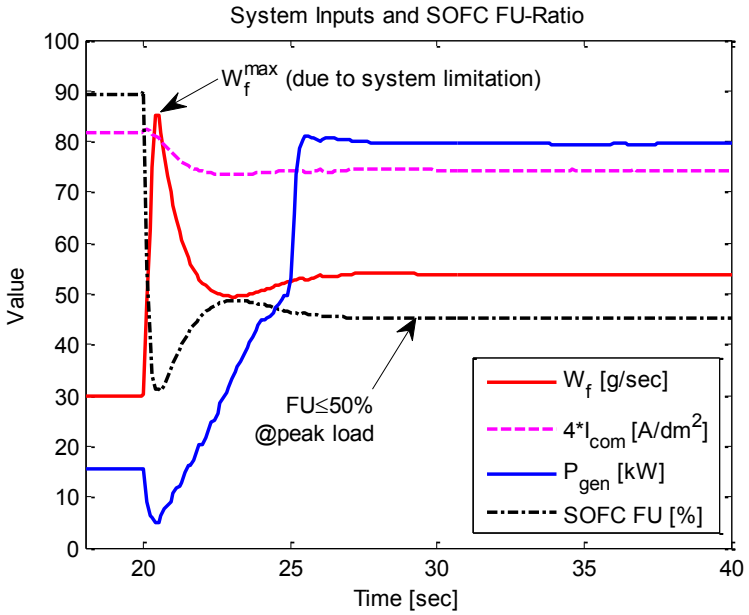

Figure 5.15: System inputs and SOFC FU ratio during load step-up operation.

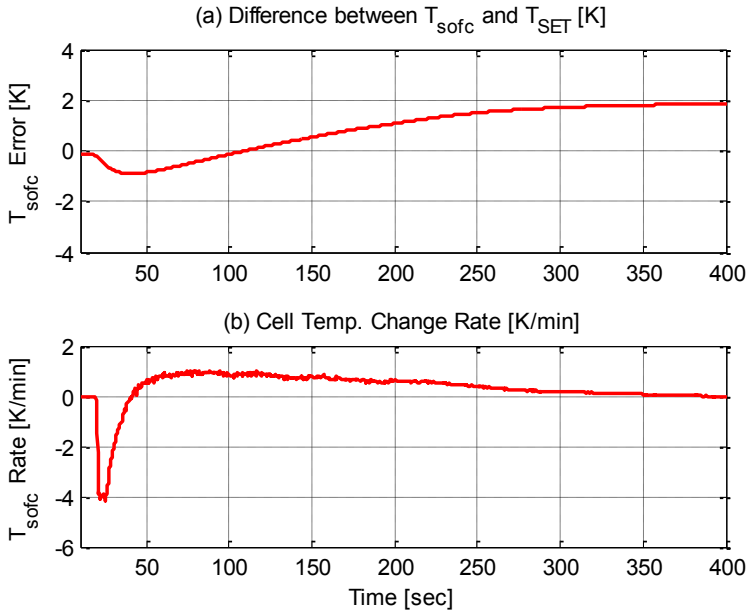

Figure 5.16: SOFC thermal transients during load step-up operation.

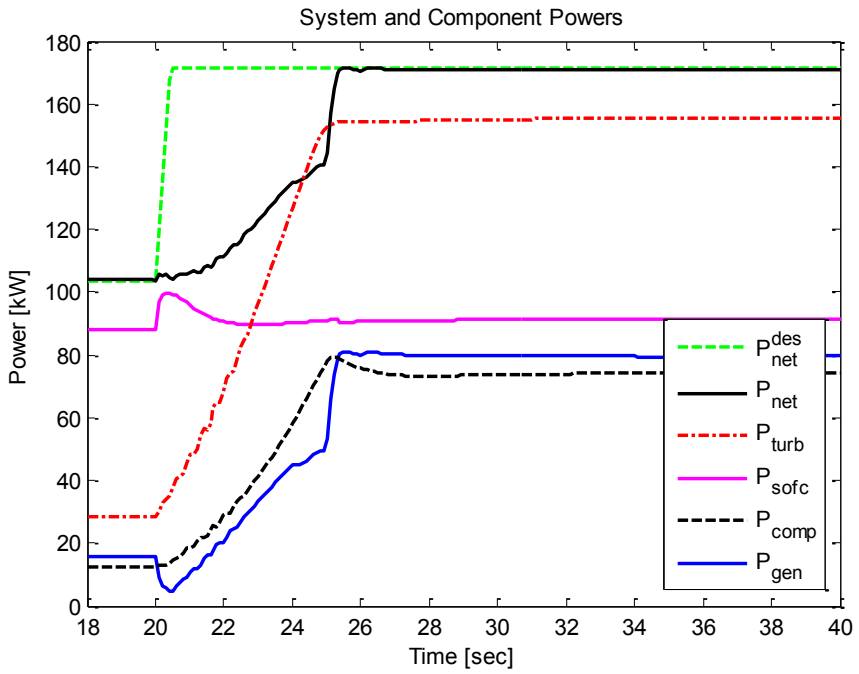

Figure 5.17: Power responses during load step-up operation.

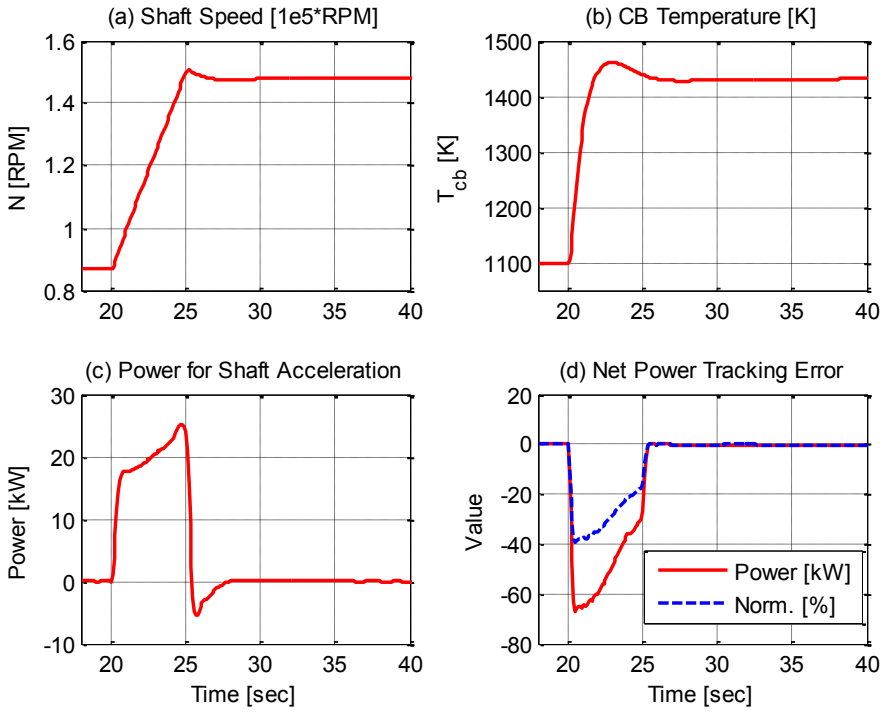

Figure 5.18: Load step-up transient responses.

5.3.2.2 Load Step-Down Transient Responses

The simulation results for load step-down operation from P_{peak} to P_{base} are given in Figure 5.19 to Figure 5.22. In particular, SOFC performance variables are presented in Figure 5.19 while the thermal transients are shown in Figure 5.20. Figure 5.21 shows the power responses during the short period of power transient.

During the load step-down transient, the current density I_{com} is mainly controlled according to the feedforward map. Hence, it varies slowly in a limited range, as shown in Figure 5.19. Recall that the CB temperature T_{cb} dominates the GT-generator power and net power. Thus, fast load reduction operation requires less fuel to be burned into the CB. Hence, the system fuel supply W_f decreases extremely fast to the minimum allowable W_f input, which is determined by the I_{com} command through Eqn. (5.18) in order to avoid hydrogen starvation. As shown in Figure 5.19, the SOFC FU ratio reaches FU_{UB} rapidly.

Both T_{cb} and the turbine power P_{turb} decrease as less fuel is fed into the system, as shown in Figure 5.22 and Figure 5.21, respectively. Thus, less P_{gen} can be drawn from the generator, which reduces the net power P_{net} for fast load following. The settling time for P_{net} response is around 7 seconds, as shown Figure 5.21. This is a bit longer than the load step-up case because a smaller (absolute value) shaft speed rate limiter is used.

It should be noted that some of the kinetic energy stored in the GT-generator shaft will be released when decelerating the GT shaft. This will deteriorate the load following performance. As shown in Figure 5.22 (d), the maximum absolute values for ΔP_{net} and ΔP_{net}^{norm} during power transient are 64.0KW and 61.7%, respectively. The over-produced power can be stored in a battery or ultra-capacitor pack in practice.

The SOFC power P_{sofc} is maintained in a relatively constant level because of the I_{com} controller. It should be noted that P_{sofc} decreases by about 10kW during the short period of power transient, as shown in Figure 5.21. This is due to the quick reduction in the fuel supply (see Figure 5.19), which reduces the SOFC voltage U_{sofc} because of the reduced species concentrations, as shown in Eqn. (2.2).

The proposed controller also achieves very good performance in keeping constant cell temperature, as shown in Figure 5.20. In particular, the difference between T_{sofc} and T_{SET} is limited in $\pm 2K$ while the T_{sofc} changing rate is less than 4 $K \cdot min^{-1}$.

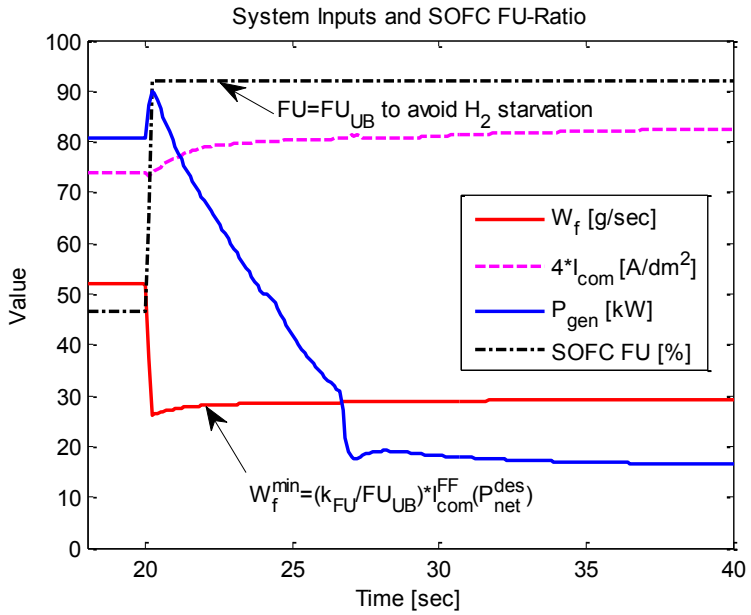

Figure 5.19: System inputs and SOFC FU ratio during load step-down operation.

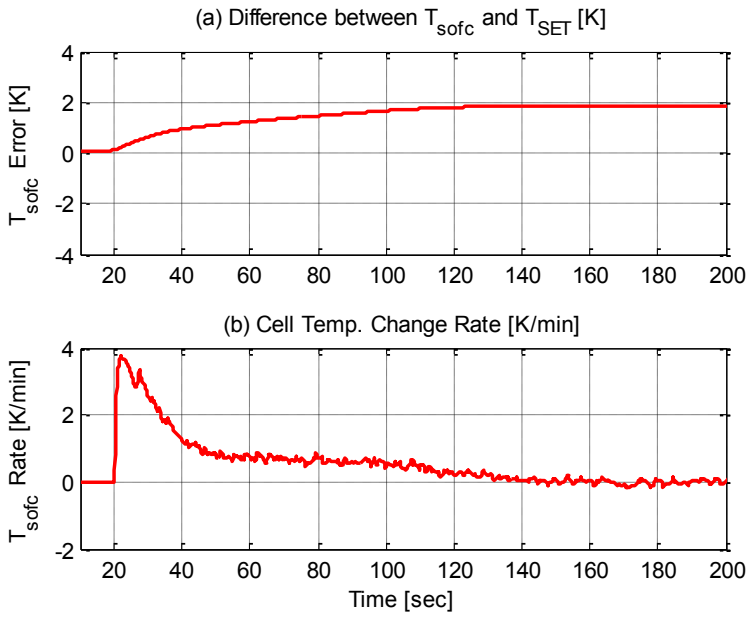

Figure 5.20: SOFC thermal transients during load step-up operation.

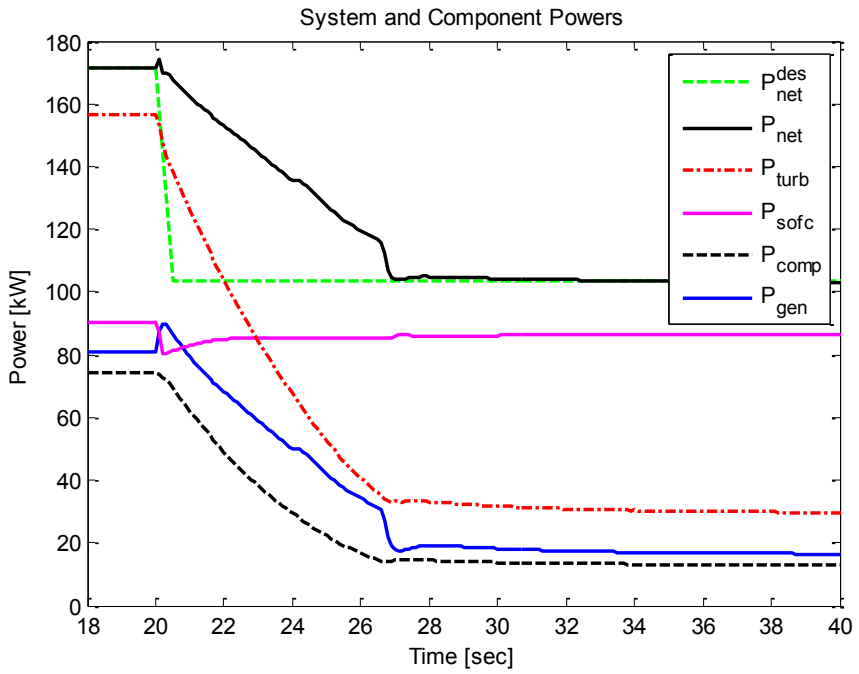

Figure 5.21: Power responses during load step-down operation.

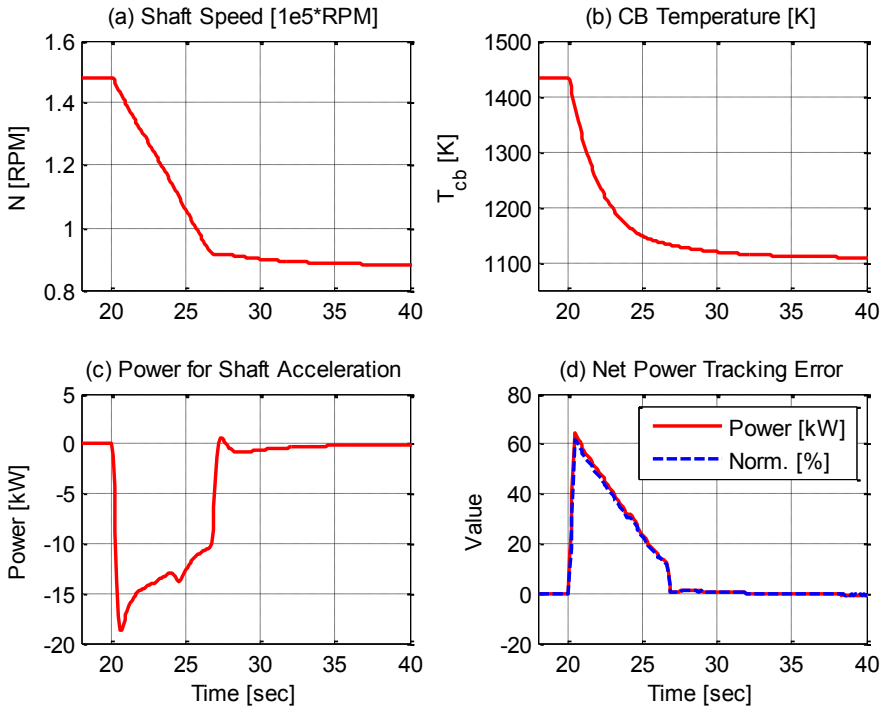

Figure 5.22: Load step-down transient responses. Note that the negative value in figure (c) indicates that kinetic energy stored in the shaft is released to the system.

Table 5.11 shows the summary of the proposed controller performance for the load step-down operation from P_{peak} to P_{base} in the S-SOFC/GT system.

Table 5.11 Summary of the load step-down operation

Performance metric parameters	Units	Value
The 2% net power settling time $T_s(P_{net})$	$[sec]$	6.9
The maximum (absolute value) P_{net} error P_{net}^{max}	$[kW]$	64.0
The maximum (absolute) value of ΔP_{net}^{norm}	[%]	61.7
SOFC temperature settling time $T_s(T_{sofc})$	$[sec]$	~180.0
Maximum T_{sofc} rate (absolute value)	$[K \cdot min^{-1}]$	~3.8

5.3.3 Comparison with the Conventional R-SOFC/GT System

Figure 5.23 and Figure 5.24 present the response of a "state-of-the-art" controller for a conventional R-SOFC/GT system with a nominal power of 220 kW [14]. Table 5.12 summarizes the system performance. As shown in the figures, we see that the net power response takes around 60 seconds and 80 seconds to settle for load step-up and load step-down operations. The SOFC thermal transient takes even longer, i.e., more than several hours to settle. This is because the slow SOFC thermal dynamics is excited very strongly by noticing that the SOFC temperature T_{sofc} varies by about 100K and 80K for the load step-up and load step-down transients, respectively.

Table 5.12 R-SOFC/GT system versus S-SOFC/GT systems

Transients	Parameters	R-SOFC/GT	S-SOFC/GT
Load Step-up	Power settling time	~ 60 seconds	5.3 seconds
	T_{sofc} settling time	~2.8 hours	~6.0 minutes
	SOFC temperature	~100K variations	$\lvert\Delta T_{sofc}\rvert < 2K$
Load Step-down	Power settling time	~ 80 seconds	6.9 seconds
	T_{sofc} settling time	>10 hours	~3.0 minutes
	SOFC temperature	~80K variations	$\lvert\Delta T_{sofc}\rvert < 2K$

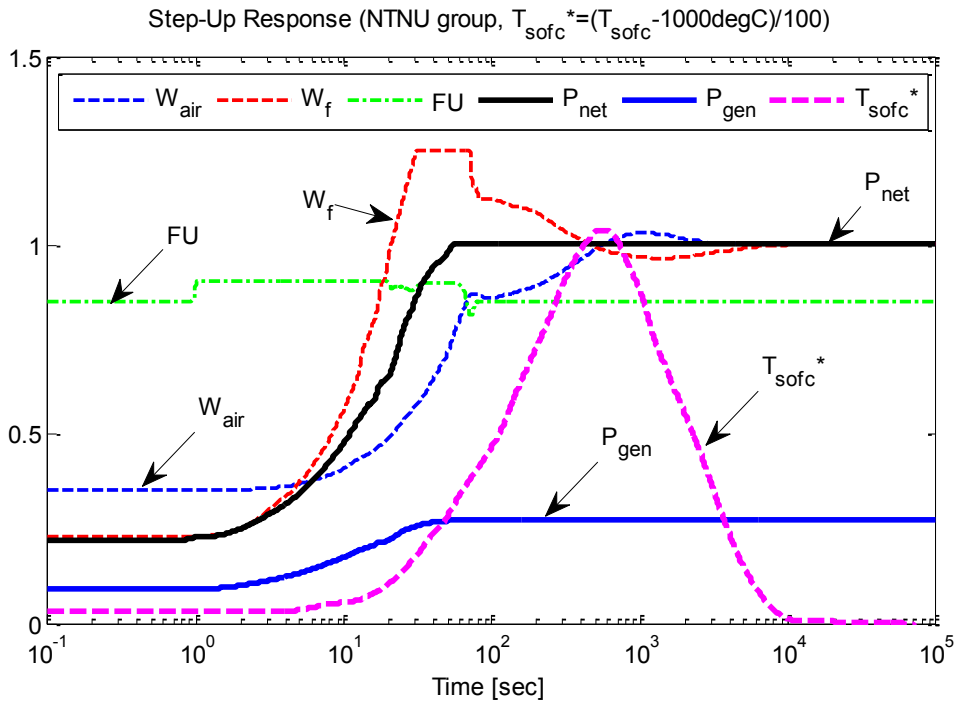

Figure 5.23: R-SOFC/GT system response to load increase (22% to 100%) [14].

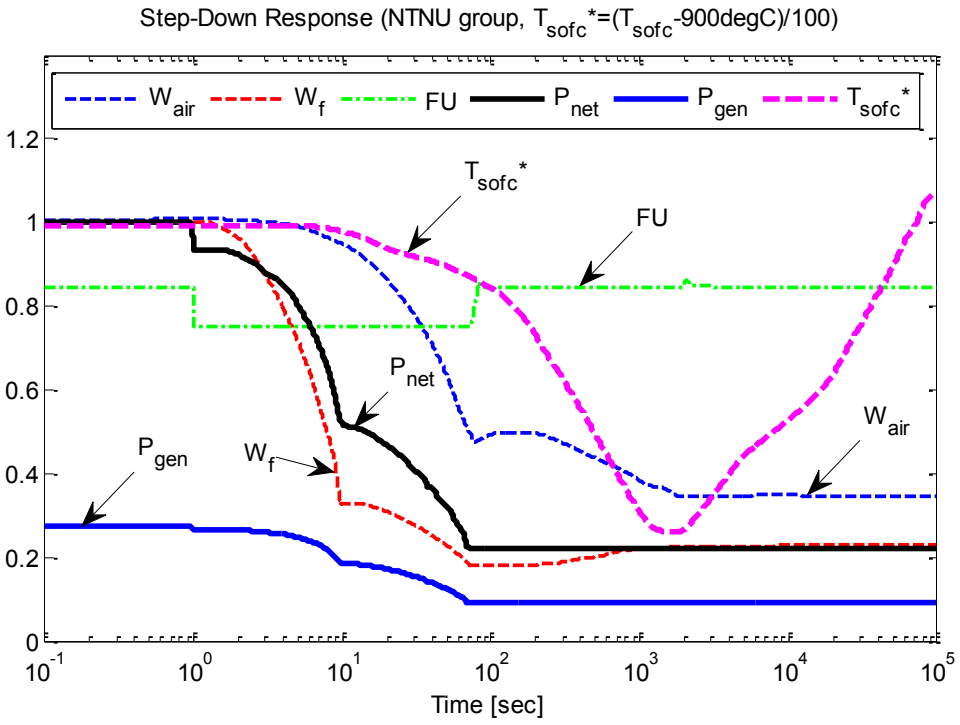

Figure 5.24: R-SOFC/GT system response to load decrease (100% to 22%) [14].

Compared to the R-SOFC/GT system, the transient capabilities of the proposed S-SOFC/GT system have been improved significantly, as shown in Table 5.12. In particular, the power response for the S-SOFC/GT system is about 10 times faster than that of the R-SOFC/GT system. The reason is that dynamic load following is mainly accomplished by taking full advantage of the fast GT-generator. In addition, large excitation of the slow SOFC thermal dynamics can be avoided by keeping fairly constant cell temperature.

5.3.4 Evaluation of the Proposed Control Strategy

The proposed control strategy is further evaluated by using a typical load profile consisting of multiple load step-up and step-down transients over multiple power levels. The simulation results for power responses and SOFC thermal transients are presented in Figure 5.25 and Figure 5.26, respectively. Table 5.13 summarizes the results.

Table 5.13 Summary of the load following performance

Performance metric parameters	Units	Value
The maximum (absolute value) P_{net} error P_{net}^{max}	$[kW]$	61.59
The maximum normalized P_{net} error ΔP_{net}^{norm}	[%]	56.80
Variation range of ΔT_{sofc}	$[K]$	[-1.0, 1.0]
Maximum T_{sofc} rate (absolute value)	$[K \cdot min^{-1}]$	3.64
System efficiency η_{net} over the load profile	[%]	49.25

As shown in Figure 5.25, good agreement between the desired net power P_{net}^{des} and the actual net power output P_{net} has been achieved. In particular, the load following is mainly accomplished by the generator power P_{gen} while the SOFC power P_{sofc} varies in a very limited range ($|\Delta P_{sofc}| < 10kW$). The maximum absolute values for ΔP_{net} and ΔP_{net}^{norm} are 61.6KW and 56.8%, respectively. A battery or capacitor pack can be used to compensate the net power error. The overall system efficiency over the entire load profile is about 49.25%, which is close the steady-state value. The controller also achieves very good performance in SOFC thermal management. The difference between T_{sofc} and the setting-value T_{SET} is limited in $\pm 2K$ while the T_{sofc} changing rate (the absolute value) is less than 4 $K \cdot min^{-1}$, as shown in Figure 5.26. Hence, the S-SOFC/GT system achieves far superior load following performance than the conventional R-SOFC/GT system and can be used as a primary propulsion system for mobile applications.

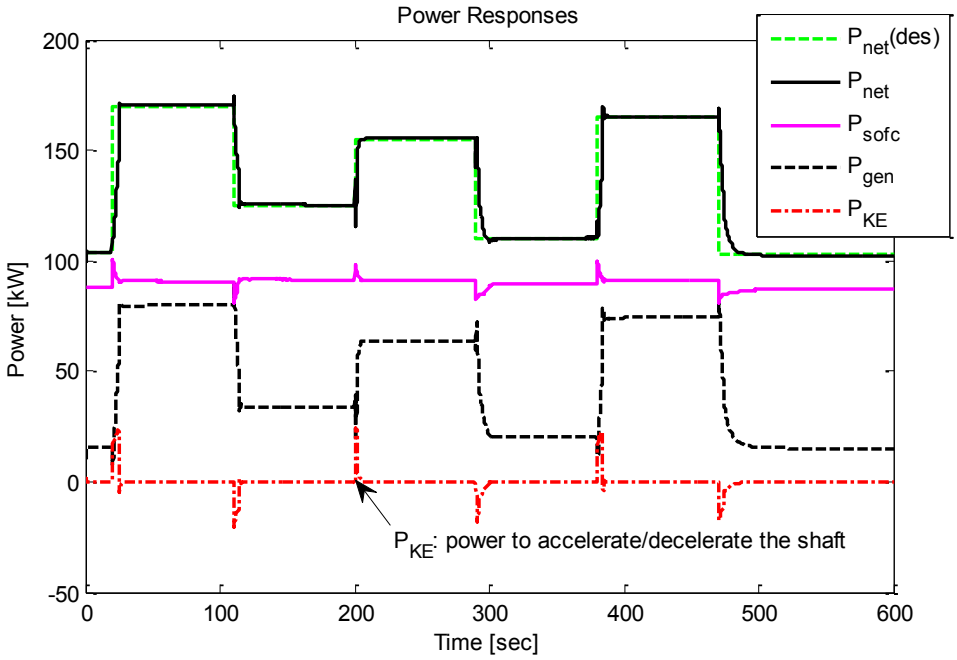

Figure 5.25: Power responses during dynamic load following.

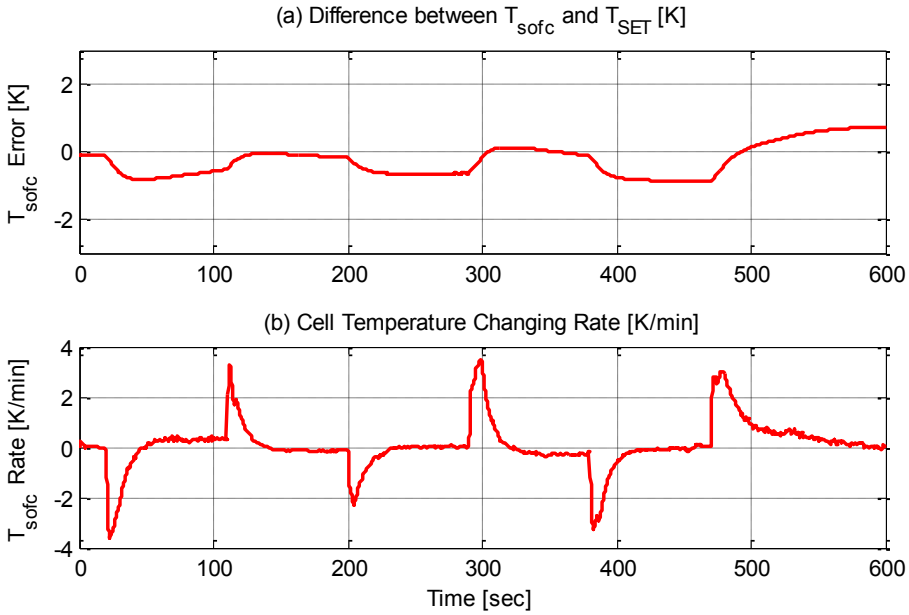

Figure 5.26: SOFC thermal transients during dynamic load following.

CHAPTER 6
Conclusions and Future Work

6.1 Conclusions

In this dissertation, we mainly focus on developing control and system integration solutions to achieve fast and safe load following operation of the SOFC/GT system for mobile applications. Two types of systems, i.e., the conventional recuperating-SOFC/GT system and the proposed sprinter-SOFC/GT system, have been studied through model-based methodologies. The main work and results are summarized as follows:

- A detailed dynamic model of the SOFC/GT system is developed. This model includes a tubular SOFC stack, a GT-generator assembly consisting of a compressor, a turbine and a generator, a catalytic burner and a counter-flow heat exchanger. The modeling principles and governing equations for the components are presented and the system model is derived by integrating models of these individual components. In the SOFC sub-model, the detailed spatial distribution of parameters in the SOFC is considered using the finite volume approach. Electro-chemical reactions and mass and energy balances are incorporated, and five temperature layers are assumed in the SOFC. The catalytic burner sub-model is developed by using mass and energy conservation and the ideal gas law. The heat exchanger model is based on the approach commonly used in thermodynamics. The turbomachinery model incorporates the shaft dynamics, the compressor and turbine model. Moreover, the SOFC model and the turbomachinery model are validated against experimental data. The dynamic SOFC/GT system model lays foundation for subsequent design and control studies.
- The generator/motor (G/M) dual mode operation is analyzed for improved transient performance of the conventional R-SOFC/GT system. The G/M dual mode operation and its control and design implications are investigated through load step-up and load

step-down case studies of a 5kW-class APU system. Active shaft load control is used to manage the load transients by: (a) pre-conditioning of G/M power for load step-up transients; and (b) absorbing the excessive power through motoring operation for load step-down transients. Feedback control and optimization algorithms are proposed for the G/M dual mode operation. Numerical simulations are carried out to demonstrate their effectiveness and computational efficiency. By taking full advantage of the G/M dual mode operation, better trade-offs between power tracking and thermal safety can be achieved, power and energy requirements for the energy storage (battery) can be reduced, and overall system performance can be enhanced.

- For the proposed sprinter-SOFC/GT system, operation strategy, design procedure and steady-state performance are investigated. In particular, through model-based analysis, an operational strategy is derived to coordinate the system inputs to maintain constant SOFC power and temperature over the entire load range. Based on this strategy, a system design procedure, which helps to determine component sizes and the reference steady-state operation line from the given power requirements, is developed. Feasible operating regimes and steady-state performance are studied for the sprinter system as well. The "actual" operating envelope is determined by integrating the constant SOFC power and temperature constraints with those pertinent to different safety factors. A constrained optimization problem is formulated to determine the static feed-forward map, which is used to schedule the actuators to achieve maximum fuel efficiency for different power demands. Finally, the S-SOFC/GT system is compared with the R-SOFC/GT system in terms of operation envelope and steady-state performance.
- Stability analysis and feedback control design are performed for the new S-SOFC/GT system. The BIBO stability with respect to the generator load is investigated through numerical simulations and linearized system analysis of a simplified "2-state" model, which captures the dominating dynamics of the full-order model. Shaft speed control is proposed to stabilize the system at desired operating points. Meanwhile, open-loop analysis and relative gain array (RGA) analysis are used to gain insights on system transients, loop interactions and operation challenges. Based on these analysis and the characteristics of the S-SOFC/GT system, a cascade feedforward-feedback control strategy is developed. It is shown, through numerical simulations, that by taking full

advantage of the GT-generator's fast dynamic capabilities, the proposed S-SOFC/GT system could achieve far superior load following performance, when compared with the "state-of-the-art" results for the conventional R-SOFC/GT system.

6.2 Future Work

The work presented in this dissertation can be extended in several directions:

- ***Model Validation***

The integrated dynamic model needs to be validated in a system level so that the approaches and solutions developed in this dissertation can be implemented for practical applications. Although key sub-models such as the SOFC and turbomachinery have been validated against experiment data available in the literature, the integrated system model has not been verified in a system level due to the lack of experiment data. Therefore, one important future work is to acquire system level experiment data from either a test facility or a hardware-in-the-loop (HIL) simulation facility [20]. In doing so, we can validate the model and calibrate the parameters using both steady-state and transient experiment data. System identification techniques can be used to calibrate these parameters. Note that it is important to validate the air/gas flow pressure and temperature distributions and the inter-connections between different components.

- ***Development of a Control-Oriented Model***

Currently, the integrated SOFC/GT system model comprises 49 coupled nonlinear ordinary differential equations as well as many nonlinear functions. This limits options for system design and control analysis. Dynamic models that capture the key dynamic characteristics of the hybrid SOFC/GT system but have reduced complexity are preferred to facilitate model-based design and analysis. There are several approaches focusing this subject in the open literature. For example, model reduction has been achieved by using the linear parameter varying (LPV) structure of the SOFC in [75]. Other authors also developed reduced-order models by assuming uniform pressure/temperature distributions inside the SOFC, as explained in [47]. However, these over-simplified models produced

considerable errors [47]. A promising approach for model reduction is to use descriptive functions [76], [77] for the temperature and current distributions in the SOFC.

- ***Model Expansion and Augmented System Configuration***

Additional balance-of-plant components such as the on-board fuel processing and supply system might pose even more challenges with respect to the system operation and performance. Integrating these components into the SOFC/GT system and examining the performance of the augmented system could be a significant extension to this work. For example, the S-SOFC/GT system can be augmented by using bypass valves and/or the additional CB fuel supply system. In this case, the model needs to be expanded to reflect the augmented system configuration. Moreover, operational strategy (to maintain fairly constant SOFC power/temperature), design procedure, and operation envelope associated with the augmented system need to be developed. In addition, control analysis and design should be investigated for the augmented system.

- ***Further Control Analysis***

Fast load following and thermal management for the hybrid SOFC/GT system are investigated in this work. However, there might be some physical constraints such as the generator power/torque constraints that may dictate the dynamic operation of the hybrid SOFC/GT systems for practical applications. In this case, model predictive control [74] could be used to solve these problems. Moreover, other control issues might arise if the system is integrated with balance-of-plant components. Understanding and mitigating the control issues are important for future studies.

APPENDICES

APPENDIX A

Specifications of the 5kW SOFC/GT-based APU System

Key parameters of the 5kW class SOFC/GT-based APU system is summarized in Table APX.1. The SOFC stack consisting of 60 tubular cells (see Section 2.1) generates 5.60kW electric power at a temperature of 1020K. Figure APX.1 presents the normalized GT map, which is acquired from the *GasTurb* software [73]. The similarity principle [25] is used to scale the original 100kW-class GT map [14], [73] for this specific APU system. In addition, constant isentropic efficiencies, i.e., $\eta_c = 75\%$ and $\eta_t = 80\%$, are assumed for the compressor and turbine for simplifications. The HEX is sized to keep the SOFC inlet air temperature at around 900K at full load condition.

The SOFC/GT-based APU system achieves around 45% efficiency over a power range from 3.50kW to 6.10kW. The power split ratio P_{gen}/P_{net} is about 10%. This value is less than that of large size systems [4]. For example, the 220kW SOFC/GT system in [14] has a P_{gen}/P_{net} ratio of around 20%.

Table APX.1 Key parameters of the SOFC/GT-based APU system.

Components	Parameters	SOFC/GT-based APU
SOFC Stack	Cell number N_{cell} [-]	60
	SOFC temperature T_{sofc} [K]	950 - 1020
	SOFC power P_{sofc} [kW]	3.20 - 5.60
	Current density I_{com} $[A \cdot m^{-2}]$	1200 - 2100
	Fuel utilization FU [-]	~85%
GT-Generator (@ design point)	Compressor pressure ratio PR [-]	~2.70
	Compressor flow W_c $[g \cdot sec^{-1}]$	20.0
	Turbine inlet temperature [K]	873K (600℃)
	Turbine expansion ratio ER [-]	~2.60
	Corrected turbine swallowing capacity ϕ_{choke} $[kg \cdot K^{0.5} \cdot s^{-1} bar^{-1}]$	0.35
	Designed shaft speed [RPM]	3.80e5
	Effective shaft inertia J $[kg \cdot m^2]$	1e-4
HEX	HEX efficiency	68.7%
Integrated System	Net power range (SS-line) [kW]	3.50 - 6.10
	Net power efficiency (SS-line) [-]	~45.0%

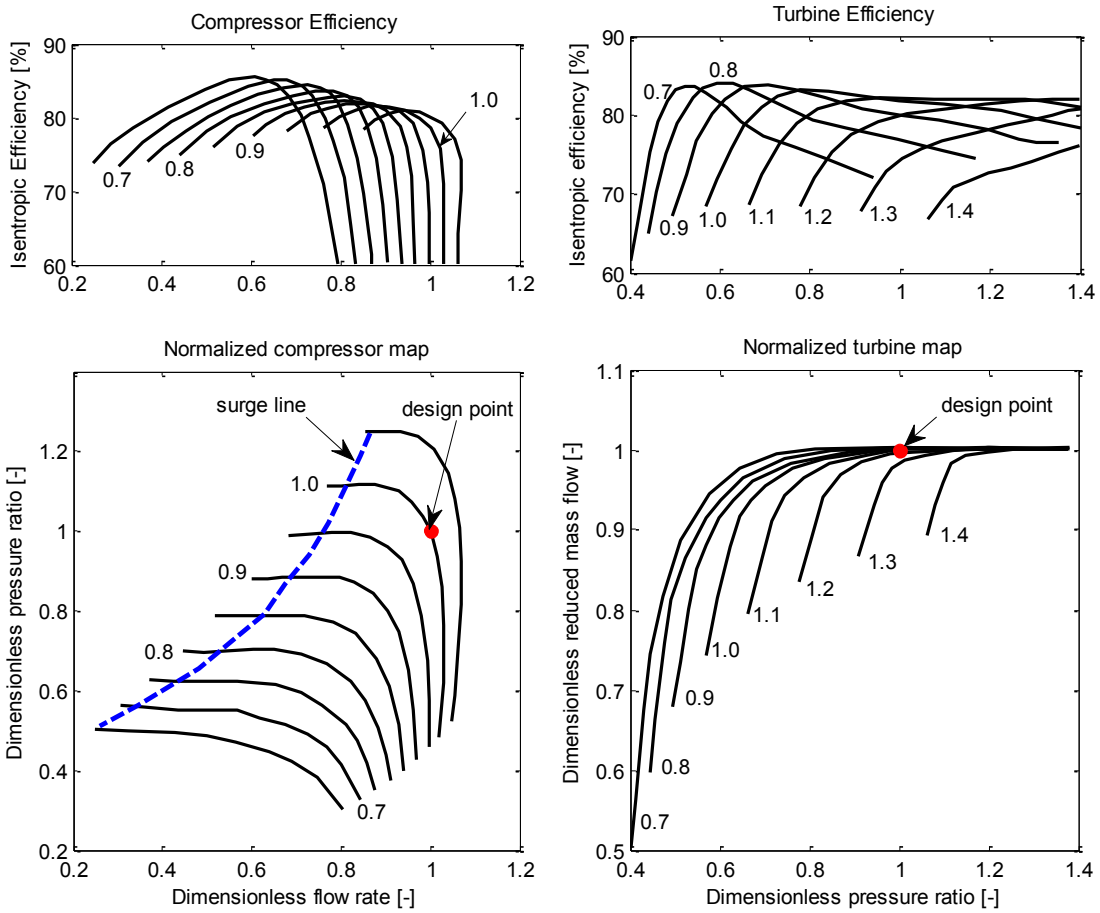

Figure APX.1: Normalized compressor and turbine maps for the 5kW-class SOFC/GT-based APU system. The GT maps are acquired from [14].

APPENDIX B
Steady State Performance of the Recuperating-SOFC/GT System

First, we identify the feasible operation envelope of the R-SOFC/GT system (see Table 4.2 for its specifications) with boundaries determined by considering safety factors in Section 4.4.1. Next, we investigate the off-design performance and part-load operation within the valid operation regime. Influence of varying fuel utilization (FU) coefficients and the maximum permissible CB temperature will also be studied.

C. 1. Feasible Operation Regime

The R-SOFC/GT system has three inputs: fuel flow W_f, current density I_{com}, and generator load P_{gen}. Note that other variable sets are also valid, such as the SOFC power P_{sofc} instead of the SOFC current I_{com}, or the generator torque instead of the generator power. With any combination of input variables, there are three degrees of freedom for part-load operation [14]: (1) variation of the airflow W_{air} through shaft speed control by manipulating P_{gen}; (2) variation of the fuel flow W_f; and (3) variation of the SOFC fuel utilization (FU). Note that the fixed FU constraint, e.g., constant FU ratios of 80% and 85% were used in [69] and [14], respectively, used by many references will be relaxed here to present a complete picture for the conventional R-SOFC/GT system.

At certain operation regions (i.e., certain combinations of W_{air}, W_f, and FU), the hybrid system might be damaged due to safety issues discussed in Section 4.4.1. A matrix of steady-state simulations with the designed R-SOFC/GT system has been performed to identify the feasible operation region with constraint values listed in Table 4.4. As shown in Figure APX.2, various constraints have been applied to identify the feasible operation region for different FU coefficients in the range of [0.75, 0.90]. Figure APX.2 (b) shows the 3D feasible operation region with the low/high airflow boundaries and different fixed-FU slices. The feasible region shifts to high airflow region as FU decreases. The reason is that more unused fuel is burned in the CB to increase the turbine power as FU decreases, thereby delivering more air to the SOFC. Detailed discussions of the 2D operation region

for fixed FU will be presented in the following section.

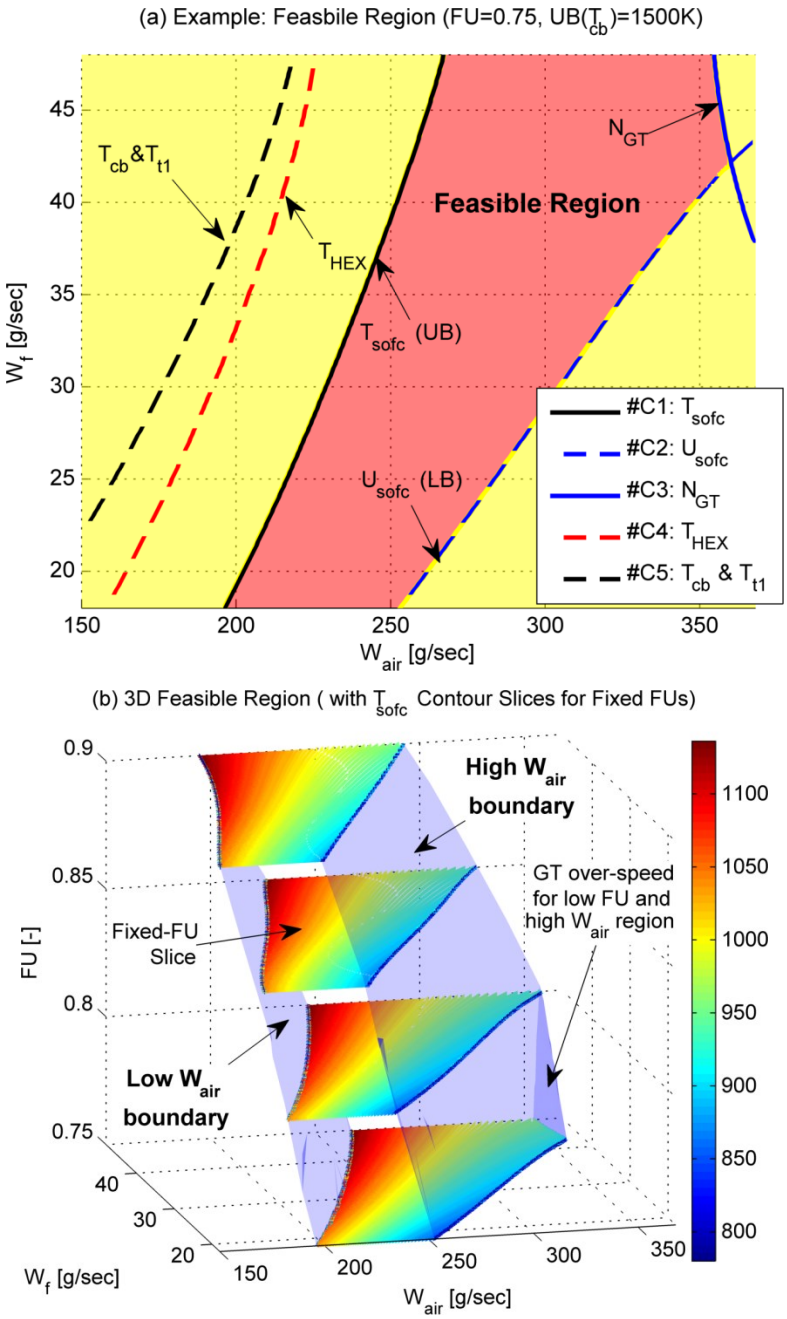

Figure APX.2: Feasible operation region for the R-SOFC/GT system.

C. 2. System Performance with Fixed Fuel Utilization

Without loss of generality, we take a fixed FU ratio of 75% as an example and evaluate the system performance in this section. Figure APX.2 (a) presents the operation

envelope with following issues observed to occur at certain regimes:

- Overheating appears for high fuel flow and low airflow. At this regime, simulations reveal that the temperature is steadily ramping beyond the valid region and causing compressor surge. This phenomenon determines the low airflow boundary. It should be pointed out that the CB temperature upper bound T_{cb}^{UB} also affects the low airflow boundary, as will be discussed in the next section.
- For the case of low fuel flow and high airflow, the SOFC is cooled down strongly, thereby leading to low cell voltage and efficiency. It is not recommended to operate in this regime due to the risk of cell cracking caused by low SOFC temperature. For the R-SOFC/GT system here, the region with a voltage less than 0.45V is considered invalid. This determines the high airflow boundary of the feasible region.
- The GT speed should be maintained in the desired range for safety considerations. However, GT over-speed is likely to occur for extremely high airflow regions, as shown in Figure APX.2. In order to ensure proper GT functioning, the regime where the shaft speed lies outside the permissible range $[N^{LB}, N^{UB}]$ is blinded out.

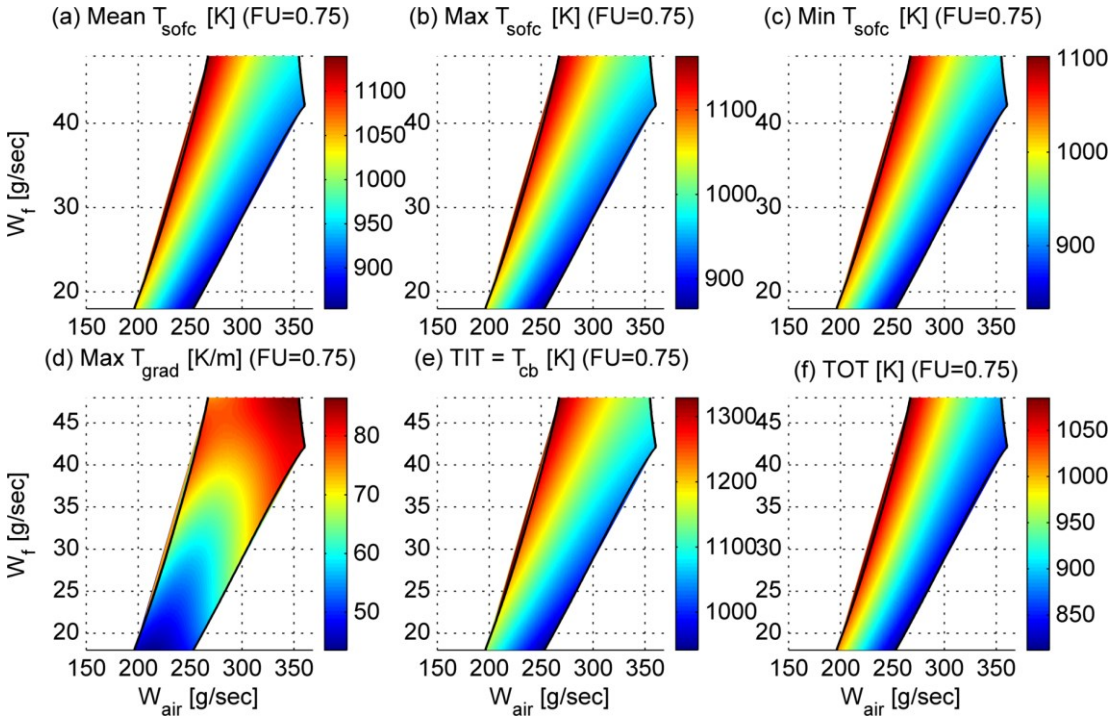

Figure APX.3: Temperature related variables for fixed FU in the recuperating system.

Figure APX.3 shows the temperature related variables regarding component over-heating, cell cracking and thermal fatigue. The SOFC temperatures (i.e., the mean value and the maximum/minimum local values) and the turbine inlet and outlet temperatures have similar distributions. All of them are decreasing functions of W_{air} due to the cooling effect and increasing functions of W_f. The reason is that more fuel is reacted in the CB to raise the burner/turbine temperatures and the SOFC inlet air temperature, thereby leading to increased cell temperatures. As shown in Figure APX.3 (d), as the absolute values of air and fuel flow increase, the SOFC temperature gradient increases due to the increased thermal energy produced by stronger electro-chemical reactions.

Figure APX.4 shows the power related variables. As shown in Figure APX.4 (a), the SOFC power P_{sofc} is an increasing function of W_f, and a decreasing function of W_{air} due to the reduced T_{sofc} caused by the cooling effect. The compressor power P_{comp} (see Figure APX.4 (b)), which has a similar distribution to the shaft speed N, increases with the air and fuel flows. Note that N is closely related to the airflow; therefore, the contour-lines in Figure APX.5 (d) are steep. Turbine power P_{turb} (Figure APX.4 (c)) increases with the air and fuel flows due to the increased turbine inlet pressure p_{t1} ($p_{t1} = p_{cb}$, see Figure APX.5 (e)). As shown in Figure APX.4 (d) and (e), the generator load P_{gen} and the net power P_{net} have similar distributions, i.e., both of them are increasing functions of W_f and decreasing functions of W_{air}. As shown in Figure APX.5 (f), the power split ratio P_{gen}/P_{net} increases with respect to W_{air}. High efficiency η_{net} (Figure APX.4 (f)) is achieved at low airflow regions due to high SOFC and turbine temperatures.

Figure APX.5 shows other operational variables. The current density I_{com} (Figure APX.5 (b)) is only a function of W_f, as they are coupled by the fixed FU ratio. Similar to the result in [14], the cell voltage U_{sofc} (Figure APX.5 (a) and Figure APX.6) increases when going to part-load at high temperature. The reason is that the voltage loss U_{loss} is closely related to the current I_{com}, which is proportional to the fuel flow W_f for fixed FU. Meanwhile, the open circuit voltage U_{OCV} increases with W_f with a slope proportional to $ln(W_f)$, as shown in the Nernst equation in Eqn. (2.2). Hence, U_{OCV} has a smaller slope relative to W_f than U_{loss}. Consequently, the voltage U_{sofc} decreases with W_f, as shown in the contour-plots in Figure APX.6. The air excessive ratio AR increases when going to

part-load, due to the increased W_{air}/W_f ratio [21], as shown in Figure APX.5 (c).

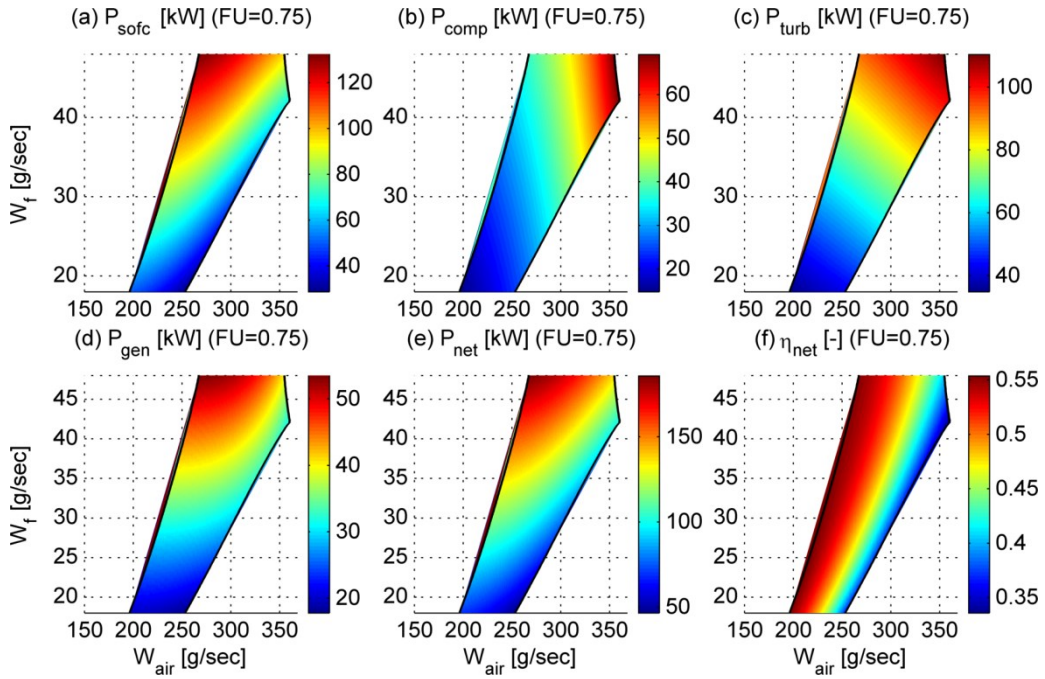

Figure APX.4: Power related variables for fixed FU in the recuperating system.

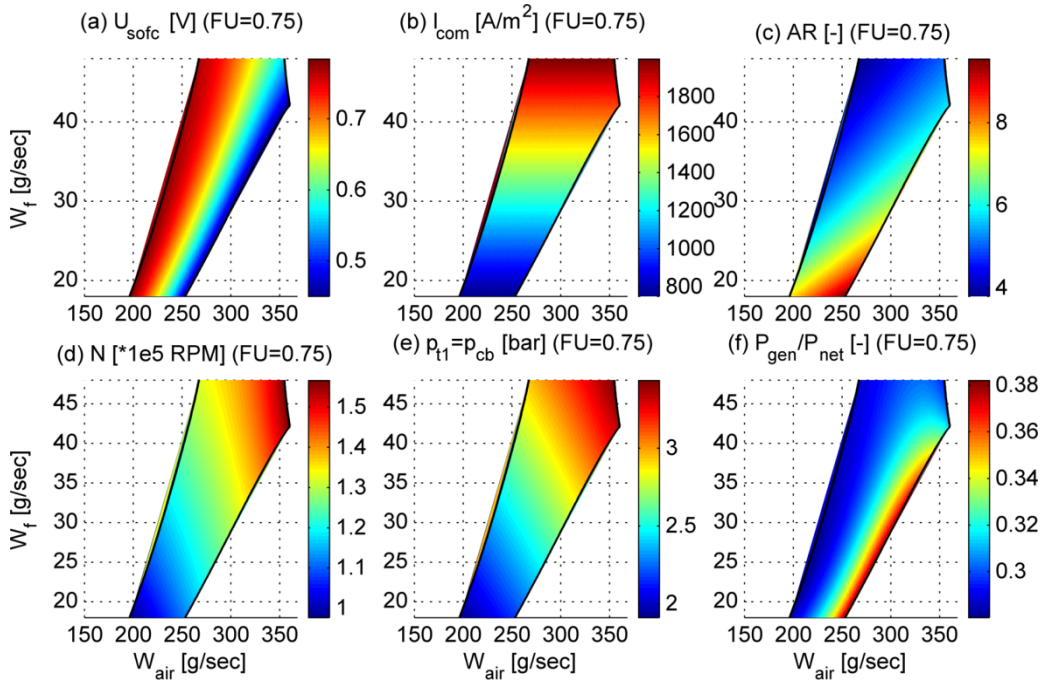

Figure APX.5: Other operational variables for fixed FU in the recuperating system.

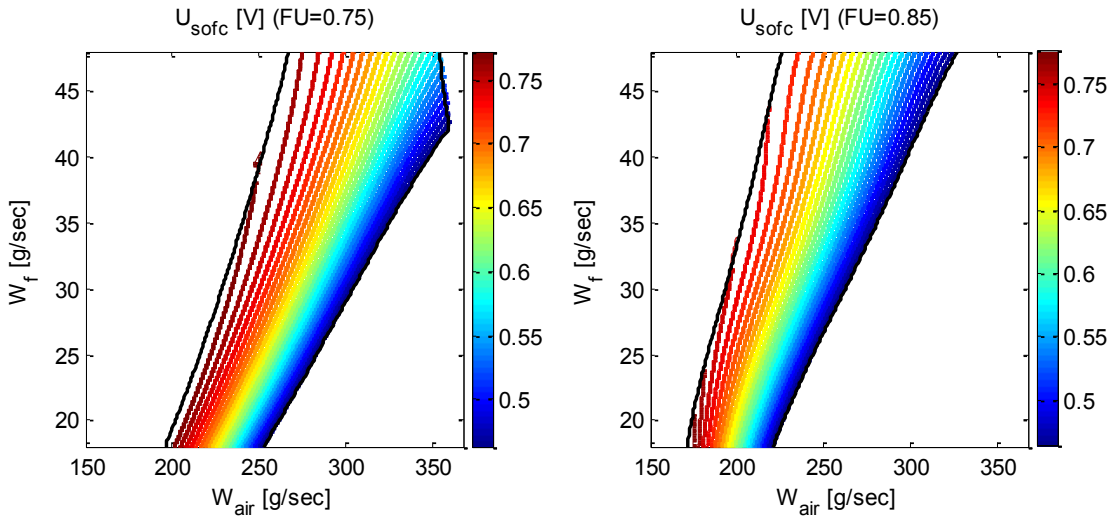

Figure APX.6: High cell voltage achieved when going to part-load at high temperature for different fuel utilization cofficients.

C. 3. Influence of Varying Fuel Utilization Coefficients

The effect of varying FU ratios on the system performance, which has not been systematically studied in the literature (e.g., [14], [21] and [69]), will be investigated in this section. We first study the "local" effect of varying FU ratios by fixing the fuel flow (e.g., $W_f = 42\ g/sec$ in the case study) and explore the "global" behavior by examining the 3D contour-slice plots (see Figure APX.10) of different performance indices.

Figure APX.7 shows the temperature related variables. As shown in the figure, the SOFC temperatures, including the mean values and minimum/maximum local values, have similar distributions, i.e., the constant temperature contour-lines are nearly parallel to the low/high W_{air} boundaries. Both the turbine inlet/outlet temperatures increase when reducing FU since more fuel is burned in the CB, as shown in Figure APX.7 (e) and (f), respectively. The maximum local cell temperature gradient (Figure APX.7 (d)) decreases when reducing FU due to (1) the reduced degree of electro-chemical reaction, i.e., less fuel is reacted in the SOFC stack; and (2) the increased air flow which helps to smooth the spatial temperature distributions along the SOFC.

The power related variables and other variables are shown in Figure APX.8 and Figure APX.9, respectively. As FU decreases, the SOFC power P_{sofc} (Figure APX.8 (a)) slightly decreases due to the reduced current I_{com} as in Figure APX.9 (b). Turbine power

P_{turb} (Figure APX.8 (c)) increases significantly when reducing FU since more unused fuel is burned in the CB to elevate the turbine inlet temperature as in Figure APX.7 (e). The compressor power P_{comp} (Figure APX.8 (b)), which is dominated by the shaft speed N (Figure APX.9 (d)), increases when reducing FU since more airflow is delivered due to the increased P_{turb}. Hence, the generator power P_{gen} (Figure APX.8 (d)) increases as FU decreases. Consequently, the net power P_{net} (Figure APX.8 (e)), the net efficiency η_{net} (Figure APX.8 (f)), and the power split ratio P_{gen}/P_{net} (Figure APX.9 (f)) all increase as FU decreases. As shown in Figure APX.9 (a), the cell voltage U_{sofc} increases if reducing FU due to (1) increased open circuit voltage U_{OCV} due to less product concentrations in the SOFC cathode channel; and (2) reduced voltage loss U_{loss} due to the reduced current density I_{com} as shown in Figure APX.9 (b).

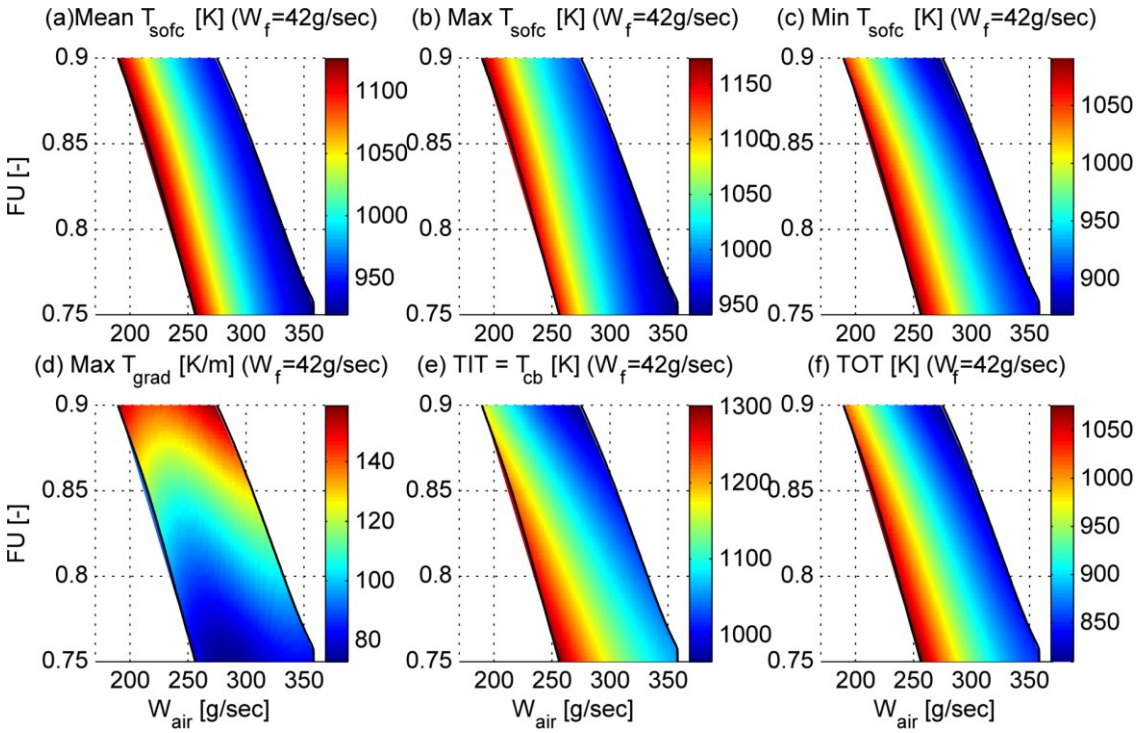

Figure APX.7: Temperature related variables for fixed W_f in the recuperating system.

The "global" picture of the system performance over the 3D operation envelope is presented in the form of contour-slice plots in Figure APX.10. The same conclusions as those drawn in the previous section can be made for each fixed-FU slice.

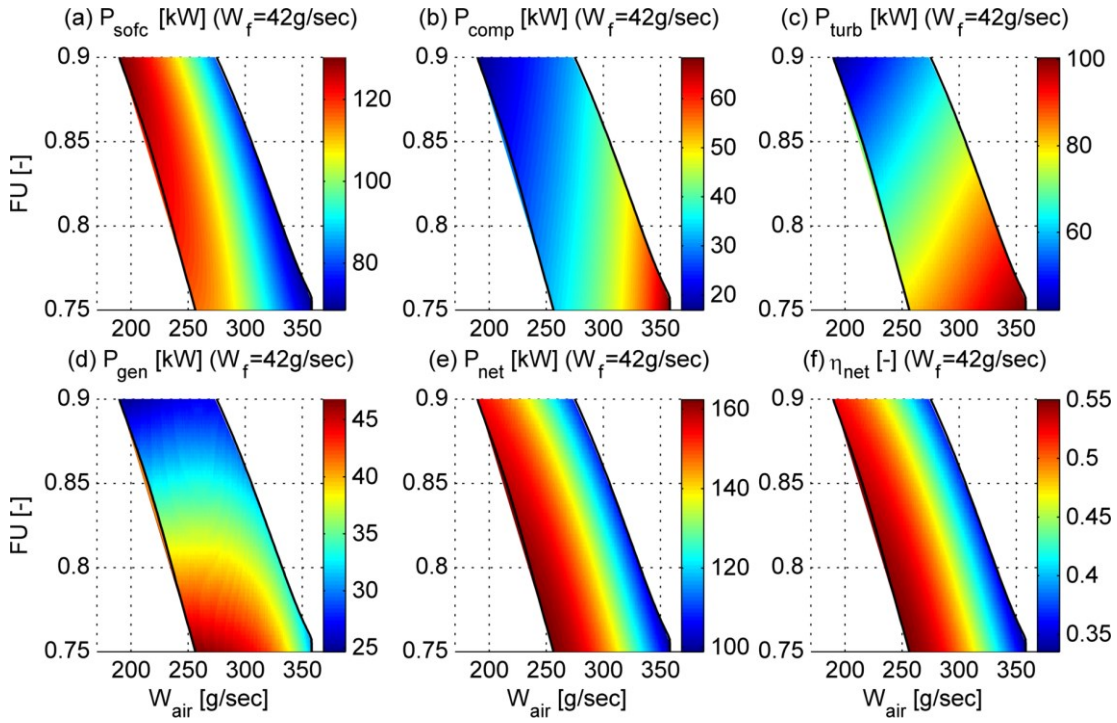

Figure APX.8: Power related variables for fixed W_f in the recuperating system.

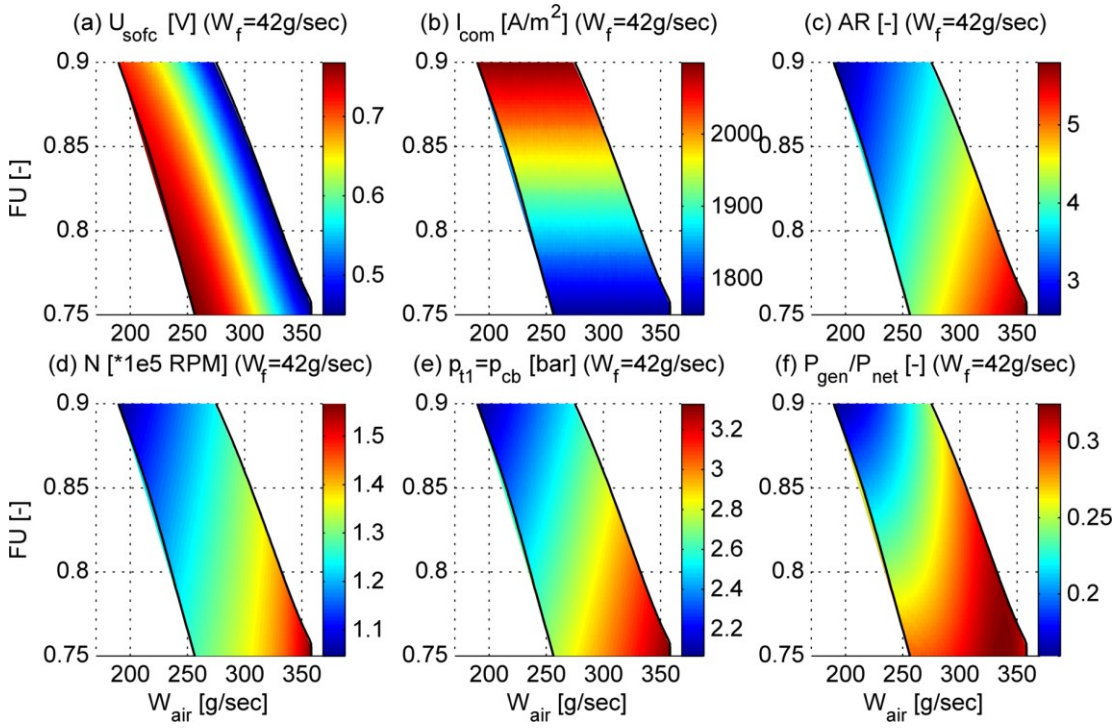

Figure APX.9: Other operational variables for fixed W_f in the recuperating system.

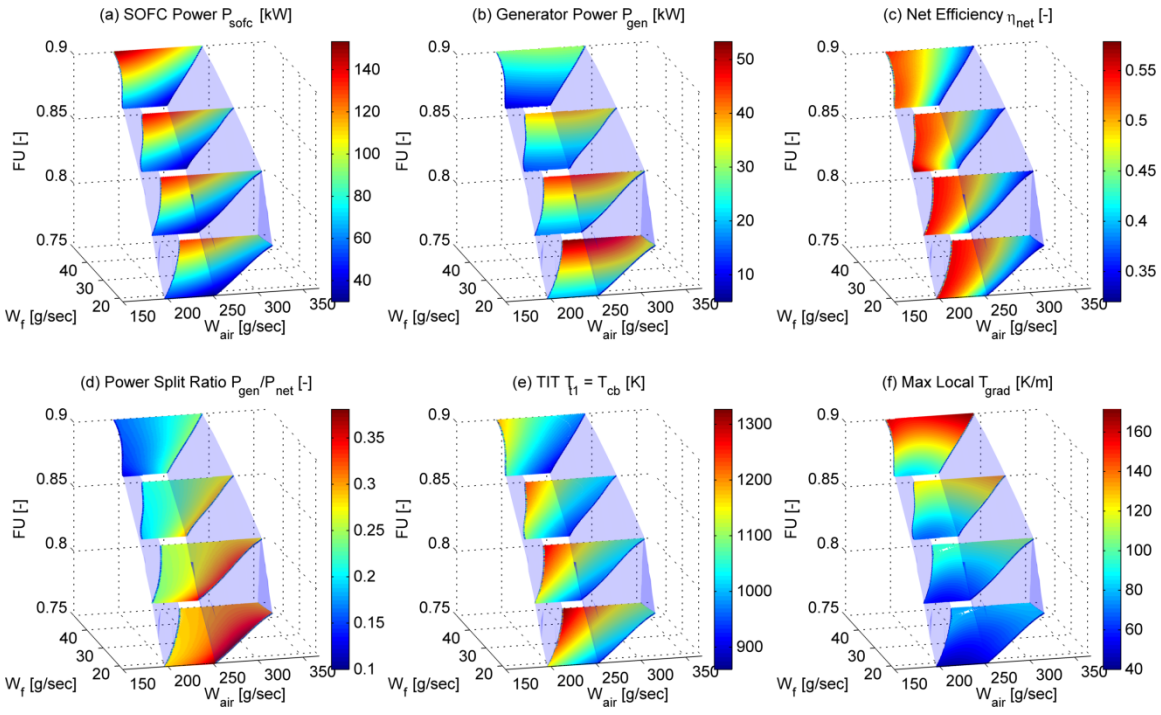

Figure APX.10: The global picture of the system performance over the 3D feasible operation region.

The effects of varying FUs on the "global" performance are similar to those for fixed W_f inputs, i.e., the "local" behavior shown in Figure APX.7 to Figure APX.9. The SOFC power P_{sofc} in Figure APX.10 (a) slightly increases as FU increases due to the increased I_{com}. As FU decreases, the turbine power P_{turb} increases due to the increased turbine inlet temperature, as shown in Figure APX.10 (e). Consequently, the generator power P_{gen} and the power split ratio P_{gen}/P_{net} increase significantly when reducing FU, as shown in Figure APX.10 (b) and (d). As shown in Figure APX.10 (c), the efficiency η_{net} slightly increases as FU decreases. Therefore, the optimal set-points are located at the low FU regions, as shown in Figure APX.11 for the case of T_{cb}^{UB} equals 1500K. As shown in Figure APX.10 (f), the maximum local T_{grad} decreases when reducing FU due to the reduced current density which weakens the SOFC electro-chemical reactions and increased airflow which smoothes the cell temperature distributions.

C. 4. Influence of Constraint Values

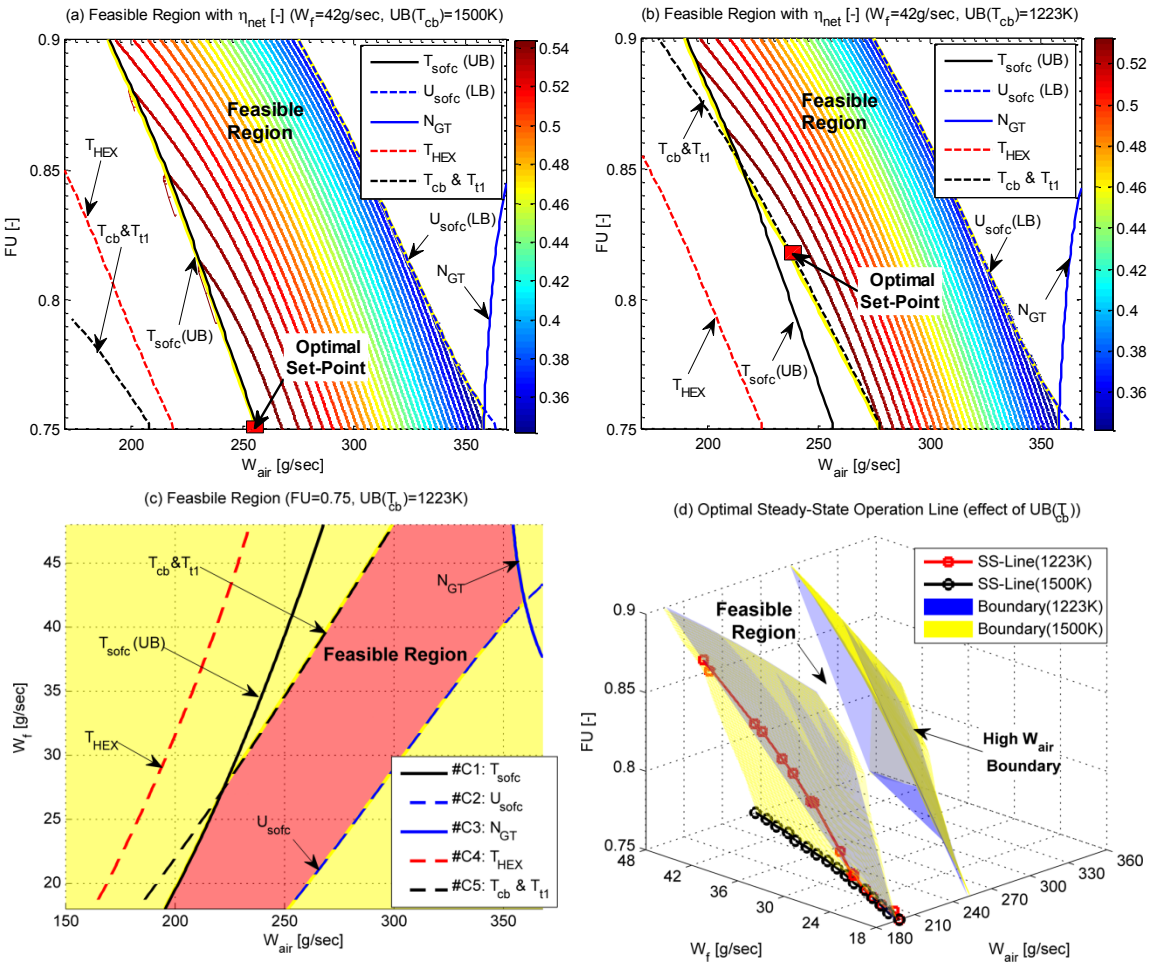

Figure APX.11: Effect of the burner temperature upper bound value on the feasible operation region and optimal set-point.

Constraint values listed in Table 4.4 affect the feasible operation region of the R-SOFC/GT system. Intensive simulations indicate that the burner temperature upper bound T_{cb}^{UB} has the most significant effect on the operation envelope among all these constraints. For example, the T_{cb}^{UB} value will decrease from 1500K to 1223K (i.e., 950℃) if the multi-stage high-temperature CB (see Figure 2.12) is replaced with a conventional single-stage metallic CB [39]. Then, the 3D feasible operation region will shrink as in Figure APX.11 (d) because the low airflow boundary for the low FU and high W_f regions will be limited by the T_{cb}^{UB} constraint, as shown in Figure APX.11 (c).

The value T_{cb}^{UB} will also affect the location of the optimal set-points. For example, as the T_{cb}^{UB} constraint becomes active, the optimal set-point for $W_f = 42\ g/sec$ is shifted from Figure APX.11 (a) to Figure APX.11 (b). The optimal steady-state operation line in Figure APX.11 (d) is also shifted. The maximum achievable net power is reduced from 187.90kW to 180.90kW as T_{cb}^{UB} decreases from 1500K to 1223K.

C. 5. Optimal Steady-State Performance of the Recuperating System

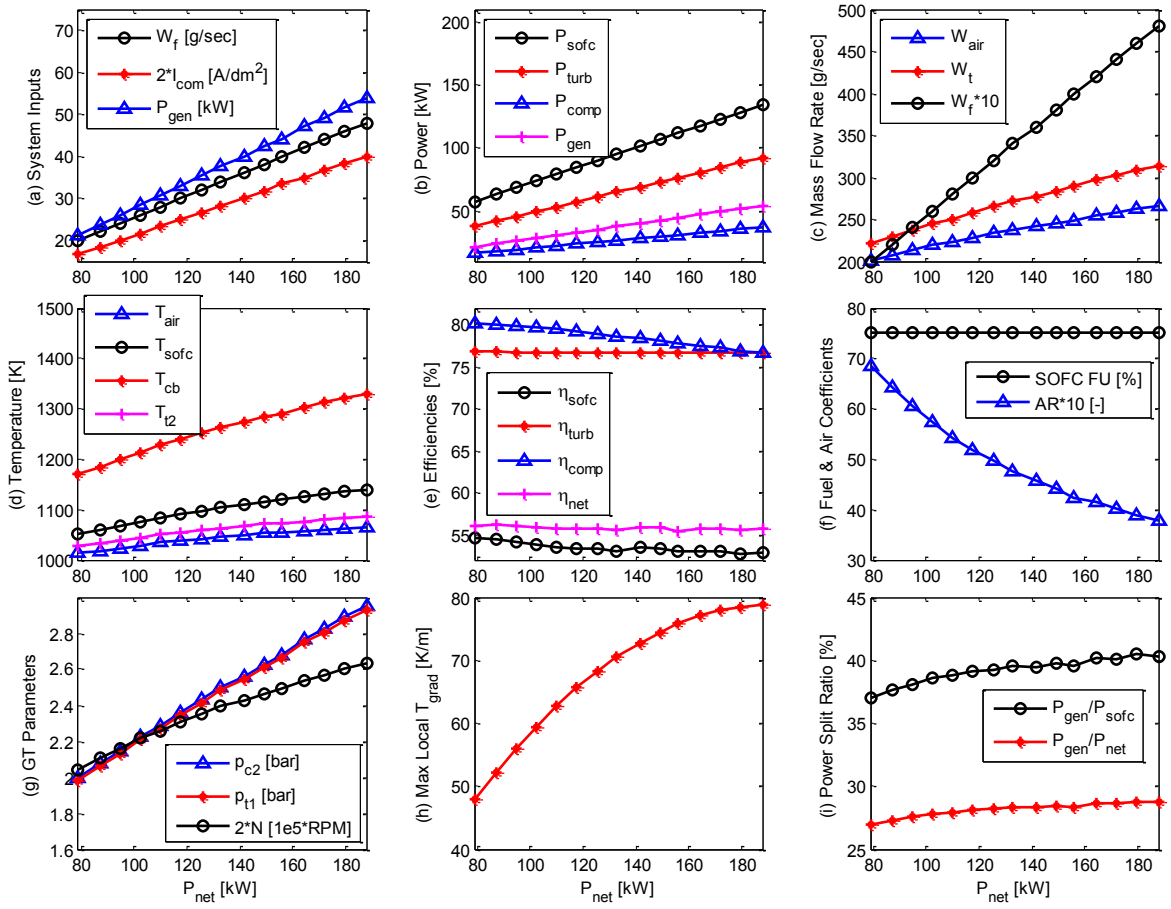

Figure APX.12: The R-SOFC/GT system performance along the optimal operation line.

Figure APX.12 presents the R-SOFC/GT system performance over the optimal steady-state operation line. Net power P_{net} varies from 78.8kW to 187.9kW. As shown in Figure APX.12 (a), all the system inputs, i.e., W_f, I_{com} and P_{gen}, are very close to linear

increasing functions of P_{net}. This is the same as those listed in our previous studies [7]. All the powers, e.g., P_{sofc}, and P_{comp}, air flow rates, e.g., W_{air} and W_t, and temperatures, e.g., T_{air}, T_{sofc}, T_{cb} and T_{t2}, increase as the net power demand P_{net} increases, as shown in Figure APX.12 (b), (c) and (d), respectively. Both the SOFC power P_{sofc} (P_{sofc} varies from 57.5kW to 133.9kW) and the SOFC temperature T_{sofc} (T_{sofc} varies from 1051K to 1140K) vary significantly over the entire load range. In addition, as P_{net} increases, both the compressor outlet pressure p_{c2} and the turbine inlet pressure p_{t1} ($p_{t1} = p_{cb}$) increase due to the increased shaft speed N, as shown in Figure APX.12 (g).

Fairly constant net efficiency η_{net}, i.e., $\eta_{net} = 55.8\% \pm 0.3\%$, has been achieved over the entire load range, as shown in Figure APX.12 (e). This observation is the same as our previous finding in [7]. Meanwhile, relatively constant power split ratio P_{gen}/P_{net} has been achieved over the entire load range, i.e., it slowly increases from 27.0% to 28.7% as P_{net} increases, as shown in Figure APX.12 (i). As shown in Figure APX.12 (f), the most efficient operation points are located in the plane where $FU = 75\%$ because more fuel is burned in the CB to elevate the temperatures and thus the power production. As shown in Figure APX.12 (f), the air excessive ratio ARincreases when going to part-load operations. This is the same as the results reported in [14], [21]. The maximum local cell temperature gradient T_{grad}, as shown in Figure APX.12 (h), increases with respect to P_{net} due to (1) increased degree of electro-chemical reactions; and (2) reduced AR ratio (note that a large AR ratio will help to smooth the SOFC temperature distributions).

BIBLIOGRAPHY

[1] Singhal, Subhash. *High-temperature Solid Oxide Fuel Cells: Fundamentals, Design and Applications: Fundamentals, Design and Applications*. Elsevier, 2003.

[2] Larminie, James, Andrew Dicks, and Maurice S. McDonald. *Fuel cell systems explained*. Vol. 2. Chichester: Wiley, 2003.

[3] Brouwer, J., Hybrid Gas Turbine Fuel Cell Systems, Chapter 4, in *The Gas Turbine Handbook*, Richard A. Dennis, ed., U.S. Department of Energy, DOE/NETL-2006/1230, Morgantown, West Virginia, 2006.

[4] Brouwer J. Fuel Cell & Hybrid Fuel Cell Gas Turbine System Design, Dynamics & Control. National Fuel Cell Research Center (NFCRC) internal report, April 18, 2011.

[5] Zabihian, Farshid, and Alan Fung. "A review on modeling of hybrid solid oxide fuel cell systems." *International Journal of Engineering* 3.2 (2009): 85-119.

[6] So-Ryeok Oh, Jing Sun, "Optimization and Load-Following Characteristics of 5kW-Class Tubular Solid Oxide Fuel Cell/Gas Turbine Hybrid Systems", pp. 417 - 422, 2010 American Control Conference, Baltimore, MD, USA.

[7] Zhenzhong Jia, Jing Sun, So-Ryeok Oh, Herb Dobbs, and Joel King. "Control of the dual mode operation of generator/motor in SOFC/GT-based APU for extended dynamic capabilities." *Journal of Power Sources* (2013).

[8] Jr. C. J. Steffen, J. E. Freeh, L. M. Larosiliere. “Solid oxide fuel cell/gas turbine hybrid cycle technology for auxiliary aerospace power”. In Proceedings of the ASME Turbo Expo. Reno-Tahoe, United States, 2005.

[9] W. Winkler, H. Lorenz. “The design of stationary and mobile solid oxide fuel cell-gas turbine systems”. Journal of Power Sources, 105: 222-227, 2002.

[10] Fang R., Jiang W., Khan J., Roger, D., 2009. System-Level Thermal Modeling and Co-simulation with Hybrid Power System for Future All Electric Ship, 2009 IEEE Electric Ship Technologies Symposium. pp. 547-553.

[11] Sun, J., Stebe, J., Kennell, C., 2010. Feasibility and Design Implications of Fuel Cell Power for Sealift Ships, Naval Engineers Journal, Vol. 22, No. 3, pp 87-102.

[12] So-ryeok Oh, Jing Sun, Herb Dobbs, and Joel King, "Model Based Predictive Control Strategy for a Solid Oxide Fuel Cell Engine Integrated with a Turbocharger," presented in 2012 American Control Conference, Montréal, Canada.

[13] Christoph Stiller, Bjørn Thorud, Olav Bollanda, et al, “Control strategy for a solid oxide fuel cell and gas turbine hybrid system”, Journal of Power Sources, Volume 158, Issue 1, pp 303–315, July 2006.

[14] Christoph Stiller, “Design, Operation and Control Modelling of SOFC/GT Hybrid Systems”, PhD thesis, Department of Energy and Process Engineering, Norwegian University of Science and Technology, Trondheim, Norway, March 2006.

[15] Vasilis Tsourapas, “Control analysis of integrated fuel cell systems with energy recuperation devices”, PhD thesis, University of Michigan, Ann Arbor, MI, USA, 2007.

[16] Caihao Weng, Jing Sun, “Design of a Variable Geometry Turbine Control Strategy for Solid Oxide Fuel Cell and Gas Turbine Hybrid Systems”, 2012 American Control Conference.

[17] Sieros, G.; Papailiou, K.D. “Gas turbine Components Optimised for use in Hybrid SOFC-GT Systems”. In the 7th European Conference on Turbomachinery fluid dynamics and thermodynamics, 2007.

[18] Calise, F., Palombo, A., and Vanoli, L. Design and partial load exergy analysis of hybrid SOFC-GT power plant. Journal of Power Sources, 158(1): pp225-244, 2006.

[19] Palsson, J. and Selimovic, A. Design and Off-Design Predictions of a Combined SOFC and Gas Turbine System. In Proceedings of ASME Turbo Expo 2001, number 2001-GT-0379, New Orleans, Louisiana, USA, 2001.

[20] David Tucker, Larry Lawson, Thomas P. Smith, Comas Haynes. "Evaluation of Cathodic Air Flow Transients in a Hybrid System Using Hardware Simulation". The 4th International Conference on FUEL CELL SCIENCE, ENGINEERING and TECHNOLOGY. June 19-21, 2006, Irvine, CA

[21] Costamagna, P., L. Magistri, and A. F. Massardo. "Design and part-load performance of a hybrid system based on a solid oxide fuel cell reactor and a micro gas turbine." Journal of Power Sources 96, no. 2 (2001): 352-368.

[22] Chan, S. H., H. K. Ho, and Y. Tian. "Modelling for part-load operation of solid oxide fuel cell–gas turbine hybrid power plant." Journal of Power Sources 114, no. 2 (2003): 213-227.

[23] David Hall. Transient Modeling and Simulation of a Solid Oxide Fuel Cell. PhD thesis, University of Pittsburgh, 1997.

[24] Handa Xi, “Dynamic Modeling and Control of Planar SOFC Power Systems,” Ph.D. thesis, University of Michigan, Ann Arbor, MI, USA, 2007.

[25] Erian A. Baskharone. Principles of turbomachinery in air-breathing engines. Cambridge University Press, 2006.

[26] Payri, F., J. R. Serrano, P. Fajardo, M. A. Reyes-Belmonte, and R. Gozalbo-Belles. "A physically based methodology to extrapolate performance maps of radial turbines." Energy Conversion and Management 55 (2012): 149-163.

[27] Karamanis, N., and R. F. Martinez-Botas. "Mixed-flow turbines for automotive turbochargers: steady and unsteady performance." *International Journal of Engine Research* 3.3 (2002): 127-138.

[28] Moraal, Paul, and Ilya Kolmanovsky. "Turbocharger modeling for automotive control applications." *SAE transactions* 108, no. 3 (1999): 1324-1338.

[29] Glad, Torkel, and Andey Sokolov. "Identifiability of Turbocharged IC Engine Models." In *Proceedings of the SAE 1999 International Congress & Exposition*. 1999.

[30] Garrett Turbochargers. http://www.turbobygarrett.com

[31] Veyo, Stephen E., et al. "Tubular solid oxide fuel cell/gas turbine hybrid cycle power systems: status." *Journal of Engineering for Gas Turbines and Power*124.4 (2002): 845-849.

[32] http://www.mhi.co.jp/en/news/sec1/200608041128.html (Mitsubishi Heavy Industries, Ltd, Japan)

[33] Bhattacharyya, D., & Rengaswamy, R. (2009). A review of solid oxide fuel cell (SOFC) dynamic models. *Industrial & Engineering Chemistry Research*, *48*(13), 6068-6086.

[34] Oh, So-Ryeok, et al. "Performance Evaluation of Solid Oxide Fuel Cell Engines Integrated With Single/Dual-Spool Turbochargers." Journal of Fuel Cell Science and Technology 8.6 (2011): 061020.

[35] Traverso, Alberto, et al. "Gas turbine assessment for air management of pressurized SOFC/GT hybrid systems." *Journal of fuel cell science and technology* 4.4 (2007): 373-383.

[36] Traverso, A., L. Magistri, and A. F. Massardo. "Turbomachinery for the air management and energy recovery in fuel cell gas turbine hybrid systems."*Energy* 35, no. 2 (2010): 764-777.

[37] http://web.mit.edu/16.unified/www/FALL/thermodynamics/notes/node131.html Thermodynamics Lecture Notes, Section 18.5: Heat Exchangers.

[38] http://www.cheresources.com/uexchangers.shtml (Heat Exchanger Resources)

[39] Zhenzhong Jia, Jing Sun, Herb Dobbs, and Joel King. “Modeling, Design and Control of Integrated SOFC Systems with Sprinter Gas Turbines”. *Journal of Power Sources*, submitted, 2014.

[40] Lance Smith, Hasan Karim, Shahrokh Etemad, and William C. Pfefferle. "Catalytic Combustion”, Section 3.2.2, and "Fuel-Rich Catalytic Combustion”,

Section 3.2.2.1, in *The Gas Turbine Handbook*, Richard A. Dennis, ed., U.S. Department of Energy, DOE/NETL-2006/1230, Morgantown, West Virginia, 2006.

[41] McLarty, Dustin, Jack Brouwer, and Scott Samuelsen. "Fuel cell–gas turbine hybrid system design part I: Steady state performance." *Journal of Power Sources* (2013).

[42] Hennessy, D. "Solid oxide fuel cell development at Delphi." *Fuel Cell Seminar (November 7)* (2012).

[43] Tse, Lawrence Kar Chung, Steven Wilkins, Niall McGlashan, Bernhard Urban, and Ricardo Martinez-Botas. "Solid oxide fuel cell/gas turbine trigeneration system for marine applications." *Journal of Power Sources* 196, no. 6 (2011): 3149-3162.

[44] Mourikis, Fotios. "Thermodynamic analysis of an SOFC-GT system for marine application on a LNG carrier". PhD Thesis, The University of Strathclyde, United Kingdom, 2008.

[45] Mueller, Fabian, Tobias Junker, Hossein Ghezel-Ayagh, Faryar Jabbari, Jacob Brouwer, and Rory Roberts. "Control design for a bottoming solid oxide fuel cell gas turbine hybrid system." *Journal of Fuel Cell Science and Technology* 4, no. 3 (2007): 221-230.

[46] Mueller, Fabian, Robert Gaynor, Allie E. Auld, Jacob Brouwer, Faryar Jabbari, and G. Scott Samuelsen. "Synergistic integration of a gas turbine and solid oxide fuel cell for improved transient capability." *Journal of Power Sources* 176, no. 1 (2008): 229-239.

[47] Kandepu, Rambabu, Lars Imsland, Bjarne A. Foss, Christoph Stiller, Bjørn Thorud, and Olav Bolland. "Modeling and control of a SOFC-GT-based autonomous power system." Energy 32, no. 4 (2007): 406-417.

[48] Roberts, Rory, Jack Brouwer, Faryar Jabbari, Tobias Junker, and Hossein Ghezel-Ayagh. "Control design of an atmospheric solid oxide fuel cell/gas turbine hybrid system: Variable versus fixed speed gas turbine operation."*Journal of Power sources* 161, no. 1 (2006): 484-491.

[49] Kaneko, T., J. Brouwer, and G. S. Samuelsen. "Power and temperature control of fluctuating biomass gas fueled solid oxide fuel cell and micro gas turbine hybrid system." *Journal of Power Sources* 160, no. 1 (2006): 316-325.

[50] Fardadi, Mahshid, Fabian Mueller, and Faryar Jabbari. "Feedback control of solid oxide fuel cell spatial temperature variation." *Journal of Power Sources*195, no. 13 (2010): 4222-4233.

[51] Mueller, Fabian, Faryar Jabbari, and Jacob Brouwer. "On the intrinsic transient capability and limitations of solid oxide fuel cell systems." *Journal of Power Sources* 187, no. 2 (2009): 452-460.

[52] Mueller, Fabian, Faryar Jabbari, Robert Gaynor, and Jacob Brouwer. "Novel solid oxide fuel cell system controller for rapid load following." *Journal of Power Sources* 172, no. 1 (2007): 308-323.

[53] So-Reyok Oh, Jing Sun, Herbert Dobbs, and Joel King. "Model Predictive Control for Power and Thermal Management of an Integrated Solid Oxide Fuel Cell and Turbocharger System." *IEEE Transactions on Control Systems Technology* 22, no.3 (2014): 911-920.

[54] Nishino, Takafumi, Hajime Komori, Hiroshi Iwai, and Kenjiro Suzuki. "Development of a comprehensive numerical model for analyzing a tubular-type indirect internal reforming SOFC." In *ASME 2003 1st International Conference on Fuel Cell Science, Engineering and Technology*, pp. 521-528. American Society of Mechanical Engineers, 2003.

[55] Aguiar, Patricia, C. S. Adjiman, and Nigel P. Brandon. "Anode-supported intermediate temperature direct internal reforming solid oxide fuel cell. I: model-based steady-state performance." *Journal of Power Sources* 138, no. 1 (2004): 120-136.

[56] Aguiar, P., C. S. Adjiman, and N. P. Brandon. "Anode-supported intermediate-temperature direct internal reforming solid oxide fuel cell: II. Model-based dynamic performance and control." *Journal of Power Sources* 147, no. 1 (2005): 136-147.

[57] Watson, Neil, and Marian Stefan Janota. *Turbocharging: The Internal Combustion Engine*. MacMillan, 1982.

[58] Pukrushpan, Jay T., Anna G. Stefanopoulou, and Huei Peng. *Control of fuel cell power systems: principles, modeling, analysis and feedback design*. Springer, 2004.

[59] Strang, Gilbert. "Linear Algebra and Its Applications. Thomson–Brooks." *Cole, Belmont, CA, USA* (2005).

[60] Kandepu, Rambabu. "Control Relevant Modeling and Nonlinear State Estimation Applied to SOFC-GT Power Systems." PhD thesis, Norwegian University of Science and Technology, Trondheim, Norway, 2007.

[61] Campanari, S., and P. Iora. "Definition and sensitivity analysis of a finite volume SOFC model for a tubular cell geometry." *Journal of Power Sources* 132, no. 1 (2004): 113-126.

[62] Tsai, Alex, Craig Groves, and David Tucker. "Improved Controller Performance of Selected Hybrid SOFC-GT Plant Signals Based on Practical Control Schemes."*Journal of Engineering for Gas Turbines and Power* 133, no. 7 (2011): 071702.

[63] Eriksson, Lars. "Modeling and control of turbocharged SI and DI engines." *Oil & Gas Science and Technology-Revue de l'IFP* 62, no. 4 (2007): 523-538.

[64] Eriksson, Lars, Lars Nielsen, Jan Brugård, Johan Bergström, Fredrik Pettersson, and Per Andersson. "Modeling of a turbocharged SI engine."*Annual Reviews in Control* 26, no. 1 (2002): 129-137.

[65] Alston, T., K. Kendall, M. Palin, M. Prica, and P. Windibank. "A 1000-cell SOFC reactor for domestic cogeneration." *Journal of Power Sources* 71, no. 1 (1998): 271-274.

[66] Lawlor, V., S. Griesser, G. Buchinger, A. G. Olabi, S. Cordiner, and D. Meissner. "Review of the micro-tubular solid oxide fuel cell: Part I. Stack design issues and research activities." *Journal of Power Sources* 193, no. 2 (2009): 387-399.

[67] Katrašnik, Tomai, Samuel Rodman, Ferdinand Trenc, Aleš Hribernik, and Vladimir Medica. "Improvement of the dynamic characteristic of an automotive engine by a turbocharger assisted by an electric motor." *Journal of engineering for gas turbines and power* 125, no. 2 (2003): 590-595.

[68] Seiichi Ibaraki, Yukio Yamashita, Kunio Sumida, Hiroshi Ogita, Yasuaki Jinnai. "Development of the 'Hybrid Turbo", an Electrically Assisted Turbocharger." *Mitsubishi Heavy Ind. Tech. Rev* 43, no. 3 (2006): 1-5.

[69] Campanari, Stefano. "Full load and part-load performance prediction for integrated SOFC and microturbine systems." *Journal of Engineering for Gas Turbines and Power* 122.2 (2000): 239-246.

[70] Richard Dorf, Robert Bishop. *Modern Control Systems* (12e), Prentice Hall, 2010.

[71] Strogatz, Steven. "Nonlinear dynamics and chaos: with applications to physics, biology, chemistry and engineering." (2001).

[72] Kim, Youngki, Tulga Ersal, Ashwin Salvi, Anna Stefanopoulou, and Zoran Filipi. "Engine-in-the-Loop Validation of a Frequency Domain Power Distribution Strategy for Series Hybrid Powertrains." *In IFAC Workshop on Engine and Powertrain Control, Simulation and Modeling*, Rueil-Malmaison, France. 2012.

[73] http://www.gasturb.de/ (GasTurb software)

[74] Maciejowski, Jan Marian. "Predictive control with constraints." (1999).

[75] Sanandaji, Borhan M., Tyrone L. Vincent, Andrew Colclasure, and Robert J. Kee. "Control-Oriented Modeling of a Solid-Oxide Fuel Cell Stack Using an LPV Model Structure." In *ASME 2009 Dynamic Systems and Control Conference*, pp. 793-800. American Society of Mechanical Engineers, 2009.

[76] Zhang, Xiongwen, Jun Li, Guojun Li, and Zhenping Feng. "Development of a control-oriented model for the solid oxide fuel cell." *Journal of power sources*160, no. 1 (2006): 258-267.

[77] Zhang, X., and Y-M. Wu. "A Control-oriented Dynamic Model Adapted to Variant Steam-to-carbon Ratios for an SOFC with Exhaust Fuel Recirculation."*Fuel Cells* 11, no. 2 (2011): 200-211.

[78] Sun, Jing, and Ilya V. Kolmanovsky. "Load governor for fuel cell oxygen starvation protection: A robust nonlinear reference governor approach." *Control Systems Technology, IEEE Transactions on* 13, no. 6 (2005): 911-920.

[79] http://www.epa.gov/cleandiesel/technologies/operations.htm

[80] Achenbach, Elmar. "Response of a solid oxide fuel cell to load change." *Journal of Power Sources* 57, no. 1 (1995): 105-109.

[81] Skogestad, Sigurd, and Ian Postlethwaite. *Multivariable feedback control: analysis and design*. Vol. 2. New York: Wiley, 2007.

[82] Stephanopoulos, G. "Chemical process control: an introduction to theory and practice." New Jersey, USA, 1984.

[83] University of Michigan Chemical Engineering Process Dynamics and Controls Open Textbook. http://controls.engin.umich.edu

[84] Hildebrandt, Andre, and Mohsen Assadi. "Sensitivity Analysis of Transient Compressor Operation Behaviour in SOFC-GT Hybrid Systems." In *ASME Turbo Expo 2005: Power for Land, Sea, and Air*, pp. 315-323. American Society of Mechanical Engineers, 2005.

[85] Jang, Seok-Myeong, Han-Wook Cho, and Sang-Kyu Choi. "Design and analysis of a high-speed brushless DC motor for centrifugal compressor." *Magnetics, IEEE Transactions on* 43, no. 6 (2007): 2573-2575.

[86] Rakopoulos, C. D., and E. G. Giakoumis. "Availability analysis of a turbocharged diesel engine operating under transient load conditions." *Energy*29, no. 8 (2004): 1085-1104.